Title
First-principles Discovery and Investigation of Novel Materials for Energy Conversion

Author
Cai, Yao

Publication Date
2019

Peer reviewed|Thesis/dissertation

First-principles Discovery and Investigation of Novel Materials for Energy Conversion

By

Yao Cai

A dissertation submitted in partial satisfaction of the

requirements for the degree of

Doctor of Philosophy

in

Engineering - Materials Science and Engineering

in the

Graduate Division

of the

University of California, Berkeley

Committee in charge:

Professor Mark Asta, Co-chair
Dr. Matthew Sherburne, Co-chair
Professor Junqiao Wu
Professor Jeffrey Neaton

Fall 2019

First-principles Discovery and Investigation of Novel Materials for Energy Conversion

Abstract

First-principles Discovery and Investigation of Novel Materials for Energy Conversion

by

Yao Cai
Doctor of Philosophy in Engineering – Materials Science and Engineering
University of California, Berkeley

Professor Mark Asta, Co-chair
Dr. Matthew Sherburne, Co-chair

This dissertation aims to employ density functional theory calculations to investigate energy-conversion materials. The main focus of this dissertation is on the emerging photovoltaic materials halide perovskites: the third and fourth chapters discuss perovskite-derived halides A_2BX_6 and double perovskite halides $A_2MM'X_6$, respectively. The fifth chapter discusses a novel material for photocatalytic water splitting.

In Chapter 3, we focus on a perovksite-derived halide A_2BX_6 for photovoltaic applications. The electronic structure and energetic stability of A_2BX_6 halide compounds with the cubic and tetragonal variants of the perovskite-derived K_2PtCl_6 prototype structure are investigated computationally within the frameworks of density-functional-theory and hybrid functionals(HSE06). The HSE06 calculations are undertaken for seven known A_2BX_6 compounds with A = K, Rb and Cs, and B = Sn, Pd, Pt, Te, and X = I. Trends in band gaps and energetic stability are identified, which are explored further employing semi-local density-functional-theory(DFT) calculations over a larger range of chemistries, characterized by A = K, Rb, Cs, B = Si, Ge, Sn, Pb, Ni, Pd, Pt, Se and Te and X = Cl, Br, I. For the systems investigated in this work, the band gap increases from iodide to bromide to chloride. Further, variations in the A site cation influences the band gap as well as the preferred degree of tetragonal distortion. Smaller A site cations such as K and Rb favor tetragonal structural distortions, resulting in a slightly larger band gap. For variations in the B site in the (Ni, Pd, Pt) group and the (Se, Te) group, the band gap increases with increasing cation size. However, no observed chemical trend with respect to cation size for band gap was found for the (Si, Sn, Ge, Pb) group. The findings in this work provide guidelines for the design of halide A_2BX_6 compounds for potential photovoltaic applications.

In Chapter 4, we focus on building a database for the double perovkite halides and employ the database to identify new materials for photovoltaic applications. Starting from a consideration of the octahedral and tolerance factors of ∼2000 candidate double-perovskite compounds, we compute structural, electronic and transport properties of ∼1000 using first-principles calculations based on DFT methods. The computational results have been assembled in a database that is accessible through the Materials Project online. As one potential

application, double perovskites are candidates in the search for lead-free halide photovoltaic absorbers. We present the application of our database to aid the discovery of new double perovskite halide photovoltaic materials, by combining the results with optical absorption and phonon stability calculations. Eleven compounds from three distinct classes of chemistries were identified as promising solar absorbers and the complex chemical trends for band gap within each of these are analyzed, to provide guidelines for the use of substitutional alloying as a means of further tuning the electronic structure.

In Chapter 5, we focus on the $SrNbO_{3+\delta}$ structures with different oxygen compositions and discuss their electronic properties based on DFT calculations of their electronic structures and charge density distributions. Under low oxygen pressure, films formed have the $SrNbO_3$ perovskite structure. $SrNbO_3$ has a heavily degenerate conduction band and a high carrier density. When growing under higher oxygen pressure, the carrier density decreases and the films become more insulating. The excess oxygen leads to the formation of extra oxygen planes with a density that increases with δ; at the nominal composition $SrNbO_{3.4}$, these extra oxygen planes should appear every 5 unit cells. According to our calculation for $SrNbO_{3.4}$, valence electrons are confined in the middle of two neighboring extra oxygen planes. These characteristics of the electronic structure lead to strong conventional plasmonic effects and strongly correlated plasmonic effects for $SrNbO_3$ and $SrNbO_{3.4}$, respectively.

Contents

Acknowledgements

First I would like to thank my advisor Professor Mark Asta for always being enlightening, encouraging, and supportive. Thank you for guiding me through the long journey of my Ph.D. study.

To my advisor Dr. Matthew Sherburne for being both an advisor and a friend.

To my dissertation committee: Professor Mark Asta, Dr. Matthew Sherburne, Professor Junqiao Wu and Professor Jeffrey Neaton.

To my qualifying exam committee: Professor Junqiao Wu, Professor Jeffrey Neaton, Professor Kristin Persson and Dr. Wladek Walukiewicz.

To the Asta Research Group, for always being gracious and helpful.

To Kevin Hong Ding, Wei Xie, Danny Broberg for valuable discussions on my research topics.

To my collaborators and co-workers I've been lucky to work with during the past years: Dongyang Wan, Yan Chen, Biplab Ghosh, Jakob Dahl, Professor Thirumalai Venkatesan, Professor Andrivo Rusydi, Professor Nripan Mathews.

To my friends at Berkeley for making my graduate life so much fun: Shuai, Yang, Lu, Xiaoxuan, Zhe, Sheng, Zilun, Zhenglu, Bo, Jade, Junxia, and everyone that brighten my days.

Finally, I would like to thank my husband Rui for all his encouraging words and unconditional supports. Thank you for being a great listener. To my mom and dad for their love and understanding. To my son Russell for being such a sweet little monster.

Chapter 1:

Introduction

1.1 Motivation

Solar energy, as a source of clean and renewable energy, can replace fossil fuels, reduce the emission of CO_2 and mitigate the problem of global warming. The price to install solar has drop by more than 70% over the last decades, and it is one of the largest new electric capacity additions over the last 6 years. Its share in total U.S. electrical generation has increased from only 0.1% in 2010 to more than 2% today.[1] There is still a long way to go for solar energy to reach its full potential. Even though it is a cleaner energy source than fossil fuels, current solar technologies still involve manufacturing processes that are not environmentally friendly. Developing next-generation solar technologies to replace the current technologies are a focus of the scientific community over the past decades.

There are several forms of utilizing solar energy, for example: photovoltaic, solar thermal and photochemical energy converters, etc. In solar thermal energy converters, solar energy is used to increase the kinetic energy of atoms and electrons in the solar thermal materials. Then these heated materials are used as heat engine just like a steam engine. In photovoltaic converter, solar energy is used to increase the potential energy of the electrons in the absorbing materials. Then these free electrons travel to an external circuit and drive the load. In photochemical energy converters, solar energy is used to increase the potential energy of the electrons, just like in a photovoltaic converter. The difference is that in photochemical energy converters these electrons are used to drive chemical reactions and the energy is then stored in products which can be used in fuel cells. In each of these utilization forms, the central problem is to find an appropriate material that can maximize the efficiency of energy conversion. Each of these conversion processes has strong requirements on the physical properties of the absorbing materials. Thus, how to find a low-cost, easy to make absorbing material with high conversion efficiency in a central challenge for the scientific community.

This thesis is focused on the absorbing materials in photovoltaic cells and photocatalyst water splitting(a form of photochemical energy conversion). Using density functional theory(DFT), this thesis investigates the stability, electronic structures, light absorbing efficiencies of these solar absorbing materials, and assesses their ability to be the next-generation solar converters. The remainder of this chapter will introduce the technical background of photovoltaic cells and photocatalyst water splitting.

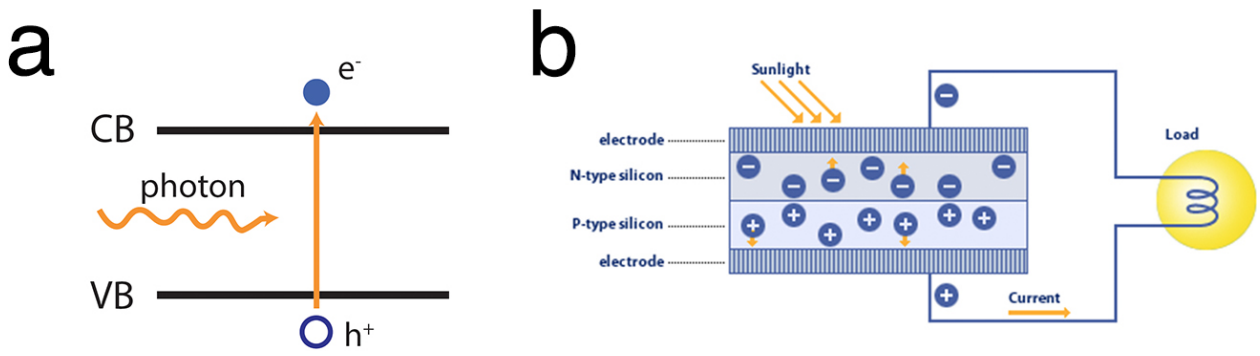

Figure 1.1: (a) The photovoltaic effects; (b) Schematic diagram of a Si p-n junction solar cell.

1.2 Photovoltaics

1.2.1 Physics of Photovoltaics

The review below follows the treatment of the subject given in Ref. [2], to which the reader is referred for further details. Photons with enough energy can excite electrons to higher energies. In semiconductors, the excited electrons can be used to do work if electrons are pulled to an external circuit before they relax to the ground state. In this way, energy in light is converted to electrical energy. A photovoltaic cell is such a device using semiconductors as light absorbing materials where electron-hole pairs are generated by incident photons from the sun. Electron and hole are then separated and collected at each of the two contacts of the device by the built-in spatial asymmetry[2]. The charges travel to the external circuit and can generate voltage and current when a load is connected.

Once excited to a higher energy state across the band gap, electron thermal relaxations happen on the time scale of femtoseconds, and radiative recombination happens on the time scale of microseconds, long enough for excited electrons to be collected. The chemical potential difference between the excited population and ground state population drives the potential difference between two terminals of the device.

Detailed balance requires that in equilibrium, the probability of absorbing a photon of energy E must be equal to the probability of emit a photon of energy E, such that there is no net current. Under illumination, absorption increases due to the solar photon flux, but since many electrons are in the excited state, the emission also increases. So there is always radiative recombination loss in solar cell devices. The net current density in the device is given by:

$$J(V) = J_{sc} - J_{dark}(V) \tag{1.1}$$

J_{sc} is photocurrent density derived from net absorption flux. In the ideal case where 1) the material is perfectly absorbing and non-reflecting; 2) perfect charge separation, then:

$$J_{sc} = q \int_{E_g}^{\infty} b_s(E) dE \tag{1.2}$$

where E_g is the band gap of the absorbing material and $b_s(E)$ is the sun spectrum.

$J_{dark}(V)$ is the dark current derived from spontaneous emission(radiative recombination loss). It depends on the bias applied to the device V:

$$J_{dark}(V) = J_0(e^{qV/k_BT} - 1) \tag{1.3}$$

When J(V) = 0, the bias applied is open cuicuit voltage V_{oc} and photocurrent and dark current exactly cancel each other. The power of the solar cell device and the power conversion efficiency(PCE) is then a function of the bias applied. Since absorption depends on band gap E_g, PCE also depends on E_g. If E_g is too small, absorbed energy is wasted through carrier thermal relaxation. If E_g is too large, photocurrent will be small since most low energy photons are not absorbed. So there is an ideal value of E_g for a specific incident spectrum. Under standard AM 1.5 solar spectrum, the ideal E_g is 1.4eV with a PCE of 33%[3].

In real solar cell devices, losses other than radiative recombination exist. Auger recombination is another type of unavoidable loss when carrier density is large. Auger recombination happens when an excited electron decays to the ground state and the energy released is used to increase the kinetic energy of another carrier, and will eventually be lost as heat when the carrier relaxes to the band edge. Shockley Read Hall (SRH) recombination[4] involves trap states or defects in semiconductors and can be avoided or mitigated by controlling the defect density in semiconductors. SRH recombination happens when a trap state captures a carrier and then captures another carrier of opposite polarity. If captured by shallow defects close to band edge, carriers can be thermally activated before the capture of carrier of the other polarity, and in such a case recombination will not happen. SRH recombination happens in deep defect states that are close to the center of the band gap, and energy is lost as heat. SRH recombination is the dominant mechanism of loss in real materials.

1.2.2 Perovskite Halide Solar Cell

In 1994, a family of tin halides with a layered organic-based perovskite structure were synthesized and found to have tunable electrical properties[5]. It was in the year 2009 when organic-inorganic lead halide perovskites were first used as the light absorber in solar cell devices, to replace the organic dye in dye-sensitized solar cell(DSSCs)[6]. In the first device $CH_3NH_3PbI_3$ was deposited on a TiO_2 mesoporous electrode and the device achieved a solar energy conversion efficiency of 3.8%[6]. In 2012, the full solid-state solar cell device with lead hailde perovksite deposited on mesoporous Al_2O_3 was fabricated and displayed a power conversion efficiency(PCE) of up to 10.9%[7]. The fact that Al_2O_3 is insulating indicated the long diffusion length of carriers in the lead halide perovskite, and hinted at the possibility of using a halide perovksite in planar n-i-p solar cell devices. Sequential deposition was employed to provide better control over the perovskite morphology and greatly increased the reproducibility of their performance, achieving a PCE of approximately 15%[8]. A planar heterojunction perovskite solar cell processed by vapor deposition was demonstrated with a high PCE of over 15%, showing that complex nanostructures are not necessary[9]. To date, the highest PCE achieved by lead halide perovskite solar cell devices reaches beyond 23%[10]. The rapid progress in this area within the last 10 years shows the potential of halide perovskites as a next-generation solar cell technology.

It is now widely accepted that the device architecture of a typical halide perovskite solar cell is of n-i-p type. The halide perovskite acts as the intrinsic solar absorber layer, and TiO_2 works as the electron transport material (ETM) while spiro-OMeTAD acts as the hole transport material (HTM). The ETM is usually deposited on a transparent conducting substrate such as indium tin oxide (ITO), or fluorine doped tin oxide (FTO). The HTM is usually connected to metal contact such as Au or Ag. The n-i-p device architecture and its energy diagram are illustrated in Fig. 1.2. Electron and hole pairs are generated by photon excitations, and then they are selectively collected by the ETM and HTM, respectively. They finally combine in the external curcuit. The band alignment depends on the selection of ETM and HTM, and a good band alignment is very important for a high PCE. The conduction band of the perovskite should be higher than the conduction band of the oxide ETM layer, so that the electrons can travel to the ETM layer barrier-free. It was shown that a higher PCE can be achieved using SnO_2 as the ETM layer for $MAPbI_3$, compared with using TiO_2 as the ETM layer[11].

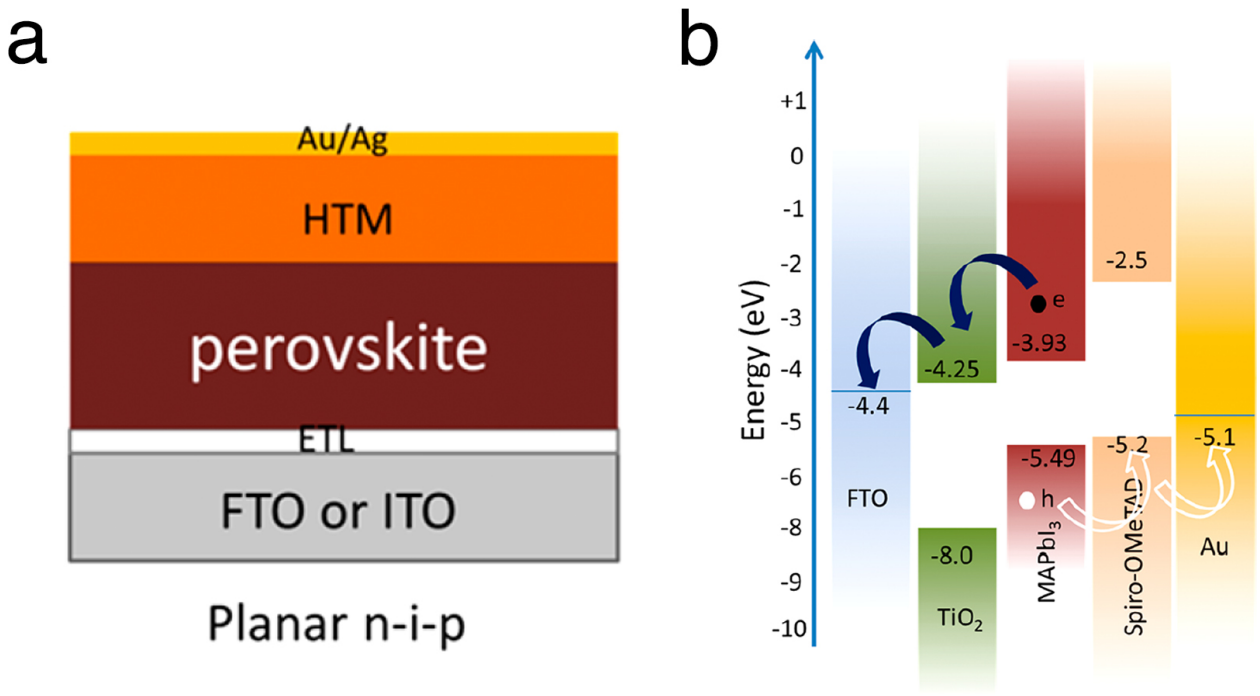

Figure 1.2: (a) The planar n-i-p architecture of a typical halide perovskite solar cell device; (b) the corresponding energy diagram. Reproduced from Ref [12].

The thin film form of the lead halide perovskite solar cell and the abundance of the elements used indicate that it is possible for the perovskite PV technology to compete with the current PV technology in terms of cost. A study shows that to reach TW level electricity generation, only a few days of lead global production is needed[13]. Halide provskite solar cell devices can be made by easy and cost-effective solution processing. In large area device fabrication, roll-to-roll production is made possible by several different coating methods compatible with solution processing, such as screening printing, slot-die coating, spray coating, etc [12].

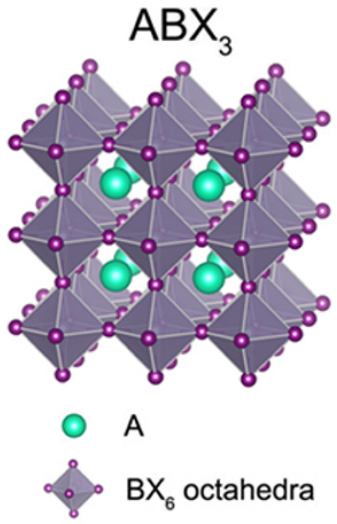

Figure 1.3: The perovskite structure, with corner-sharing BX_6 octahedra and A cations in the middle of eight neighboring octahedra. A cations can be inorganic or organic.

The perovskite structure is composed of corner-sharing octahedra BX_6 and A-site cations in the middle of eight neighboring octahedra, as shown in Figure 1.3. In high performance lead halide perovskites, the A site cation is usually an organic molecule, such as $CH_3NH_3^+$(MA) or $HC(NH_2)_2^+$(FA). The versatile perovskite structure can incorporate a large array of elements, making it possible to tune its physical properties through substitutional alloying. The band gap of a halide perovskite can be tuned easily by varying the content ratio of halide ions. The band gap usually increases when the halide ions transition from I to Br to Cl.

Organic/inorganic halide perovskites, $MAPbI_3$ for example, have a sharp absorption onset and excellent absorption coverage of the visible light regions. The excellent optical absorption is attributed to the fact that the valence band maximum (VBM) derives from Pb-s and I-p hybridization, enabling a large joint density of states(JDOS) when transitioning to the conduction band minimum (CBM) of Pb-p character[14]. Such a transition has larger JDOS than in GaAs, where the VB-CB transition is from p orbital to s orbital. The JDOS in GaAs is smaller due to the dispersive s orbital[14]. $MAPbI_3$ also has superior defect properties. It was proposed that the defects in $MAPbI_3$ are all shallow defects and as a result trapped carriers can easily escape from the these defects, leading to $MAPbI_3$'s long carrier diffusion length (175 μm in single crystal[15]). This defect-tolerant feature is due to the fact that all deep defects in $MAPbI_3$ have high formation energy and shallow defects have low formation energy, so all dominant defects in $MAPbI_3$ are shallow[14].

Photophysics of halide perovskite is still under investigation and debate. Several different theories were proposed to explain the relationship between its structure and the superior optoelectronic properties. One of the theories focuses on lattice softness and stochastic structural fluctuations(the anharmonic motion of a halide atom or tumbling motion of the organic cation) and their impact on optoelectronic properties[16]. Another theory focuses on the ferroelectricy in lead halide perovskites and ferroelectric-like large polarons, where polar

nanodomains are formed around the charge. The large screening of the Coulomb potential provided by the ferroelectric-like large polarons reduces carrier scattering[17]. A third theory proposed that Rashba-type effects might exist in lead halide perovskites, owing to the presence of heavy atoms and inversion symmetry breaking. The slow carrier recombination was interpreted as evidence of Rashba effects[18]. Subsequent work challenged the interpretation, however[19].

Even with the significant advantages of lead halide perovskites summarized above, commercialization of solar cells based on these materials might still be hindered by several problems: 1) the toxicity of Pb; 2) the long-term stability, including both intrinsic/structural stability and extrinsic/environmental stability. Intrinsic stability includes the structural stability of the perovskite structure, which requires that the tolerance factor within $0.8 \sim 1.0$, with 0.9 being ideal. The structural stability can be improved by compositional engineering of perovskite. Other intrinsic instabilities include ion migration under electric field and strain-induced degradation[12]. Extrinsic instabilities include sensitivity of perovskite to moisture, oxygen, heat, light, etc. Hybrid halide perovskite easily bind water molecules by hydrogen bonding[20]. Many of the degragation processes are found to be enhanced by light[12]. Perovskite films exposed to oxygen and light at the same time degrade faster than in moisture[12]. Finding a good sealing and packaging technology may be helpful to preventing leakage of Pb-containing compounds and protecting the devices from moisture and oxygen, but the intrinsic instabilities and sensitivity to light must be solved by other engineering techniques.

Finding alternative lead-free perovskite compounds is another approach to the above problems. The simple structure of perovskite makes it easy to incorporate various chemistries. Several perovksite-related structure motifs can incorporate cations of different oxidization states. AMX_3 of perovskite structure can incorporate divalent M^{2+} cations, such as Sn^{2+} and Ge^{2+}, etc. A_2MX_6 of perovskite-derived K_2PtCl_6 prototype structure can incorporate tetravalent M^{4+} such as Sn^{4+}, Te^{4+} and Pt^{4+}, etc. $A_3M_2X_9$ of layered perovskite structure can incorporate trivalent M^{3+} cations such as Sb^{3+} and Bi^{3+}, etc. $A_2MM'X_6$ of double perovskite structure can incorporate both monovalent M^{1+} such as Cu^{1+}, Ag^{1+}, In^{1+} and trivalent M'^{3+} cations, such as Sb^{3+} and Bi^{3+}, etc. These alternative compounds may share some of the advantages of lead halide perovskites, such as simple solution processing, tunability through solid solution, and at the same time avoid some of the disadvantages of lead halide perovskites, such as toxicity of lead, structural instability, etc.

A large compositional space can be formed using all possible combinations, and solid solutions between different compounds can be further explored to finely tune the physical properties. Chapter 3 and chapter 4 focus on exploring A_2MX_6 and double perovskite $A_2MM'X_6$ compounds, respectively. Chemical trends in the compositional space are carefully investigated to provide insight into possible alloying strategies. The promising candidates proposed in these two chapters point out new directions in furthering development of these materials for next-generation PV technology.

1.3 Photocatalytic water splitting

Another form of utilizing solar energy is through photocatalytic water splitting, producing H_2 as a clean and renewable energy source. Currently, most of H_2 production is through fossil fuels and CO_2 is emitted as by-products during the process[21]. As more knowledge is accumulated in the mechanism of photocatalytic water splitting and development of new materials, the cost of photocatalytic water splitting will decrease and it might become the primary source of H_2 production.

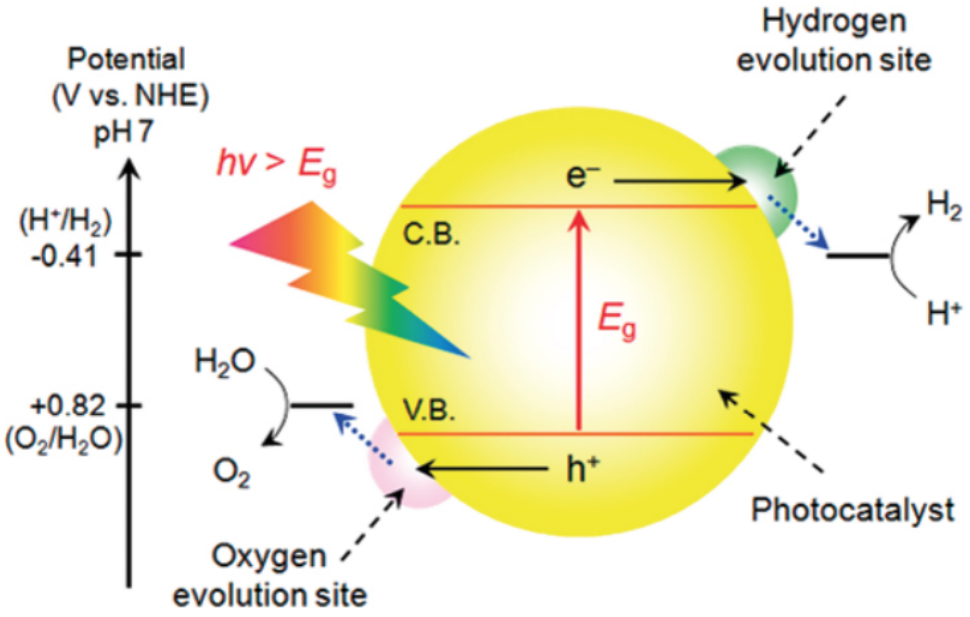

Figure 1.4: Schematic energy diagrams of photocatalytic water splitting. Reproduced from [22]
.

As shown in Fig. 1.4, similar to solar cell devices, in photocatalytic water spliting, the photocatalyst is usually a semiconductor. Electron and hole pairs are generated by incident photons of energy larger than the band gap of the semiconductor. Electrons and holes then transport to the surface of the photocatalyst and cause redox reactions with H_2O. Electrons reduce H_2O to form H_2 and holes oxidize H_2O to form O_2. It is important that the conduction band of the photocatalyst is more negative than the redox potential of H^+/H_2 and the valence band is more positve than the redox level of O_2/H_2O. Thus the band gap of the photocatalyst must be larger than 1.23 eV. To utilize as much solar energy as possible, the band gap should be smaller than 3.0 eV to utilize visible light.

Similar to solar cell devices, recombination losses in the photocatalyst cause low efficiency in photocatalytic water spliting. The dominant recombination loss is caused by recombination centers provided by defects. Two approaches can help reduce the recombination loss: 1) use of photocatalysts of small particle size, so that it is easier for carriers to travel to the surface of the photocatalyst; 2) increase the quality of the photocatalyst crystal to reduce defect density.

Sometimes a co-catalyst such as Pt is needed for H^+ reduction since the conduction band of oxide photocatalysts is usually not high enough to reduce H^+[21]. The requirements for electronic structure and band levels in one-step single photocatalyst system are very hard to meet. In a two-step Z-scheme system, two different photocatalysts are used for H_2 and O_2 evolution, respectively. A redox couple such as IO_3^-/I^- must be present as redox mediator. On the surfaces of one photocatalyst, I^- reacts with holes to form IO_3^- and help H^+ reduced to form H_2. On the surfaces of the other photocatalyst, IO_3^- reacts with electrons to form I^- and helps to oxidize H_2O to form O_2. [21]

From the above examples, we know that electronic structures are important to explain the working mechanism of photocatalysts. Chapter 5 will present the investigation into a novel metallic photocatalyst and its mechanism of photocatalytic water splitting.

Chapter 2:

Theory and simulation methods

2.1 Density Functional Theory

In this chapter, I will introduce the main theoretical method used in this dissertation: density functional theory(DFT)[23]. Density functional theory is one of the most widely used first-principles theories to predict the ground-state physical properties of molecules and solids. The ground state of materials are dictated by the solution to the interacting quantum many-body Schrodinger equation with the Hamiltonian describing the interaction of a collection of ion cores and valence electrons:

$$H_{tot} = \sum_j \frac{P_j^2}{2M_j} + \sum_i \frac{p_i^2}{2m} + \sum_{j<j'} \frac{Z_j Z_{j'} e^2}{|R_j - R_{j'}|} + \sum_{i<i'} \frac{e^2}{|r_i - r_{i'}|} + \sum_{i,j} \frac{-Z_j e^2}{|R_j - r_i|} \tag{2.1}$$

where the first term is the kinetic energy of the ion cores, the second term is the kinetic energy of the valence electrons, the third term is the Coulomb interaction between the ion cores, and the fourth term is the Coulomb interaction between the valence electrons and the last term is the Coulomb interaction between the ion cores and valence electrons. Exact solution to many-body Schrodinger equation is impractical.

The first approximation made to the above many-body Hamiltonian is the Born-Oppenheimer adiabatic approximation[24]. Since ion cores are much heavier and move much slower than electrons, so as an approximation, we can fix ion cores and treat ion cores as external fields for electronic Hamiltonian:

$$H_e = \sum_i \Big[\frac{p_i^2}{2m} + \sum_j V_j(r_i - R_j)\Big] + \sum_{i<i'} \frac{e^2}{|r_i - r_{i'}|} \tag{2.2}$$

where V_j is the external potential due to the jth ion core. Once the electronic Schrodinger equation is solved, core Schrodinger equation can then be solved to determine the energy spectrum of the cores and core motions.

2.1.1 The Hohenberg-Khon Theorems

But we still have a many-body problem, the operators for kinetic energy and interaction energy with the external potential can be easily separated for a single-particle problem, but we still have the electron-electron interaction term that cannot be readily separated. The treatment of the electron-electron interaction is one of the major challenges in condensed matter physics. In 1964, a famous paper by Hohenberg and Kohn proposed the formulation

of density functional theory(DFT) to address this problem[23]. They proposed and proved two theorems that are the foundation of density functional theory:

Theorem 1: The ground-state energy E is a unique functional of the electron density $\rho(r)$ except for a constant.

This theorem can be easily proved by contradiction for non-degenerate ground state. We know that E is a unique functional of external potential $v(r)$, if we can prove that $v(r)$ is a unique functional of $\rho(r)$, then E is also a unique functional of $\rho(r)$. Let's assume the that there is another potential $v'(r)$ such that its ground state $|\Psi'\rangle$ corresponds to the same density $\rho(r)$. For the primed system:

$$E' = \langle \Psi' | H' | \Psi' \rangle \tag{2.3}$$

Also we know for non-degenerate ground state:

$$\langle \Psi' | H' | \Psi' \rangle < \langle \Psi | H' | \Psi \rangle = \langle \Psi | H - V + V' | \Psi \rangle = E + \int [v'(r) - v(r)] \rho(r) dr \tag{2.4}$$

So:

$$E' < E + \int [v'(r) - v(r)] \rho(r) dr \tag{2.5}$$

Similarly, for the unprimed system:

$$E < E' + \int [v(r) - v'(r)] \rho(r) dr \tag{2.6}$$

Add the above two inequality together we have:

$$E + E' < E' + E \tag{2.7}$$

which is not true, thus we proved $v(r)$ is a unique functional of $\rho(r)$ and so E is a unique functional of $\rho(r)$.

Theorem 2: The global minimum of this functional $E(\rho)$ is the exact ground state energy E_0, and the density that minimizes the functional is the exact ground state density $\rho_0(r)$.

The proof of Theorem 2 is also straight-forward. Suppose the ground-state density is $\rho(r)$, the corresponding external potential is $v(r)$, and the corresponding ground state wavefunction is $|\Psi\rangle$. Then the energy functional is:

$$E = \langle \Psi | H | \Psi \rangle \tag{2.8}$$

Now consider a different density $\rho'(r)$, which corresponds to a different wavefunction $|\Psi'\rangle$. Then:

$$E = \langle \Psi | H | \Psi \rangle < \langle \Psi' | H | \Psi' \rangle = E' \tag{2.9}$$

Thus we have proved that the ground state density indeed leads to the lowest energy of the system, and it is the ground state energy of the system. Then by minimizing the energy of the system, one can get the exact ground state density and ground state energy.

2.1.2 The Kohn-Sham Equations

The remaining problem is that the functional form of $E(\rho)$ is not known yet. The functional form of the interaction energy with external field is straight-forward and can be written as $\int v(r)\rho(r)dr$. However, because of the electron-electron interaction, the form of electron kinetic energy and electron-electron interaction energy in terms of electron density can be complicated. For a non-interacting system with the same density, the kinetic energy of the system can be written as:

$$T_s(\rho) = -\frac{\hbar^2}{2m}\sum_i^{occ}\int \psi_i^*(r)\nabla\psi_i(r)dr \tag{2.10}$$

If we ignore exchange and correlation, then the interaction energy is the Hartree term:

$$E_{Hartree} = \frac{e^2}{2}\int \frac{\rho(r)\rho(r')}{|r-r'|}drdr' \tag{2.11}$$

The total energy of the interacting system can be written as:

$$E(\rho) = \int v(r)\rho(r)dr + T_s(\rho) + E_{Hartree} + E_{xc}(\rho) \tag{2.12}$$

where $E_{xc}(\rho)$ is the exchange-correlation energy functional which includes everything we do not include in the sum $T_s(\rho) + E_{Hartree}$.

Kohn and Sham proposed an auxiliary non-interacting system with an effective potential $v_{eff}(r)$ to help find the ground state density and energy of the interacting system[25]. The goal is to find a density that minimized the total energy. We can derive the $v_{eff}(r)$ such that the density $\rho(r)$ of the non-interacting system is also the ground state density of the real system(i.e., that which minimizes E). The $v_{eff}(r)$ found this way is:

$$v_{eff}(r) = v(r) + e^2\int \frac{\rho(r')}{|r-r'|}dr' + \frac{\delta E_{xc}(\rho)}{\delta\rho(r)} \tag{2.13}$$

This leads to the one-particle Kohn-Sham equations for the auxiliary non-interacting system:

$$(\frac{p^2}{2m} + v_{eff}(r))\psi_i(r) = \epsilon_i\psi_i(r) \tag{2.14}$$

Solving Kohn-Sham equations self-consistently we can obtain the ground state density of the non-interacting system $\rho(r) = \sum_i^{occ}|\psi_i(r)|^2$, which is also the ground state density of the real system, and then the ground state energy of the real system can also be calculated.

It should be note that DFT can only give us the ground state density and energy, but not the excited states. Especially, the Kohn-Sham eigenvalues and eigenfunctions do not correspond to the excitation energy and electron wave-functions in the real system. They are just for the auxiliary non-interacting system, and they appear just as a mathematical trick to use the variational principle to obtain the ground state density and energy of the real system. Thus only the ground state density and energy are exact in the DFT formalism. In band gap calculations for semiconductors and insulators, DFT usually underestimates the band gap. The band gap problem of DFT calculation comes from this misuse of the Kohn-Sham eigenvalues.

2.1.3 Exchange-correlation Energy Functional

The above discussions assume that we know the functional form of E_{xc}. Even though we do not know the exact from of E_{xc}, there are several approximations that work well in practice. The most simple one is local density approximation:

$$E_{xc}^{LDA} = \int \rho(r)\epsilon_{xc}^{hom}(\rho(r))dr \tag{2.15}$$

which makes the approximation that E_{xc} is local. The exchange-correlation energy density ϵ_{xc}^{hom} is a function of the local density $\rho(r)$ and the dependence of ϵ_{xc}^{hom} on $\rho(r)$ is the same as in a homogeneous electron gas with the same ρ. The Kohn-Sham construct separates out the independent-particle kinetic energy and the long-range Hartree terms, E_{xc} thus can be approximated as nearly local functional of density. In most solids with typical densities, the range of the effects of exchange and correlation is rather short, so LDA works pretty well for solids[26].

Another approximation beyond LDA is the generalized gradient approximation(GGA), where exchange-correlation density is a function of both $\rho(r)$ and $\nabla\rho(r)$:

$$E_{xc}^{GGA} = \int \rho(r)\epsilon_{x}^{hom}(\rho(r))F_{xc}(\rho(r), \nabla\rho(r))dr \tag{2.16}$$

where F_{xc} is the dimensionless enhancement factor and ϵ_x^{hom} is the exchange energy of homogeneous gas.

The exchange enhancement factor $F_x \geq 1$, so GGA leads to an exchange energy lower than the LDA. While LDA over-binds, GGA reduces binding energy and improves agreement with experiment[26]. Different forms of F_x has been proposed, with Perdew and Wang(PW91)[27] and Perdew, Burke and Enzerhof(PBE)[28] being the most widely used forms. For most physical applications, the density gradient is relatively small. In such regime, the different forms of F_x have nearly identical shapes, so different GGAs give similar results. The functional form of correlation is more complicated, but its contribution to the total energy is also much smaller than exchange[26].

2.2 Corrections and Improvements upon Conventional DFT

2.2.1 Self-interaction Error

If we look at at the second term of the effective potential $v_{eff}(r)$, the Hartree term (Equation 2.13) closely, we realize the physical meaning of this term is the Coulomb interaction between an electron and the total electron density of the system, with the latter including the former electron itself. This un-physical interaction between the electron and itself causes the self-interaction error. If we know the exact form of the true exchange-correlation functional, the self-interaction error would be cancelled out by the exchange-correlation functional. But in any approximate form of the exchange-correlation functional (i.e. LDA, GGA, etc), the self-interation error cannot be cancelled out exactly, and it can be large since these terms involve large Coulomb interations. It should be noted that in Hartree-Fork method, the self-interaction energy is cancelled exactly by the exact exchange energy.

Even in one-electron systems where there is no electron-electron interaction, the Hartree-term is non-zero and caused the self-interaction error. Self-interaction error causes more problems in strongly correlated systems, where electrons are highly localized. With semi-local DFT, the localized electrons are calculated to be un-physically delocalized. Delocalization helps to minimize the self-interaction energy, which should not exist at all. Self-interaction error also causes problem in defect calculations when localized defects are calculated to be spatially delocalized with semi-local DFT[29].

Several approaches were proposed to deal with self-interaction error. Among them two approaches are especially popular: hybrid functionals and DFT+U functionals. The hybrid functionals are employed heavily in Chapter 3 and Chapter 4 and the DFT+U functionals are used in Chapter 5. The two methods are discussed in more detail below.

2.2.2 Hybrid Functionals

Hartree-Fock method includes an exact treatment of exchange interaction and self-interaction of an electron with itself is canceled out. However, the Hartree-Fock approximation does not include electron correlation, and thus can lead to significant deviation compared with experiments. DFT with semi-local functionals include both exchange and correlation but within a local or semi-local (as described the dependence on density gradient) approximation, and in this case the self-interaction error can be significant. Hybrid functionals which incorporate some portion of exact exchange with semi-local density functional were proposed and proved to lead to significant improvement in calculating structural, thermodynamic and electronic properties of molecules and periodic systems.

Heyd et al[30] showed that in metallic systems, convergence with distance is very hard to achieve with Hartree-Fock(HF) calculations, which greatly increases the time complexity of hybrid calculations. However if only the short-range component of HF exchange interaction are considered, convergence with distance can be achieved exponentially. So they proposed to separate the Coulomb operator into short-range(first-term) and long-range(second-term) components, and only mix in a portion of short-range exchange into semi-local density functional such that the computation efficiency is greatly improved.

The error function is used to separate the Coulomb operator:

$$\frac{1}{r} = \frac{erfc(\omega r)}{r} + \frac{erf(\omega r)}{r} \tag{2.17}$$

where the first-term is the short-range term, second term is the long-range term and ω is the range-separation parameter. When $\omega = 0$, the long-range term disappears and the short-range term is just $\frac{1}{r}$. When $\omega \to \infty$, the short-term disappears and the long-term is just $\frac{1}{r}$.

And the form of the hybrid functional(referred as HSE functional) is defined below:

$$E_{xc}^{HSE} = \frac{1}{4}E_x^{HF,SR}(\omega) + \frac{3}{4}E_x^{PBE,SR}(\omega) + E_x^{PBE,LR}(\omega) + E_c^{PBE} \tag{2.18}$$

It can be shown that the long-range exchange from both HF and PBE are very small and in opposite sign and tend to cancel each other. $2/\omega$ is the characteristic distance at

which the short-range exchange converges with distance. When $\omega = 0$, $2/\omega \to \infty$ and the long-terms disappear, and HSE functional essentially becomes PBE0 functional where the whole exchange interaction is mixed in with PBE functional. When $\omega \to \infty$, the short-range terms disappear and HSE functional essentially becomes PBE functional where no exchange interaction is mixed in. In HSE06 functional, ω is set to be 0.2 A^{-1} and preserves good accuracy for band gaps and lattice constants in solids[31, 32]. In chapter 3 and 4, we will use HSE06 hybrid functional extensively to obtain reasonable predictions for band gaps in perovskite halides.

2.2.3 DFT+U Functional

In systems with partly filled d or f shells where on-site Coulomb interaction is very important, DFT with semi-local functionals is inadequate because of oversimplified treatment of exchange and correlation in an averaged way. Such systems are called strongly correlated systems and usually contain transition metal or rare-earth metal elements. When the on-site Coulomb repulsion(characterized by the Hubbard U in Hubbard Model) is large compare with the valence bandwidth(characterized by the overlap integral in Hubbard Model), hopping of electrons between metal ions will not happen, electrons will be localized and the system is an insulator. DFT with semi-local functionals often cannot obtain the right ground state for such systems, either finding a metallic state when the ground state is an insulator, or obtaining an insulator state with much smaller band gap than the true ground state.

DFT+U is a correction to DFT that adds a Hubbard-like orbital-dependent penalty term to the total energy expression and can account for the strong on-site repulsion for the localized d or f electrons in the system. The total energy expression for DFT+U in Dudarev's formalism[33] has the following form:

$$E_{DFT+U} = E_{DFT} + \frac{U-J}{2} \sum_{\sigma} \Big[\Big(\sum_{j} \rho^{\sigma}_{jj} \Big) - \Big(\sum_{j,l} \rho^{\sigma}_{jl} \rho^{\sigma}_{lj} \Big) \Big] \tag{2.19}$$

where U and J are the on-site Coulomb and exchange parameters, j and l denote the magnetic quantum number and σ the spin index, ρ^{σ}_{jl} is the on-site density matrix of the localized shell in consideration. As in the simple 1D Hubbard model, this Hubbard-like penalty term forces the on-site density matrix to have either 1 or 0 eigenvalues, which physically means either fully occupied or fully unoccupied states are favored. Here U and J do not enter the expression separately, but together as a single effective Hubbard-U $U_{eff} = U - J$. This parameter can either be extracted from ab-initio calculations[34, 35] or calculated semi-empirically[36].

The orbital-dependent nature of DFT+U method introduces the orbital degree of freedom which are absent in conventional DFT, and lends to multiple self-consistent solutions induced by different occupation of the orbitals. These states includes both metastable states and ground state whose energies can differ by several hundred meV per atom[37]. The barrier between the metastable and ground state might be high and prevent the relaxation into the true ground state. We will discuss this problem that always accompanies DFT+U calculations in Chapter 5.

Chapter 3:

Computational Study of Halide Perovskite-Derived A_2BX_6 Inorganic Compounds: Chemical Trends in Electronic Structure and Structural Stability

3.1 Abstract

The electronic structure and energetic stability of A_2BX_6 halide compounds with the cubic and tetragonal variants of the perovskite-derived K_2PtCl_6 prototype structure are investigated computationally within the frameworks of density-functional-theory (DFT) and hybrid (HSE06) functionals. The HSE06 calculations are undertaken for seven known A_2BX_6 compounds with A = K, Rb and Cs, and B = Sn, Pd, Pt, Te, and X = I. Trends in band gaps and energetic stability are identified, which are explored further employing DFT calculations over a larger range of chemistries, characterized by A = K, Rb, Cs, B = Si, Ge, Sn, Pb, Ni, Pd, Pt, Se and Te and X = Cl, Br, I. For the systems investigated in this work, the band gap increases from iodide to bromide to chloride. Further, variations in the A site cation influences the band gap as well as the preferred degree of tetragonal distortion. Smaller A site cations such as K and Rb favor tetragonal structural distortions, resulting in a slightly larger band gap. For variations in the B site in the (Ni, Pd, Pt) group and the (Se, Te) group, the band gap increases with increasing cation size. However, no observed chemical trend with respect to cation size for band gap was found for the (Si, Sn, Ge, Pb) group. The findings in this work provide guidelines for the design of halide A_2BX_6 compounds for potential photovoltaic applications.

3.2 Introduction

Since the initial discovery of lead halide perovskite compounds as solar absorbers for photovoltaic devices[6, 7, 39], the power conversion efficiencies (PCEs) achieved with these

The results presented in this chapter and appendix A have been published as a regular article with title "*Computational Study of Halide Perovskite-Derived A_2BX_6 Inorganic Compounds: Chemical Trends in Electronic Structure and Structural Stability*" in Chem. Mater. 2017, 29, 77407749 by Yao Cai, Wei Xie, Hong Ding, Yan Chen, Krishnamoorthy Thirumal, Lydia H. Wong, Nripan Mathews, Subodh G. Mhaisalkar, Matthew Sherburne and Mark Asta[38]. The material is presented here with the permission of co-authors and publishers.

materials has increased steadily and currently reaches 22.1%[40]. These high PCEs have motivated significant efforts aimed ultimately at the commercial application of lead-based halide perovskites for solar power conversion. For such applications, two issues that continue to receive considerable attention are the toxicity of lead, which can be leached out of $APbX_3$ compounds due to their aqueous solubility [41], and the poor chemical stability in air [41]. The first of these two issues has motivated research into the use of alternative Sn/Ge-based perovskite compounds, although limited PCEs of 6% or less have been demonstrated with these materials to date [42–45]. Further, like their Pb-based counterparts, Sn/Ge-based perovskite compounds also have been found to suffer from poor chemical stability [42, 43, 45].

The inorganic compound Cs_2SnI_6 has received recent attention as an alternative to Sn-based halide-perovskites for photovoltaic device applications. In comparison with Sn and Pb based halide perovskites, Cs_2SnI_6 has been shown to feature enhanced stability in ambient environments[46–48], correlating with the presence of a more stable higher oxidation state for Sn in this compound (formally 4+ in Cs_2SnI_6 compared with 2+ in $CsSnI_3$). The crystal structure of Cs_2SnI_6 can be described as a defect variant of perovskite, with half of the Sn atoms removed, as illustrated in Fig. 3.1. In this figure, the SnX_6 octahedra in the Cs_2SnI_6 compound can be seen to be isolated, in contrast to the corner-sharing arrangement characterizing the perovskite structure. Associated with this structural change, the Sn-I bond lengths are shorter in the Cs_2SnI_6 compound, which has been correlated with its enhanced chemical stability [49].

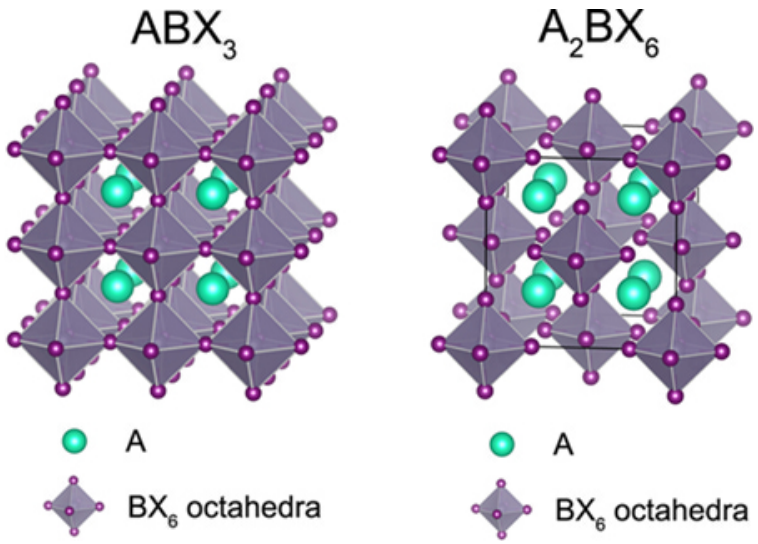

Figure 3.1: Crystal structures of ABX_3(left) and A_2BX_6(right).

In addition to its desirable stability, the electronic and optical properties of Cs_2SnI_6 also have been demonstrated to be attractive for photovoltaic device applications. Specifically, Cs_2SnI_6 is a direct-gap semiconductor that displays strong visible light absorption [47, 50]. The measured band gaps reported range from 1.6 eV[47] to 1.48 eV[50] to 1.3 eV[46]. The valence band and conduction band are well dispersed, with dominant characters based on I-p and hybridized I-p/Sn-s orbitals, respectively[46]. A high electron mobility of 310 $cm^2/V{*}s$ and a sizable hole mobility 42 $cm^2/V{*}s$ were reported in bulk compounds [46]. The Cs_2SnI_6

compound has been reported to display intrinsic n-type conductivity[46, 47] (with carrier concentrations of 10^{14} cm^{-3} and $5{*}10^{16}$ cm^{-3}), and it has been shown that it can be doped p-type with SnI_2[46] (with carrier concentrations of 10^{14} cm^{-3}), demonstrating the ambipolar nature of this material [46]. As an initial attempt, PCEs of about 1% in air have been recently demonstrated in photovoltaic devices employing this material as a photoabsorber [50].

As a means for further optimizing the properties of Cs_2SnI_6 for device applications, substitutional alloying is expected to be a useful strategy, as the A_2BX_6 structure can be readily doped with different impurity ions, especially in the 6-fold coordinated tetravalent cation site[51]. Studies investigating the effect of chemical substitutions have been limited to date, but they have clearly demonstrated the possibility of tuning electronic properties. For example, in a study comparing hole-transport properties in Cs_2SnI_6, Cs_2SnBr_6 and Cs_2SnCl_6 systematic variations in the optical and transport properties were observed to be correlated with the substitution of halogen anions having different size and electronegativity [48]. In another study the alloying of Cs_2SnI_6 with Cs_2TeI_6, to form $Cs_2(Sn_{1-x}Te_x)I_6$ solid solutions, was found to lead to reduced mobility and reduced defect tolerance [52]. While these studies have not yet resulted in improved materials for device applications, they have clearly demonstrated the importance of the B-X chemistry in defining optical and transport properties.

To guide further studies aimed at the use of chemical substitutions to optimize properties for photovoltaic applications, in this work we employ density-functional-theory (DFT) based computational methods to explore trends underlying the variation of electronic structure and structural stability of A_2BX_6 compounds with chemical composition. We begin by employing hybrid-functional (HSE06) methods to calculate and analyze the electronic structures of seven known inorganic compounds with varying A(=K, Rb, Cs) and B(=Pt, Pd, Sn, and Te) site cations, for the case of X=I. We use these results as benchmarks to demonstrate the ability of computationally more efficient semi-local DFT functionals(Perdew-Burke-Ernzerhof parametrization of the generalized gradient approximation, or GGA-PBE) to capture chemical trends. Using the GGA-PBE method we extend the study to consider a wider range of chemistries on the A (A= K, Rb, Cs), B (B= Si, Ge, Sn, Pb, Ni, Pd, Pt, Se, Te) and X sites (X = Cl, Br, I).

The results yield the following chemical trends. For variations in the halide anion from Cl to Br to I, the band gap and effective mass are found to decrease, while variations in the A site cation from Cs to Rb to K, lead to an increase in tetragonal distortion and an associated increase in band gap and effective mass. For variations in the B site in the group of Si, Ge, Sn, Pb, there is no observed chemical trend with respect to cation size for band gap, with larger values for Si and Sn and smaller values for Ge and Pb. For variations in the B site in the (Ni, Pd, Pt) group the band gap increases with increasing cation size. For variations in the B site in the group of Se and Te, the band gap increases with increasing size.

3.3 Approach

3.3.1 Structures and Chemistries Considered

In this section we provide a brief description of the chemical compositions of the A_2BX_6 inorganic compounds considered in the present computational studies. We focus initially on compounds with the halide anion X=I and consider seven compounds with varying alkali A-site cations and tetravalent B-site cations: K_2PtI_6, Rb_2PtI_6, Cs_2PtI_6, Cs_2PdI_6, Rb_2SnI_6, Cs_2SnI_6 and Cs_2TeI_6. Each of these compounds has been synthesized and characterized experimentally, with crystal structure parameters tabulated in the International Crystal Structure Database(ICSD)[53, 54]. All of these compounds have the cubic (space group $Fm\bar{3}m$) structure illustrated in Fig. 3.1 (b), with the exception of K_2PtI_6, which is tetragonally distorted (space group P4/mnc). From the DFT-GGA results available through the Materials Project [55] these chemistries are expected to yield a range of band gap values that is relevant for photovoltaic applications. For each of these seven compounds we have undertaken computational studies of the electronic structure for both cubic and tetragonal polymorphs, employing the Heyd-Scuseria-Ernerhof HSE06 [30, 32] hybrid functional, as detailed below.

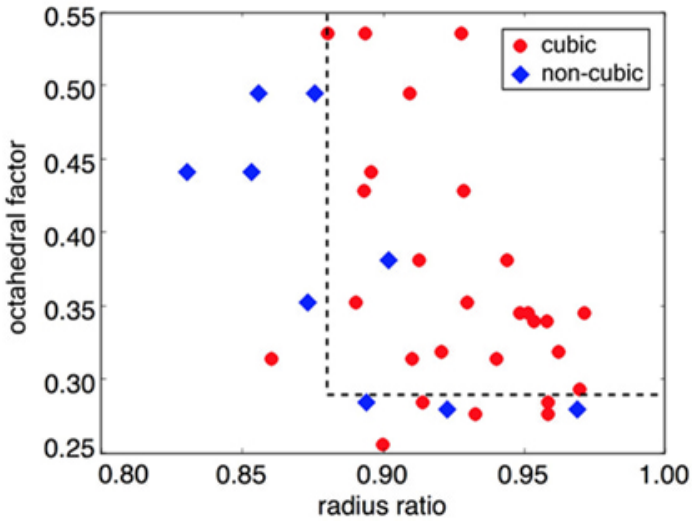

Figure 3.2: A structure map for known A_2BX_6 compounds with A = K, Rb, Cs, B = Si, Ge, Sn, Pb, Ni, Pd, Pt, Se, Te and X = Cl, Br, I. Crystal structures reported in the ICSD are indicated by the different symbols, with red circles and blue diamonds corresponding to cubic and non-cubic materials, respectively. For each material, the octahedral factor is calculated as $\frac{R_B}{R_X}$ and the radius ratio is calculated as $\frac{R_A}{D_{XX}-R_X}$, with R_A, R_B, R_X, D_{XX} representing the radius of A site cation, radius of B site cation, radius of X site anion, and nearest neighbor X-X bond length, respectively. The X-X bond length is calculated from GGA-PBE relaxed structures for the cubic phase for each material. Shannon effective ionic radii for 12-coordinated A^+ cations, 6-coordinated B^{4+} cations, and 6-coordinated X^- anions[56] are used for R_A, R_B and R_X. The dashed line is a guide to the eye that separates the majority of the cubic perovskite structures and distorted non-cubic structures.

To motivate the choice of crystal structures considered in this work, we show in Fig. 3.2 a structure map similar to those used in studies of perovskite-based compounds[57]. The axes in this figure correspond to the octahedral factor and the radius ratio. The octahedral factor is defined as the ratio between B cation radius and X anion radius. The radius ratio is the ratio between the radius of the A site cation and the size of the cavity formed by the neighboring halogen anions[58]. For perovskite compounds the octahedral factor is used empirically to predict the formation of the BX_6 octahedron; and the tolerance factor is used empirically to predict the formation and distortion of the perovksite structure. Likewise, in the A_2BX_6 perovskite-derived structure, we can combine the octahedral factor and radius ratio to predict the formation and distortion of the structure. Small octahedral factors suggest that the formation of BX_6 octahedra are disfavored. A small radius ratio results in distortion of the cavity and a lower symmetry of the structure, or even totally different connectivity of the octahedra network. According to the survey of known A_2BX_6 compounds in the ICSD database[53, 54], shown in Fig.3.2, most known compounds are cubic ($Fm\bar{3}m$) and are indicated by red circles. Because of this, in this work, most of the trends are derived from considerations of cubic ($Fm\bar{3}m$) structures. On the other hand, as shown in Fig.3.2, compounds with smaller radius ratio and smaller octahedral factor tend to form non-cubic structures, as indicated by blue diamond symbols. Among these non-cubic structure compounds, most adopt the tetragonal P4/mnc structure. The crystallographic details of the experimentally observed structures are listed in Table S1 for A_2BX_6 compounds with A=K, Rb, Cs, B=Si, Ge, Sn, Pb, Ni, Pd, Pt, Se and Te, X=Cl, Br, I. In this work, the effect of tetragonal distortions and octahedral rotations are investigated for select compositions by comparing results for the cubic structure with those computed for the tetragonal P4/mnc structure. As shown in Fig. 3.3, the two structures differ by the rotations of octahedra in the a-b plane.

3.3.2 Computational Methods

Calculations were carried out employing spin-polarized HSE06 and PBE-GGA based DFT methods using the Projector Augmented Wave (PAW) method [59], as implemented in the Vienna Ab initio simulation package (VASP)[60–62]. The PAW potentials used in the calculations are the same as those underlying the data provided in Materials Project[55], in order to facilitate comparisons with the results available through this database. The energy cutoff for the plane wave basis for all compounds was set to 520 eV. For cubic structures, self-consistent calculations were carried out with a gamma-centered k-point mesh of 6×6×6. Based on convergence tests for Cs_2SnI_6, Rb_2TeI_6 and K_2PtI_6, this choice of plane-wave cutoff and k-point density is found to be sufficient to provide total energies converged to within 1 meV/atom, lattice constants within 0.01 A, and band gaps within 1 meV. For tetragonal structures, according to the convergence tests for 4 randomly picked compounds, self-consistent calculations were carried out with a gamma-centered k-point mesh of 4×4×4, to maintain the same level of energy convergence as that for the cubic structures. For relaxation and density of state calculations, the tetrahedron method with Blöchl corrections was used for k-space integration. To check the importance of relativistic effects on band gaps, spin-orbit coupling is included using the standard approach in VASP for three representative

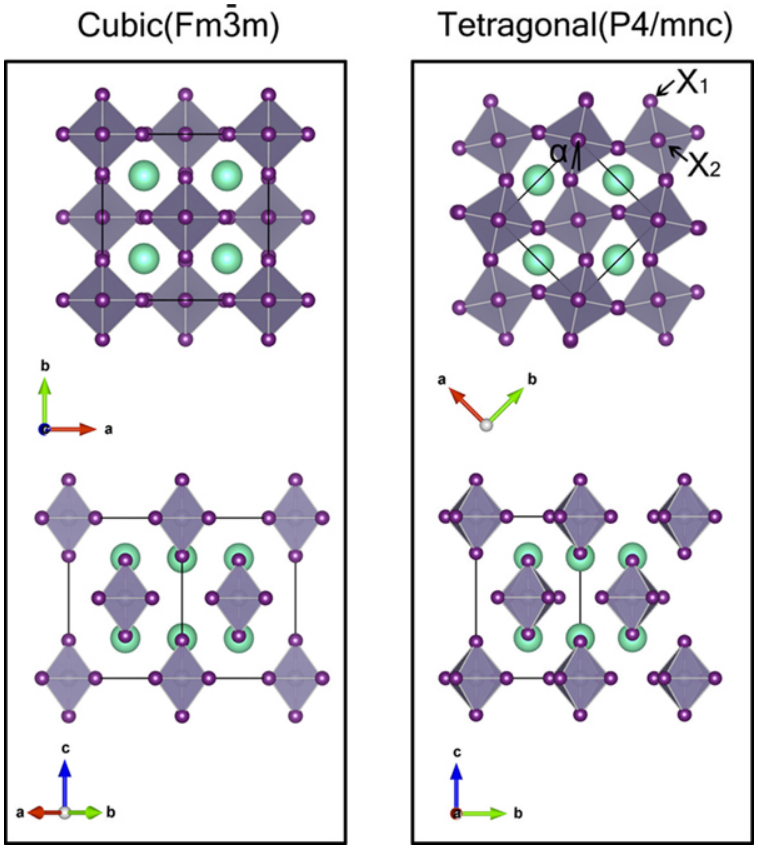

Figure 3.3: Crystal structures for the A_2BX_6 compound in cubic $Fm\bar{3}m$ (left) and tetragonal P4/mnc (right) polymorphs viewed from different directions. Lattice vectors are shown for each structure and orientation. The BX_6 octahedra are shaded, with the purple balls on the corners representing halide cations. The green balls represent the A-site cations. In the tetragonal structure, octahedral rotation angle with respect to cubic structure is labeled as α, equatorial halide as X_1, and apical halide as X_2.

compounds with heavier elements. The self-consistency iterations were performed until the energy was converged to within 1×10^{-5} eV. The structural relaxations were undertaken until the forces were converged within 0.01 eV/A for the GGA-PBE calculations, and within 0.05 eV/A for HSE06. For the compounds containing B-site transition-metal cations (B=Ni, Pd, and Pt) with unfilled d shells in the 4+ charge state, we ran spin-polarized calculations considering both high-spin and low-spin configurations, finding the low-spin (zero local moment) states to be lowest in energy. The HSE06 band structures were calculated self-consistently using a regular Monkhorst-Pack k-grid, with k-points along high symmetry lines added as zero-weight points.

The energy above hull(i.e., the difference in energy between this compound and the compound or phase-separated combinations of compounds that have the lowest energy at the associated composition) for the 81 A_2BX_6 compounds with cubic structures were calculated by retrieving the total energies of all available compounds in A-B-X system from Materials Project, including common allotropes, binaries and some ternaries. The previously described calculation parameters of the 81 A_2BX_6 compounds were chosen to be consistent with those used by Materials Project.

The average effective masses[63] were calculated using the BoltzTrap code[64] and the pymatgen package[65, 63]. Gamma-centered 20×20×20 and 18×18×12 k-point meshes were used for GGA-PBE band structure calculations of cubic and tetragonal structures, respectively. The band structures were then used as input to BoltzTrap code to calculate the conductivity tensor $\frac{\sigma(T,\mu)}{\tau}$, with τ the constant relaxation time, T set to room temperature (300K), and μ the Fermi level. Then averaged effective masses were calculated as $\mathbf{m} = \frac{ne^2\tau}{\sigma}$. As mentioned by Hautier et al[63], the effective mass defined in this way is an average of $\mathbf{m}(i, \mathbf{k})$ around the Fermi level μ, with i the index of band, $\mathbf{k}$ the wave vector. For electron effective mass, μ was set at the conduction band minimum; for hole effective mass, μ was set at the valence band maximum. Convergence of the effective mass values with respect to the density of k-points over which the band structure was sampled was carefully tested and the values were found to be converged to within 1% using a 20×20×20 mesh.

3.4 Results and discussion

3.4.1 Calculated Results for Experimentally Reported A_2BI_6 Compounds

Table 3.1 lists calculated results for the lattice constants of the seven experimentally-reported A_2BI_6 compounds, along with measured values at room temperature. The calculated and measured results agree reasonably well with the GGA-PBE values larger than measurements by as much as 3.3%, and those from HSE06 showing slightly better agreement with deviations of up to 2.5%.

Table 3.2 shows that no appreciable difference of B-X bond length is found between cubic and tetragonal structures. The 5th column of Table 3.2 lists the octahedral rotation angle α as illustrated in Fig. 3.3. The last column lists the energy difference per atom between cubic and tetragonal structures, with positive values indicating that the latter are stable. For Cs_2SnI_6, Cs_2PdI_6, Cs_2PtI_6, Cs_2TeI_6, the energy difference between cubic and the hypothetical tetragonal structures is less than 2 meV/atom, so we only present the results for the cubic

Compound	Structure	GGA-PBE (A)	HSE06 (A)	Exp. (A)
Cs_2SnI_6	cubic	a=8.53	a=8.46	a=8.235[52]
Rb_2SnI_6	cubic	a=8.40	a=8.32	a=8.217[66]
Cs_2PdI_6	cubic	a=8.28	a=8.21	a=8.013[67]
Cs_2PtI_6	cubic	a=8.32	a=8.26	a=8.038[68]
Rb_2PtI_6	cubic	a=8.16	a=8.11	a=7.932[68]
K_2PtI_6	tetragonal	a=7.73	a=7.69	a=7.717[68]
		c=12.15	c=12.05	c=11.454[68]
Cs_2TeI_6	cubic	a=8.60	a=8.51	a=8.275[52]

Table 3.1: Calculated and experimentally measured lattice parameters of seven A_2BI_6 compounds reported in the ICSD. The second and third columns list calculated results obtained by semi-local GGA-PBE and hybrid HSE06 functionals, respectively. The fourth column lists experimental values at room temperature. The structures labeled in the second column correspond to the cubic ($Fm\bar{3}m$) and tetragonal (P4/mnc) polymorphs described in the text.

structures. Among the seven compounds, K_2PtI_6 has the largest α and energy difference, consistent with the fact that it is the only compound that is experimentally observed to form in the tetragonal structure at room temperature.

Band gaps and effective masses of both cubic and tetragonal structures calculated by HSE06 are listed in Tables 3.3 and 3.4, respectively. In these tables, results for the structures that are reported to be stable at room temperature are indicated in bold font. The HSE06 calculated band gaps listed in Table 3.3 span the range of 0.8 to 2.2 eV. For Cs_2SnI_6, Cs_2PtI_6 and Cs_2TeI_6, the effects of spin-orbit coupling (SOC) on the calculated bandgaps were computed and found to lead to at most a reduction of 0.2 eV. For the other compounds, involving lighter ions, these effects are expected to be smaller. The calculated band gap of Cs_2SnI_6 including spin-orbit coupling is 1.011 eV, which is consistent with the value of 0.97 eV reported in the literature using the same computational approach[52]. As pointed out by Maughan et al[52], the calculated band gap is the fundamental band gap, across which the transition is dipole forbidden in Cs_2SnI_6. This explains why the measured band gap is significant larger than calculated values. The calculated band gap value for Cs_2TeI_6 is 0.4 eV larger than measured values, which is comparable to the 0.3 eV mean absolute error of band gaps reported for HSE06 for a semiconductor test set[31]. A HSE06+SOC calculation reported[52] for Cs_2TeI_6 gives an indirect band gap of 1.83 eV. The 0.15 eV discrepancy with our calculated results listed in Table 3.3 may reflect the smaller cutoff energy and k-point density used in the previous calculations.

The present calculated results display clear trends with the size of the A-site cation. Considering first the trends for the cubic structures, the band gap values decrease systematically as the A site varies from Cs to Rb to K. By contrast, the trend is the opposite in the tegrag-

	cubic	tetragonal			
Compound	$B-X/A$	$B-X_1/A$	$B-X_2/A$	α/ deg	ΔE(meV/atom)
Cs_2SnI_6	2.87				
Rb_2SnI_6	2.86	2.86	2.89	9.4	8
Cs_2PdI_6	2.69				
Cs_2PtI_6	2.69				
Rb_2PtI_6	2.68	2.69	2.68	8.7	2
K_2PtI_6	2.68	2.69	2.68	12.0	16
Cs_2TeI_6	2.93				

Table 3.2: Calculated bond lengths and rotation angles of seven A_2BI_6 compounds for both cubic ($Fm\bar{3}m$) and tetragonal ($P4/mnc$) polymorphs from HSE06. The second column lists the B-X bond length for the cubic structures. The next three columns list equatorial B-X bond length, apical B-X bond length and octahedral rotation angle α for tetragonal structures, respectively. The equatorial atom X_1, apical atom X_2 and α are illustrated in Fig.3.3. The last column lists the energy difference between cubic and tetragonal structures.

Compound	$E_{g(HSE-cubic)}/eV$	$E_{g(HSE-SOC-cubic)}/eV$	$E_{g(HSE-tetragonal)}/eV$	$E_{g(exp)}/eV$
Cs_2SnI_6	**1.172** $(\Gamma-\Gamma)$	**1.011**$(\Gamma-\Gamma)$		1.3 - 1.6 [47, 50, 46]
Rb_2SnI_6	**1.021** $(\Gamma-\Gamma)$		1.510$(\Gamma-\Gamma)$	
Cs_2PdI_6	**0.858** $(\Gamma-X)$			
Cs_2PtI_6	**1.472** $(\Gamma-X)$	**1.340**$(\Gamma-X)$		
Rb_2PtI_6	**1.303** $(\Gamma-X)$		1.574$(\Gamma-M)$	
K_2PtI_6	1.195 $(\Gamma-X)$		**1.649**$(\Gamma-M)$	
Cs_2TeI_6	**2.187** $(X-L)$	**1.976**$(X-L)$		1.5 - 1.59 [52, 69]

Table 3.3: Band gaps calculated by the HSE06 functional for seven A_2BI_6 compounds reported in the ICSD. The second and third columns give calculated results for cubic structures with and without spin-orbit-coupling (SOC) contributions includes, respectively. The fourth column gives results for the tetragonal structure.

onal structure. For a given chemistry, the band gap increases in going from the cubic to the tetragonal structure, and the magnitude of this increase is larger for the compounds with the smaller A-site cation. These trends will be discussed further below based on considerations of the nature of the bonding in these compounds.

In Figs. 3.4 - 3.7 we present calculated HSE06 band structures for each of the seven compounds listed in Table 3.3. Each separate figure gives band structures for a set of compounds with a fixed B-site cation. Beginning with Sn-based compounds, Cs_2SnI_6 and Rb_2SnI_6 have both been synthesized and their structures characterized experimentally[66]. Considering first the HSE06 electronic structures of Cs_2SnI_6(Fig.3.4(a)) and Rb_2SnI_6(Fig.3.4(c)) without spin-orbit coupling, both compounds are calculated to be direct gap semiconductors with valence bands derived primarily from I p states, and conduction bands derived from hybridized Sn s and I p states. The direct nature of band gap in Cs_2SnI_6 is consistent both with previous ab initio calculations[46, 49] as well as experiments[46, 47]. The highest valence band for these two compounds are almost dispersionless along $\Gamma - X$ direction. This feature can be understood based on the I p character of the highest occupied valence bands. The symmetry of the associated I p orbitals is t_{1g} at Γ point. The lobes of three t_{1g} orbitals extend in three orthogonal 2D planes perpendicular to the Sn-I bonds($\Gamma - X$ direction). The flat band corresponds to the states derived from the t_{1g} orbital that lies in the perpendicular plane to the given Γ-X direction and have minimal overlap along this direction. When considering spin-orbit coupling, as displayed for Cs_2SnI_6 in Fig.3.4(b), the t_{1g} three-fold degeneracy at the Γ point is lifted and the highest valence bands split into two degenerate higher bands and one lower band. Along $\Gamma - X$, the highest valence band becomes more dispersive with SOC.

We consider next the B=Pd and Pt systems Cs_2PdI_6, Cs_2PtI_6, Rb_2PtI_6, and K_2PtI_6. The latter compound forms in the tetragonal structure while all of the others are cubic[67, 68]. The calculated bandstructures in Fig. 3.5 and Fig. 3.6 show that these compounds are indirect gap semiconductors with valence bands derived primarily from I p states, and conduction bands derived from hybridized Pd/Pt d and I p states. When including SOC for Cs_2PdI_6, as displayed in 3.5(b), the highest valence band along $\Gamma - X$ becomes more dispersive.

We consider finally the Cs_2TeI_6 compound, which is experimentally observed to form in the cubic structure[52]. The calculated bandstructure in Fig. 3.7 shows that this compound is an indirect gap semiconductor with valence bands derived primarily from I p states, and conduction bands derived from hybridized Te p and I p states. These results are consistent with the results reported by Maughan[52]. Comparing the band structures without(3.7(a)) and with(3.7(b)) SOC, the effect of SOC is seen to be that the conduction bands are split and the lowest conduction band becomes less dispersive.

We consider next the results for effective masses listed in Table 3.4. In all seven compounds, holes are found to be heavier than electrons. This result can be understood based on the fact that the valence bands are derived from unhybridized halogen p orbitals, which are less dispersed compared with the conduction bands that are derived from anti-bonding states between halogen anions and B site cations. The trend obtained here is contrary to the case in halide perovskites, where holes are lighter than electrons[70]. The trends in the effective mass values listed in Table 3.4 are correlated with those for the band gaps. Specifically, in

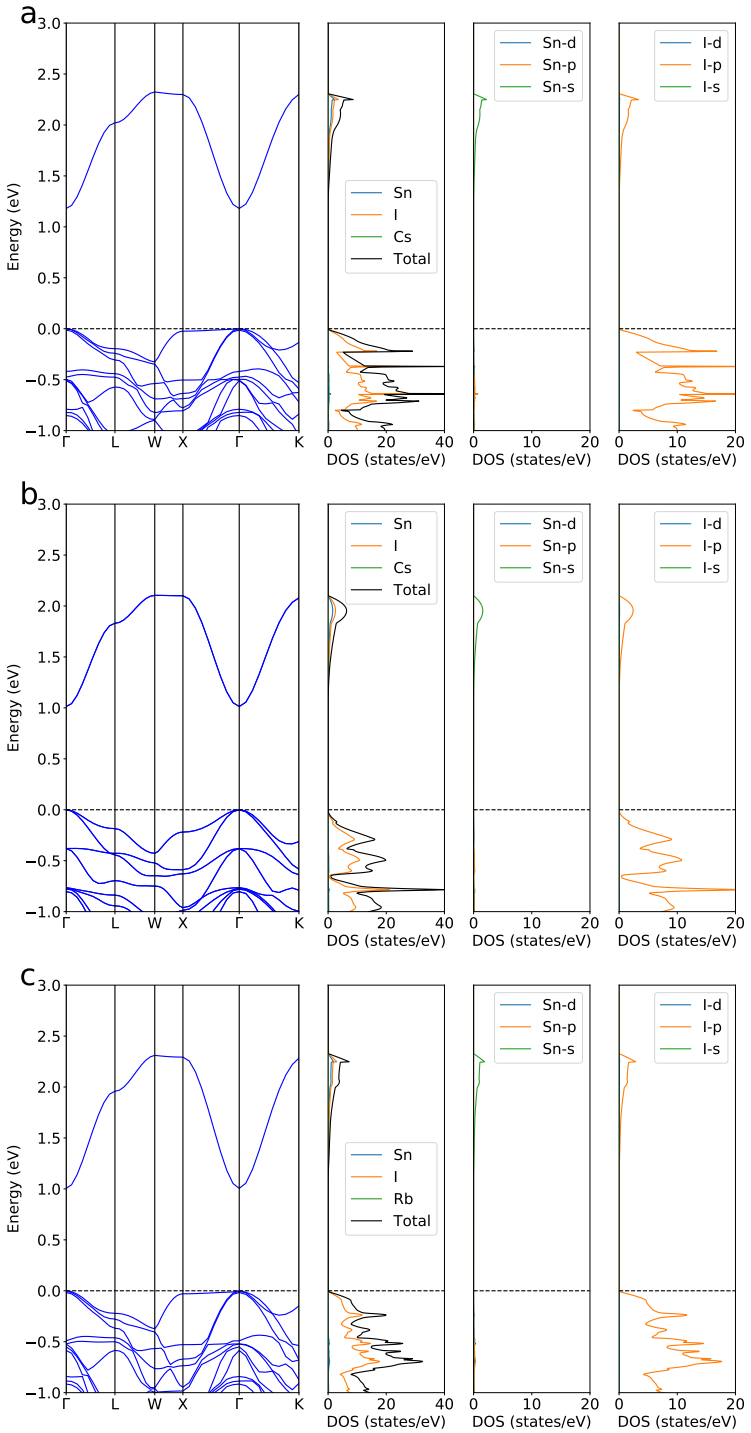

Figure 3.4: Band structures, total and projected densities of states, calculated by HSE06 for the experimentally observed A_2BX_6 compounds with B=Sn and X=I. Results are plotted for (a)Cs_2SnI_6, (b)Cs_2SnI_6 with SOC and (c)Rb_2SnI_6 in the stable cubic ($Fm\bar{3}m$) structure.

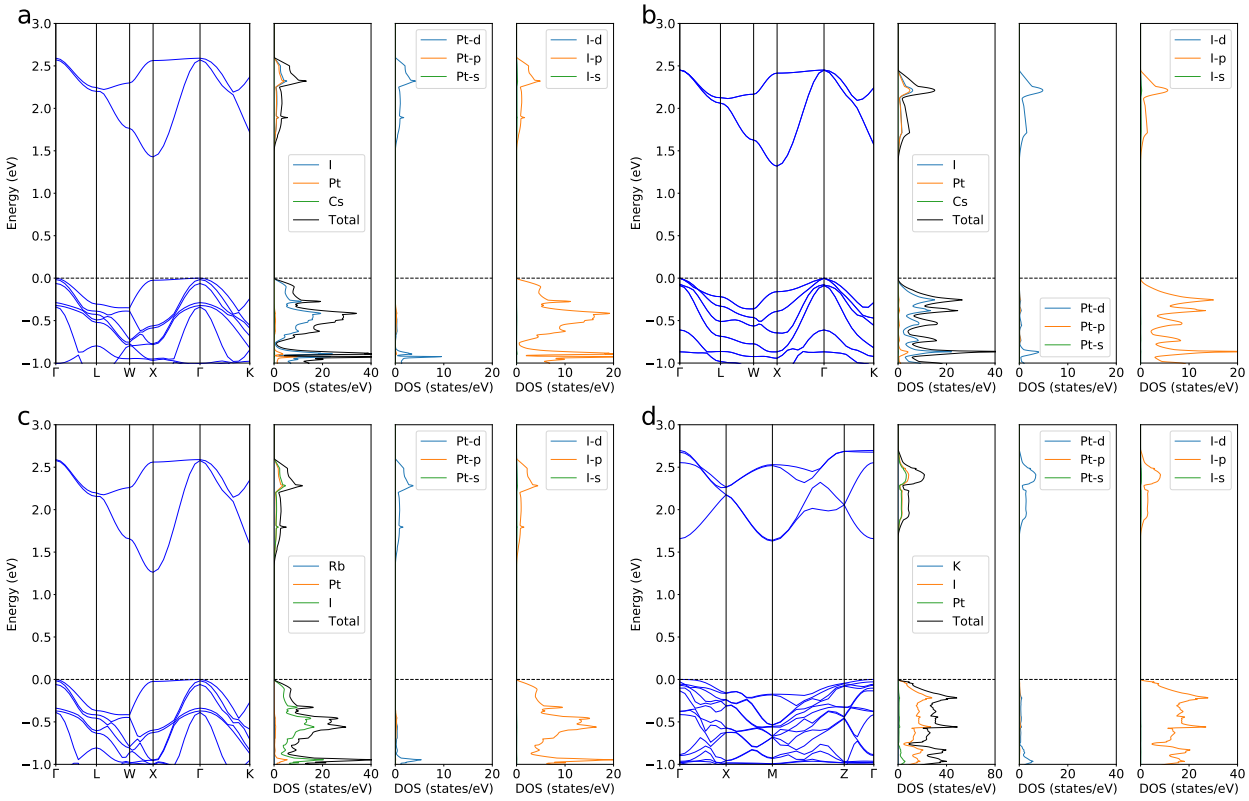

Figure 3.5: Band structures, total and projected densities of states, calculated by HSE06 for the experimentally observed A_2BX_6 compounds with B=Pt and X=I. Results are plotted for (a)Cs_2PtI_6, (b)Cs_2PtI_6 with SOC, (c)Rb_2PtI_6 in the stable cubic ($Fm\bar{3}m$) structure, and for (d)K_2PtI_6 in the stable tetragonal (P4/mnc) structure.

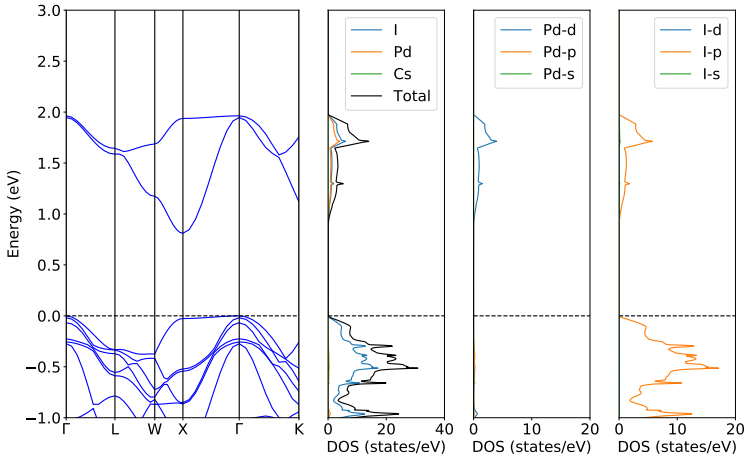

Figure 3.6: Band structures, total and projected densities of states, calculated by HSE06 for the experimentally observed Cs_2PdI_6 compound with the stable cubic ($Fm\bar{3}m$) structure.

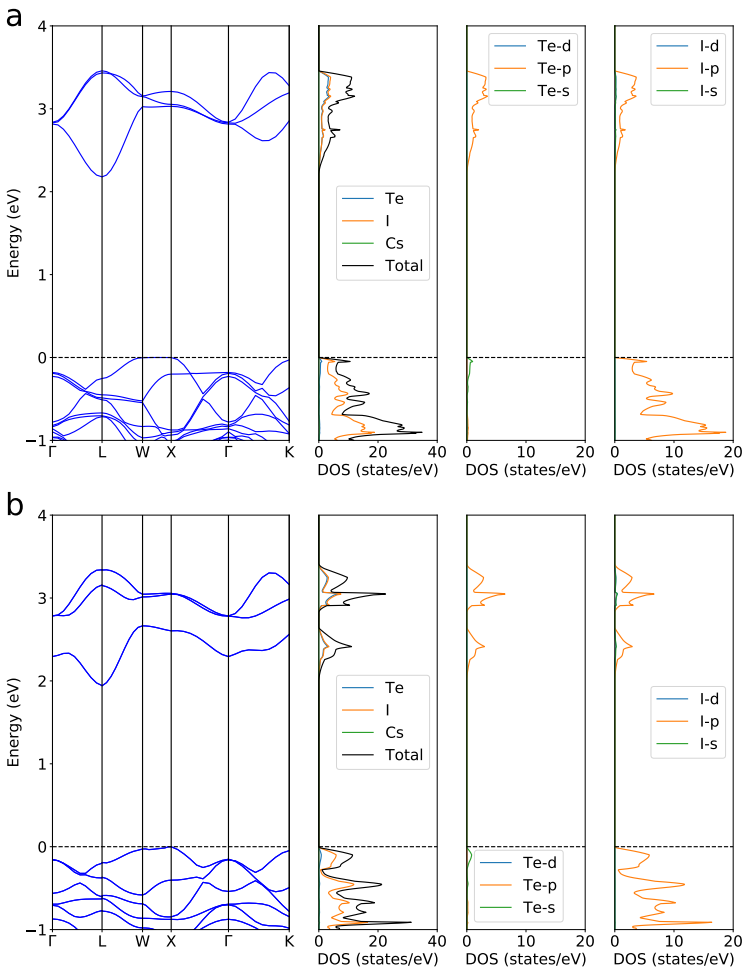

Figure 3.7: Band structures, total and projected densities of states, calculated by HSE06 for the experimentally observed Cs_2TeI_6 compound in the stable cubic ($Fm\bar{3}m$) structure (a)without SOC and (b)with SOC.

cubic structures, for a given B-site cation, reducing the size of the A-site cation leads to a decrease in both the effective mass and the band gap, consistent with the expectations of $k \cdot p$ theory[71]. In tetragonal structures, for a given B-site cation, reducing the size of the A-site cation leads to an increase in both electron effective mass and the band gap. The variations of hole effective masses are more complex because of the presence of multiple valence bands at the band edge.

Compound	$m^*_{e(cubic)}$	$m^*_{h(cubic)}$	$m^*_{e(tetra)[100]}$	$m^*_{e(tetra)[001]}$	$m^*_{h(tetra)[100]}$	$m^*_{h(tetra)[001]}$
Cs_2SnI_6	**0.33**	**1.50**				
Rb_2SnI_6	**0.29**	**1.34**	0.65	0.64	2.61	2.17
Cs_2PdI_6	**0.47**	**1.37**				
Cs_2PtI_6	**0.51**	**1.45**				
Rb_2PtI_6	**0.45**	**1.25**	0.59	0.66	2.50	1.32
K_2PtI_6	0.40	1.15	**0.84**	**0.83**	**1.79**	**2.55**
Cs_2TeI_6	**0.40**	**1.51**				

Table 3.4: Calculatd effective masses for seven A_2BI_6 compounds reported in the ICSD. The results for electrons and holes in the cubic structures are given in columns two and three, respectively. The remaining columns list results for electrons and holes in the tetragonal structure along the two independent crystallographic directions: [100] and [001].

3.4.2 Trends in band gaps and stability across broader compositional ranges

The HSE06 results in the previous section display clear trends in the electronic structure as the compositions of A_2BX_6 are varied with X=I. In this section we investigate these trends over a broader range of 81 total compositions, considering A=(K, Rb, Cs), B=(Si, Ge, Sn, Pb, Ni, Pd, Pt, Se, Te), and X=(Cl, Br, I), using the computationally efficient GGA-PBE method. As shown in Fig. 3.8, which compares results for band gaps obtained from GGA-PBE and HSE06 for the compounds considered in the previous section, the former reproduces the trends from the latter method quite well, even though the semi-local GGA-PBE functional systematically underestimates the band-gap values as expected. The emphasis in the presentation of results in this section is specifically on compositional trends rather than absolute values for the bandgaps. In addition, we present results related to the relative structural stability of the cubic and tetragonal phases of the compounds.

We consider first the geometrical factors of octahedral factor and radius ratio introduced above. Figure 3.9 plots these values for each of the 81 compositions considered, and the results provide insights into why only a small subset of these compositions have been observed to form A_2BX_6 compounds experimentally. For example, it can been seen from Fig. 3.9(a) that B=(Si, Ge, Ni and Se) cations lead to small octahedral factors. For these B-site cations only K_2SeBr_6, Rb_2SeCl_6, Cs_2SeCl_6 and Cs_2GeCl_6 have been reported to form experimentally according to the ICSD [72–74]; no compounds with X=I have been reported, consistent with the smaller octahedral factors characterizing these compounds. The results in Fig. 3.9(b)

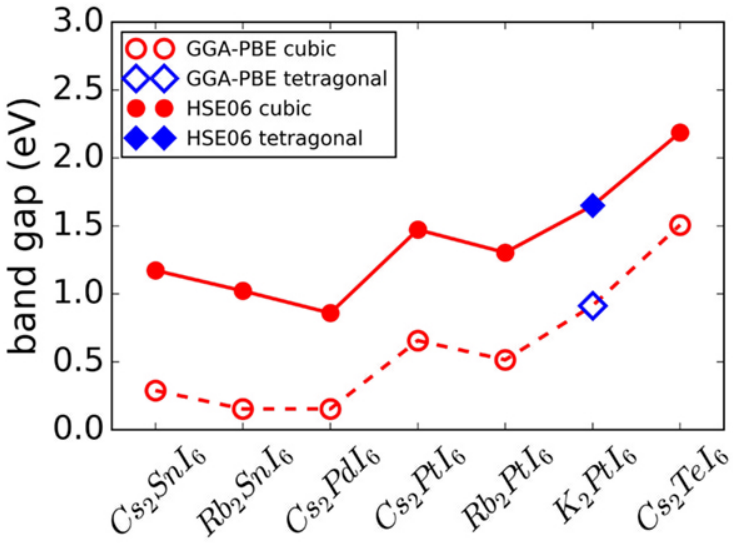

Figure 3.8: Comparison between calculated band gaps obtained with the GGA-PBE and HSE06 methods. The HSE06 calculated band gaps for cubic and tetragonal structures are indicated by filled red circles and filled blue diamonds, respectively. The GGA-PBE calulated band gaps for cubic and tetragonal structures are indicated by open red circles and open blue diamonds, respectively. The solid and dashed lines are guides to the eye.

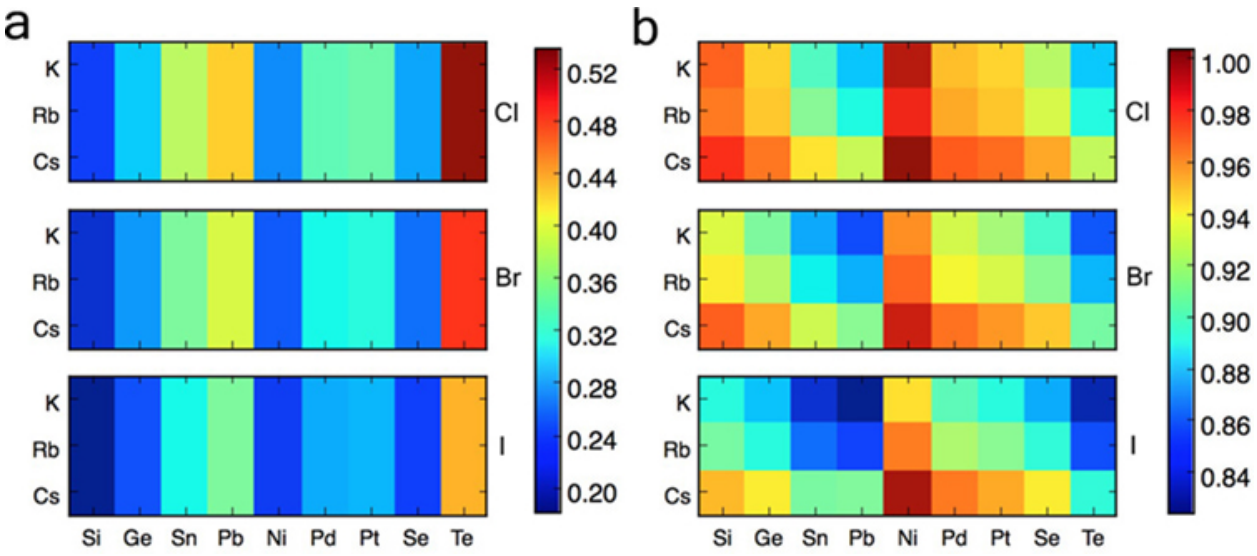

Figure 3.9: A color map of (a)octahedron factor and (b)radius ratio for 81 A_2BX_6 compounds with A = K, Rb, Cs, B = Si, Ge, Sn, Pb, Ni, Pd, Pt, Se, Te and X = Cl, Br, I.

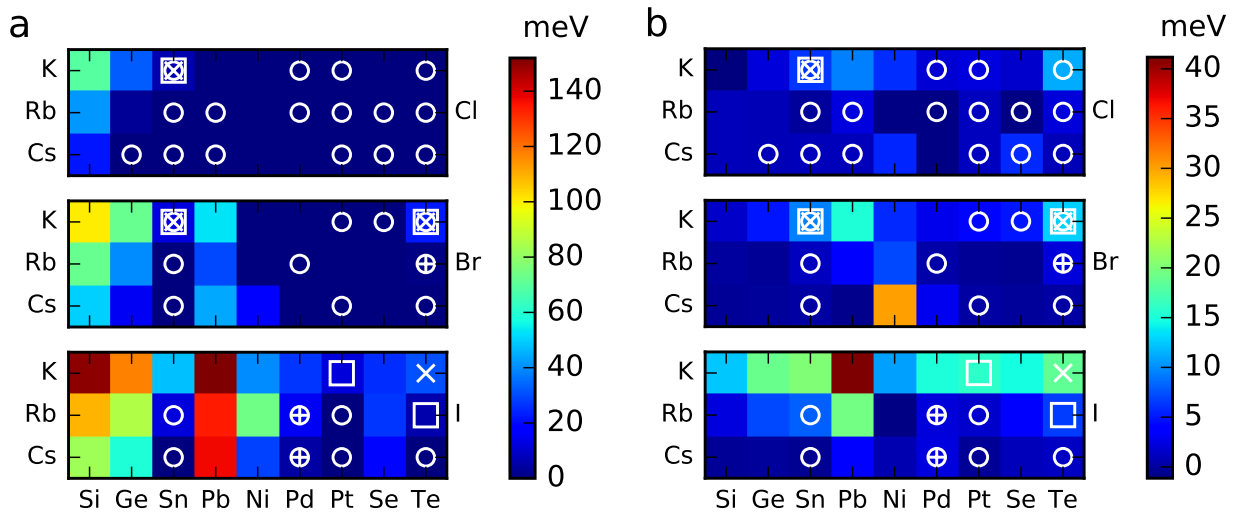

Figure 3.10: A color map of (a) energy above hull for cubic structures and (b) the energy difference per atom of cubic minus tetragonal structures for 81 A_2BX_6 compounds with A = K, Rb, Cs, B = Si, Ge, Sn, Pb, Ni, Pd, Pt, Se, Te and X = Cl, Br, I. Values of zero imply that the tetragonal phase is not stable. Experimentally observed compounds are indicated by symbols: white open circle for cubic($Fm\bar{3}m$) structures, white open square for tetragonal(P4/mnc) structures, white 'X' for monoclinic($P2_1/c$) structures, white '+' for all other structures(Pnma, I4/m, I4/mmm). Note that some compounds exist in multiple phases.

show that the radius ratio decreases systematically for A cations changing from Cs to Rb to K, and for X site cations varying from Cl to Br to I. These results suggest that compounds with A=K and/or X=I are expected to display distorted (non-cubic) phases, which is consistent with the reported non-cubic crystal structures for K_2PtI_6, Rb_2TeI_6, K_2TeI_6 and K_2TeBr_6 in the ICSD [68, 75, 76, 58]. This argument is also supported by calculating the energy difference between cubic and tetragonal structures for the 81 compounds, as displayed in Fig. 3.10(b). The energy of tetragonal K_2BI_6 is significantly lower than the energy of cubic K_2BI_6, indicating the greater tendency to form tetragonal structures for K_2BI_6 compounds.

The energy above hull(E_{hull}) of the 81 cubic A_2BX_6 compounds are displayed as a color map in Fig. 3.10(a), with superimposed white symbols indicating the experimentally observed compounds. These E_{hull} values are also listed in Table S2, together with their decomposition products if $E_{hull} > 0$. From Fig. 3.10(a), it is clear that none of the compounds with large E_{hull} were experimentally observed, among them are iodides with B = Si, Ge, Pb, Ni, bromides with B = Si, Ge, Pb and chlorides with X = Si. All experimentally reported compounds have zero or small values of E_{hull}, and the results suggest additional A_2BX_6 compounds with small E_{hull} that are candidate compounds for experimental synthesis. Note that the calculated E_{hull} values presented here are all for cubic structures, and as a result the compounds which are observed with cubic structures(as indicated by white open circles) generally have a smaller E_{hull} than the compounds which are observed with non-cubic structures(as indicated by non-circle symbols).

Calculated band gaps obtained with the GGA-PBE functional for the 81 compounds

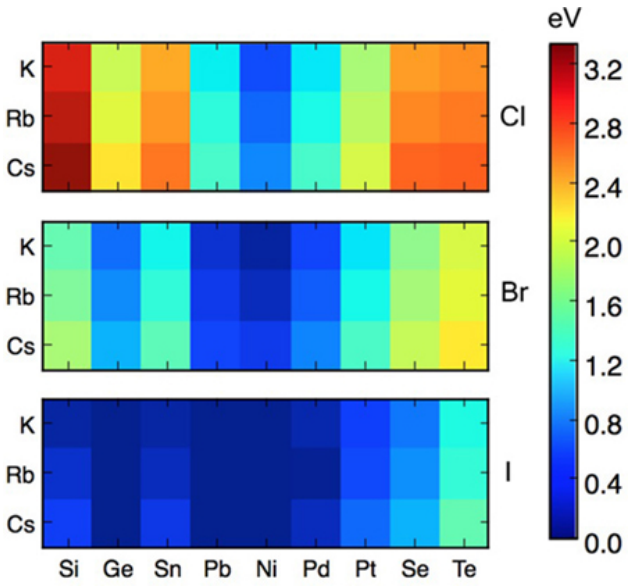

Figure 3.11: A color map of PBE-GGA calculated band gaps for 81 A_2BX_6 compounds in the cubic ($Fm\bar{3}m$) structure, with A = K, Rb, Cs, B = Si, Ge, Sn, Pb, Ni, Pd, Pt, Se, Te and X = Cl, Br, I. The three large blocks respond to Cl, Br and I compounds, respectively.

with ideal cubic structures are plotted in Fig.3.11. The compounds on the 'blue' side have smaller band gaps. Based on a comparison of these GGA-PBE results with the more accurate HSE06 calculations presented in the previous section these materials may have band gaps in the right range for sunlight absorber calculations. Similarly, the compounds such as the chloride shown in red in Fig. 3.11 are expected to be large gap semiconductors/insulators. General chemical trends are apparent in the calculated band gaps with increasing size of A site cation and halogen anion, as demonstrated more explicitly in Fig. 3.12, which includes results for both cubic and tetragonal structures. To reduce the complexity of this figure, only Sn, Pt and Te compounds are shown, however the trends in Fig. 3.11 for compounds with other B-site cations are similar.

The calculated band gaps are shown in Fig. 3.12 (b)-(d) to decrease with increasing size of the halide anion, i.e., from Cl to Br to I. This trend occurs for both cubic and tetragonal structures, and across all of the B and A site combinations presented. The same trend was observed experimentally for Cs_2SnCl_6, Cs_2SnBr_6, and Cs_2SnI_6 with band gaps of 3.9 eV, 2.7 eV and 1.26 eV, respectively[48]. This trend can be understood based on the electronic states at the conduction and valence bands. Taking B=Sn compounds as an example, the conduction band is composed of anti-bonding states between Sn s orbitals and halide p orbitals. With increasing size of the halide anion the Sn-X bonds increase systematically, correlating with a decrease in the splitting between bonding and anti-bonding splitting and a concomitant lowering of the CBM. The VBM is composed of states that are primarily derived from the halide anion p orbitals, and these states are expected to rise in energy with the decreasing electronegativity going from Cl to Br to I. The trend in decreasing band gap with increase size of the halide anion can thus be understood as resulting from a combination of a lower CBM and higher VBM. The bonding picture presented above is consistent with

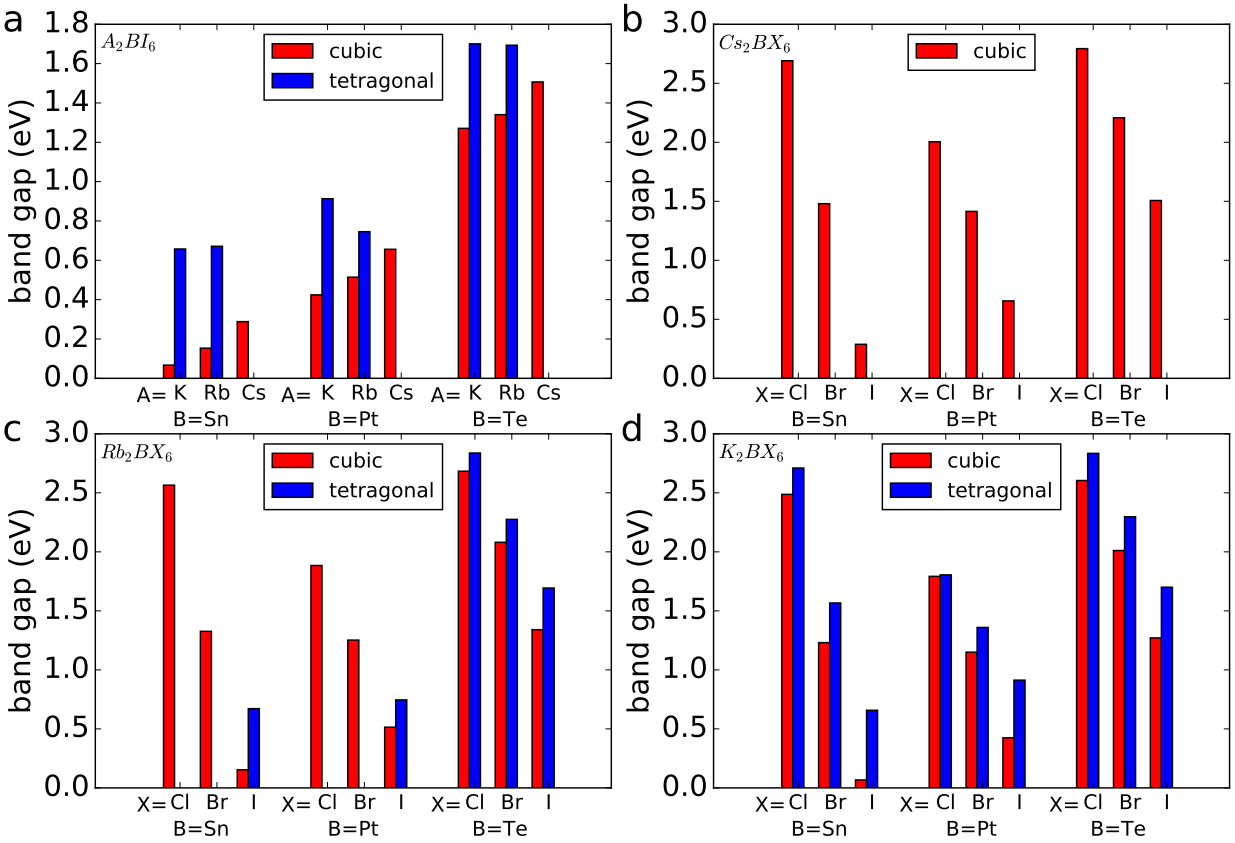

Figure 3.12: Chemical trends for GGA-PBE calculated band gaps in A_2BX_6(A=K, Rb, Cs, B=Sn, Pt, Te, X=Cl, Br, I) compounds with cubic ($Fm\bar{3}m$) and tetragonal (P4/mnc) structures. Band gap values for cubic and tetragonal structures are indicated by red bars and blue bars, respectively. (a)band gap trends with varying size of A site cations in A_2BI_6(A=K, Rb, Cs, B=Sn, Pt, Te); (b)band gap trends with varying size of X site anions in Cs_2BX_6(B=Sn, Pt, Te, X=Cl, Br, I); (c)band gap trends with varying size of X site anions in Rb_2BX_6(B=Sn, Pt, Te, X=Cl, Br, I); (d)band gap trends with varying size of X site anions in K_2BX_6(B=Sn, Pt, Te, X=Cl, Br, I).

that discussed by Xiao et al[49].

The effects of variations of the A-site cation on the calculated band gaps are illustrated in Fig. 3.12 (a) for the case of X=I. The effects are seen to be weaker than those resulting from variations in the halide anion, and they are shown to be qualitatively different for cubic and tetragonal phases. Specifically, the calculated band gaps are found to increase and decrease for cubic and tetragonal structures, respectively, with increasing A-site cation size. For the cubic phases the results can be understood as arising from the effect of the A-site cation on the distance between neighboring I sites. As the size of the A-site cation increases, the distance between neighboring I sites increases, while the B-X bond lengths in the BI_6 octahedra remain largely unchanged. Increasing I neighbor distances correlate with a narrowing of the I-p band and thus a lowering of the VBM, consistent with the increase in band gap from K to Rb to Cs.

We consider next the trends with A-site cation for the tetragonal structures. For the smaller A-site cations (K and Rb) the tetragonal structure is lower in energy and the band gap larger than that for the corresponding cubic phase. With decreasing size of the A site cation, the degree of octahedral rotation (c.f., Fig. 3.3) increases, which leads to a decrease in the bonding strength between neighboring halide-ions as their p orbitals increasingly point away from each other. The larger band gap for the smaller A-site cation in the tetragonal phase thus correlates with a resulting narrowing of the valence band.

3.5 Summary

First-principles calculations employing the hybrid HSE06 method have been undertaken to compute the electronic structures of seven perovskite-derived A_2BI_6 compounds, considering B=Sn, Pd, Pt and Te cations. Calculated band gaps and effective masses of cubic structures decrease as the A site cation size decreases. These trends were explored over a broader range of A_2BX_6 halide chemistries, considering in total 81 combinations of A(=K, Rb, Cs), B=(Si, Ge, Sn, Pb, Ni, Pd, Pt, Se, Te) and X(=Cl, Br and I) ions, employing semi-local GGA-PBE calculations. The results show that the trend of increasing band gaps with decreasing size of the halide anion holds across the compounds, for both cubic and tetragonal structures. The effect of A-site cations is more complex. Within the cubic structure, decreasing size of the A-site cation leads to a decrease in the calculated band gap, while also favoring structural distortion associated with the rotation of the BX_6 octahedra in the tetragonal phase, which has the effect of increasing the calculated band gap.

The trends identified in this computational study provide guidelines for the use of substitutional alloying as a means of tuning band gaps and structural stability for use of A_2BX_6 compounds in applications such as solar photo-absorbers. For example, alloying of Cs_2BX_6 with Rb_2BX_6 could be expected to give rise to increasing rotation of the BX_6 octahedra and an increase in the band gap. Similarly, as already demonstrated by McMeekin et al[77], alloying of both A and X sites can be expected to be effective in tuning both bandgap and structural stability. We note that alloying of B site Sn and Te cations has also been explored in this context [52]. The general trends in band gaps and structural stability identified in this computational study are anticipated to be helpful in guiding further work in these directions.

3.6 Acknowledgement

This work was funded by National Research Foundation (NRF), Singapore (CRP NRF2014NRF-CRP002-036) and the Singapore-Berkeley Research Initiative for Sustainable Energy (SinBeRISE) CREATE programme. This work made use of computational resources provided under the Extreme Science and Engineering Discovery Environment (XSEDE), which is supported by the National Science Foundation grant No. OCI-1053575.

Chapter 4:

High-throughput Computational Study of Halide Double Perovskite Inorganic Compounds

4.1 Abstract

Double perovskite halides are a class of materials with diverse chemistries that are amenable to solution-based synthesis routes, and display a range of properties for a variety of potential applications. Starting from a consideration of the octahedral and tolerance factors of ∼2000 candidate double-perovskite compounds, we compute structural, electronic and transport properties of ∼1000 using first-principles calculations based on density-functional-theory methods. The computational results have been assembled in a database that is accessible through the Materials Project online. As one potential application, double perovskites are candidates in the search for lead-free halide photovoltaic absorbers. We present the application of our database to aid the discovery of new double perovskite halide photovoltaic materials, by combining the results with optical absorption and phonon stability calculations. Eleven compounds from three distinct classes of chemistries were identified as promising solar absorbers and the complex chemical trends for band gap within each of these are analyzed, to provide guidelines for the use of substitutional alloying as a means of further tuning the electronic structure. Other possible applications of the database are also discussed.

4.2 Introduction

Double perovskite halides($A_2MM'X_6$) are a class of compounds that can span diverse chemistries. The crystal structure(Figure 4.1(a)) is formed by corner-sharing octahedra with M or M′ atoms at the centers and X atoms at corners. M and M′ centers are ordered as second neighbors over the simple cubic cation sublattice and A atoms are in the center of eight neighboring octahedra. Due to their diverse chemistries, the family of halide double perovskites display a range of electronic properties, making them candidates for a variety

The results presented in this chapter and appendix B have been published as a regular article with title "*High-throughput Computational Study of Halide Double Perovskite Inorganic Compounds*" in Chem. Mater. 2019, 31, 15, 5392-5401 by Yao Cai, Wei Xie, Yin Ting Teng, P.C. Harikesh, Biplab Ghosh, Patrick Huck, Kristin A. Persson, Nripan Mathews, Subodh G. Mhaisalkar, Matthew Sherburne, and Mark Asta[78]. The material is presented here with the permission of co-authors and publishers.

of applications, including photo-absorbers for solar cells, ultraviolet(UV) photodetectors, X-ray detector, and scintillators, etc. For example, thin film $Cs_2AgBiBr_6$ photovoltaic devices have been demonstrated with Power Conversion Efficiency(PCE) close to 2.5% and an open circuit voltage exceeding one volt[79]; additionally, sensitive and fast UV photodetectors based on $Cs_2AgInCl_6$ single crystals[80] and low detection limit X-ray detectors based on $Cs_2AgBiBr_6$ single crystal have been demonstrated[81], respectively; further, use of Cs_2LiYCl_6 has been demonstrated for detection of Gamma rays, thermal and fast neutrons simultaneously[82]. The wide interest and variety of potential applications of these compounds has motivated the current work, in which we have employed high-throughput computing using density-functional-theory (DFT) based approaches to develop an open and searchable double perovskite halide database, which has been incorporated into Materials Project database[55].

One of the applications of double perovskite halides that has received significant attention recently is as absorber materials for solar cells[44]. Many experimental and computational investigations related to such applications have been published since 2016. Single crystals of $Cs_2AgBiBr_6$(indirect band gap 1.95 eV) were synthesized and shown to have a long room-temperature fundamental photoluminescence(PL) lifetime of 660 ns, high defect tolerance and better heat and moisture stability compared with $(MA)PbI_3$[83]. Another work demonstrated long electron-hole diffusion length(> 100 nm) in $Cs_2AgBiBr_6$ solar cell devices with over 1% PCE[84]. The hybrid double perovskite $(MA)_2AgBiBr_6$ with a band gap of 2.02 eV was also synthesized[85]. $Cs_2AgBiCl_6$ was synthesized and measured to possess an indirect band gap of 2.2[86] $\sim$ 2.77 eV [87], and Cs_2AgBiI_6 with a smaller 1.75 eV band gap was synthesized as nanocrystals via anion-exchange[88]. A similar compound $Cs_2AgSbCl_6$ with an indirect band gap(2.54 eV) [89] was also synthesized. Another double perovskite $(MA)_2KBiCl_6$ was synthesized and found to have a large indirect band gap of 3.04 eV[90]. Indirect band gaps are not ideal for photovoltaic applications, and direct band gap materials are desired[91]. Single crystal $(MA)_2TlBiBr_6$ was synthesized and found to have an direct band gap of 2.0 eV[92]. $Cs_2AgInCl_6$, a direct band gap compound with parity-forbidden band gap of 2.1 eV and absorption onset of 3.2 eV[80] was shown to be photosensitive to UV light[93], and to possess good moisture, light and heat stability[94].

As a means for further optimizing the properties of double perovskites for device applications, substitutional alloying or doping is expected to be a useful strategy. Band engineering with impurities in this system can dramatically alter band edge structure. Dilute alloying of Tl into both Ag and Bi sites of $Cs_2AgBiBr_6$ decreases its band gap by 0.5 eV, with long-lived carriers with micro-second lifetimes[95]. 75%In and 37.5%Sb can be alloyed into the host $Cs_2AgBiBr_6$ with In-Bi alloying increasing the band gap and Sb-Bi alloying decreasing the band gap to 1.86 eV at most[96]. Solid solutions between $Cs_2AgSbCl_6$ and $Cs_2AgInCl_6$ can be tuned to have either direct(below 40%Sb) or indirect(above 40%Sb) band gaps[89]. A DFT study indicates that $Cs_2BiAg_{1-x}Cu_xCl_6$ mixtures should be amenable to synthesis with the band gap between 1.6 $\sim$ 1.9 eV[97]. Another DFT study indicates that mixed-cation $(Cs/MA/FA)_2InBiBr_6$ halide double perovskites have optoelectronic properties comparable to $MAPbI_3$[98].

Several previous investigations have focused on the use of computational methods to screen double perovskites for photovoltaic applications. Two double perovskites $Cs_2InSbCl_6$

and $Cs_2InBiCl_6$ isoelectronic to Pb halides(ns^2np^0) were proposed as promising candidates due to their good theoretical maximum solar cell efficiencies[99, 100]. Also proposed were three other double perovskites $Cs_2AgInBr_6$, $Rb_2AgInBr_6$ and $Rb_2CuInCl_6$ that have direct band gaps with close to optimal values for solar absorbers [101, 102]. $Rb_2AgInCl_6$ and $Cs_2AgInCl_6$ with larger direct band gaps were also identified computationally[103]. A mixed valence $Cs_2Au_2I_6$(i.e., $Cs_2Au^{1+}Au^{3+}I_6$) compound was synthesized[104, 105] and was measured to have an optical gap of 1.31 eV[106]. In another high pressure study, it was shown to have a band gap near 0.6 eV at 1.5GPa[107]. In a first-principles computational study, this compound was shown to be a direct gap semiconductor with a 1.21 eV band gap[108].

The experimental and computational research reviewed above has focused on ~ 50 halide double perovskite compositions, which is a relatively small subset of the large number of possible compositions. Consequently, an expanded computational screening effort that considers a wider range of chemical combinations is worthwhile. In this work, we have performed DFT based high-throughput calculations considering $\sim$1000 halide double perovskites. Based on our calculations we have developed a double perovskite database, including all calculated structural information, energetics, and band gaps. The database covers chemistries identified starting with $\sim$2000 candidate double perovskite compositions, considering empirical structural factors. These structural stability considerations lead to a down select to $\sim$1000 compositions for which we employed semi-local DFT functionals to perform electronic structure calculations to obtain thermodynamic stability and a rough estimate of band gaps.

As an example of the use of this database, we present an application in screening for possible new photovoltaic(PV) materials and explore trends underlying the variation of electronic structure with chemical composition. 30 double perovskites from five categories are identified as possible candidates as solar absorbers. For these compounds we employ hybrid-functional methods with spin-orbit coupling to calculate and analyze the electronic structures in more detail. The important parameters for PV applications, such as band gaps, effective masses, absorption spectra, conversion efficiency and phonon stability, are calculated. Eleven compounds from three classes of chemistries that are anticipated to be thermodynamically and structurally stable and have theoretical conversion efficiencies larger than 10% are identified. Several compounds from two of the three classes have been reported in previous experimental or computational studies (A_2AgInX_6[80, 93, 94, 103], A_2CuInX_6[101], A_2TlBiX_6[92], A_2InBiX_6[99] and A_2InSbX_6[99], etc), and our screening results are consistent with these reports. Furthermore, we propose one new category of compounds in this work: $A_2MM'X_6$ with M=In, Tl, M′=Al, Ga, In, Tl. For each of the three classes, chemical trends of band gaps are discussed, to provide guidance for design of solid solutions that may enable further tuning of properties.

4.3 Database Details

In this section we describe the methods underlying the development of the double perovskite computational database, the results of screening based on consideration of tolerance and octahedral factors to identify the chemistries considered, and an overview of the database information. The database of calculated values can be accessed through the Materials Project website(DOI: 10.17188/1476059, link:

https://materialsproject.org/materials/10.17188/1476059).

4.3.1 Computational Methods

Calculations were carried out employing HSE06 and PBE-GGA based DFT methods using the Projector Augmented Wave (PAW) method [59], as implemented in the Vienna Ab initio simulation package (VASP)[60–62]. The workflow used in this study was developed to consider the possibility of extending to broader ranges of chemistries, including those where spin-polarized groundstates might be expected; as a consequence, all calculations were performed spin-polarized even though all of the resulting ground states were non-magnetic. The PAW potentials used in the calculations are the same as those employed in the calculations underlying the data in Materials Project[55], in order to facilitate comparisons with the results available through this database. The self-consistency iterations were performed until the energy was converged to within 1×10^{-5} eV. Structural relaxations with respect to cell volume and ionic coordinates(ISIF = 3 in VASP) were undertaken until the forces were converged within 0.01 eV/A for the GGA-PBE calculations, and within 0.05 eV/A for hybrid functional calculations. Symmetry for the space group $Fm\bar{3}m$ was kept throughout the relaxations. For some compounds, the ground state may be structurally distorted with lower symmetry[109, 105, 110]; in applications of the database promising structures can be further examined for such structural distortions as demonstrated below. The energy cutoff for the plane wave basis for all compounds was set to 520 eV. Relaxation calculations were carried out with a gamma-centered k-point mesh of 5×5×5. Based on our convergence tests, this choice of plane-wave cutoff and k-point density is found to be sufficient to provide total energies converged to within 1 meV/atom, and lattice constants within 0.01 A.

To obtain more accurate electronic structures for select compounds, band structures and density of states were calculated by PBE with spin-orbit coupling (SOC) corrections, with conduction bands corrected to match the HSE06+SOC band gaps employing a simple "scissor operator". Spin-orbit coupling was included using the approach available in VASP. For density of states calculations, a gamma-centered k-point mesh of 10×10×10 and the tetrahedron method with Blöchl corrections[111] was used for k-space integration. For band structure calculations, k-points were sampling along high-symmetry lines in the Brillouin zone.

The energy above hull(i.e., the difference in energy between a given compound and the compound or phase-separated combinations of compounds that have the lowest energy at the associated composition) was calculated by retrieving the total energies of all available compounds in A-M-M′-X system from Materials Project, including common allotropes, binary and ternary compounds. The average effective masses[63] were calculated using the BoltzTrap code[64] and the pymatgen package[65, 63]. Gamma-centered 20×20×20 k-point meshes were used for GGA-PBE band structure calculations. The band structures were then used as input to the BoltzTrap code to calculate the conductivity tensor $\frac{\sigma(T,\mu)}{\tau}$, with τ the constant relaxation time, T the absolute temperature (set to 300 K), and μ the Fermi level. Then averaged effective masses were calculated as $\mathbf{m} = \frac{ne^2\tau}{\sigma}$. As mentioned by Hautier et al[63], the effective mass defined in this way is an average of $\mathbf{m}(i, \mathbf{k})$ around the Fermi level μ, with i the index of the band and $\mathbf{k}$ the wave vector. For electron effective mass, μ was

set at the conduction band minimum; for hole effective mass, μ was set at the valence band maximum. Convergence of the effective mass values with respect to the density of k-points over which the band structure was sampled was carefully tested and the values were found to be converged to within 1% using a 20×20×20 mesh.

Absorption spectra were calculated from the frequency dependent dielectric function within the independent-particle picture with PBE functionals, and corrected by the scissor operator to match the HSE band gap values. The number of bands(NBANDS) used in the calculations are 4 times of the number of occupied bands. Gamma-centered 10×10×10 k-point meshes were used in the calculation. The spectroscopic limited maximum efficiency(SLME) was calculated based on the absorption spectra, following an approach due to Yu and Zunger[112].

To investigate structural stability, phonon spectra were calculated using the finite-displacement method employing VASP with the Phonopy package[113]. The primitive structures were first relaxed with a higher force-tolerance criterion of 10^{-4} eV/A. A 2×2×2 supercell and a 4×4×4 k-point mesh were used for the finite displacement calculations.

4.3.2 Chemistries Considered

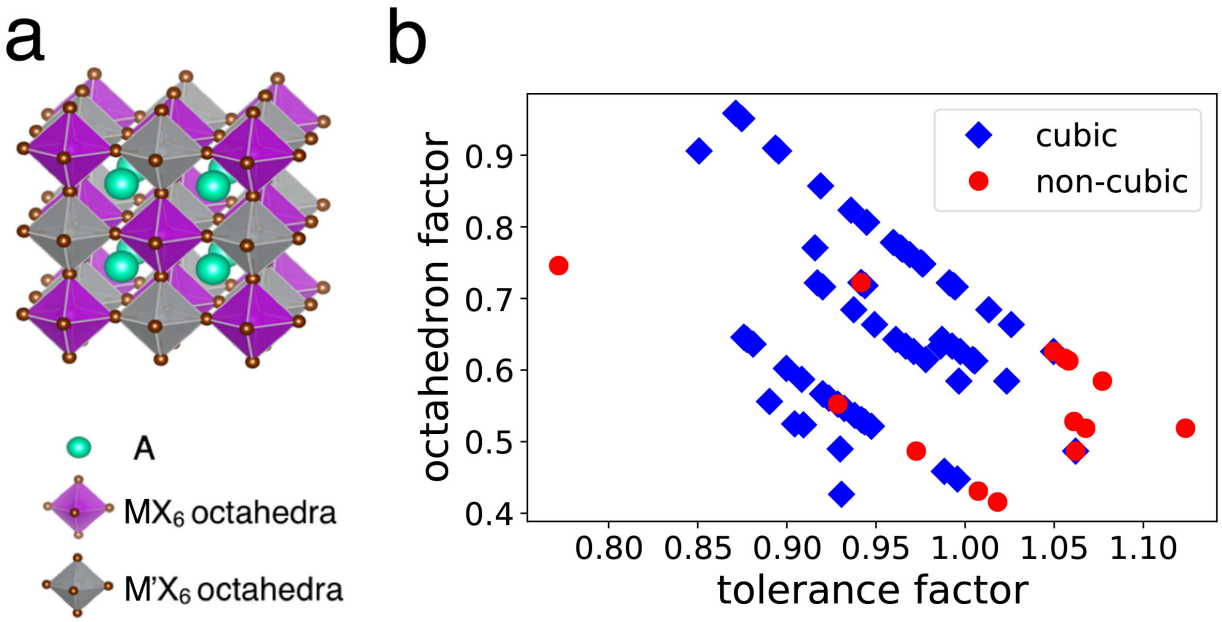

Figure 4.1: (a) Crystal structure of the cubic double-perovskite compound with composition $A_2MM'X_6$. (b) A structure map for known halide $A_2MM'X_6$ compounds. Crystal structures reported in the ICSD are indicated by the different symbols, with blue diamonds and red circles corresponding to cubic and non-cubic materials, respectively. For each material, the octahedral factor is calculated as $\frac{R_M+R_{M'}}{2R_X}$ and the tolerance factor is calculated as $\frac{R_A+R_X}{\sqrt{2}((R_M+R_{M'})/2+R_X)}$, with R_A, R_M, $R_{M'}$, R_X representing the radii of the A, M and M' site cations and the X site halide anion, respectively. Shannon effective ionic radii for 12-coordinated A^{1+} cations, 6-coordinated M^{1+} and M'^{3+} cations, and 6-coordinated X^{1-} anions[56] are used for R_A, R_M, $R_{M'}$ and R_X.

In this section we provide a brief description of the chemical compositions of the $A_2MM'X_6$ inorganic compounds considered in the present computational study. We start by considering 1980 double perovksite compounds of the elpasolite type(Fig. 4.1(a)) with alkali atoms A=Li, Na, K, Rb, Cs, monovalent cations M=Li, Na, K, Rb, Cs, Cu, Ag, Au, Hg, In, Tl, trivalent cations M′=Sc, Y, Al, Ga, In, Tl, As, Sb, Bi and the halide anions X=F, Cl, Br, I. To further motivate the choice of structure and chemistries considered in the calculations, we show in Figure 4.1(b) a structure map similar to those used in studies of perovskite-based compounds[57]. The axes in this figure correspond to the octahedral factor and the Goldschmidt's tolerance factor.

The octahedral factor is defined as the ratio between average (M,M′) cation Shannon radii for 6-fold coordination and X anion Shannon radius for 6-fold coordination[56]. The tolerance factor is calculated by replacing the M radius in the standard expression for the perovskite tolerance factor[114] with the average radius of (M,M′). For perovskite compounds the octahedral factor is used empirically to predict the formation of the MX_6 octahedron; and the tolerance factor is used empirically to predict the formation and distortion of the perovksite structure. Likewise, in the $A_2MM'X_6$ double perovskite structure, we can combine the octahedral factor and tolerance factor to predict the formation and distortion of the structure.

Small octahedral factors suggest that the formation of MX_6 octahedra are disfavored. According to the survey of known $A_2MM'X_6$ compounds in the ICSD database[53, 54], shown in Fig.4.1(b), most known compounds are face-centered cubic ($Fm\bar{3}m$) and are indicated by blue diamonds. Thus, this work focuses on the consideration of such cubic structures with a $Fm\bar{3}m$ space group. On the other hand, as shown in Fig.4.1(b), compounds with larger tolerance factor and smaller octahedral factor tend to form non-cubic structures, as indicated by red circle symbols. The crystallographic details of the experimentally observed double perovskite structures are listed in Table B.1. The limits of the octahedral factor and tolerance factor for cubic structures indicated by the above survey are used empirically as the first screening criteria to reduce the 1980 compounds by approximately half, to a number of 1,149 compounds selected for further consideration by DFT-based methods. The limits set for tolerance factor is (0.82, 1.08) and for octahedral factor (0.4, 1.0). More discussions on tolerance factor and octahedral factor can be found in the Supporting Information, where we also consider the implications of the use of a modified set of ionic radii due to Travis et al.[115]

4.3.3 Overview of Database

In Figure 4.2(a) we present the distribution of the calculated energy above hull and PBE band gap of all double perovskite halides that are within the determined limits for tolerance factor and octahedral factor identified in the previous section. In a survey by Sun et al[116], for experimentally observed fluorides, chlorides, bromides and iodides, the energies above hull are under 100, 50, 30, 25 meV/atom, respectively. In the current study, we used these thresholds to screen for stable or metastable compounds. It should be pointed out that the Materials Project database does not contain all possible decomposition products for some of the compounds, so that the calculated energy above hull serves only as a lower bound such

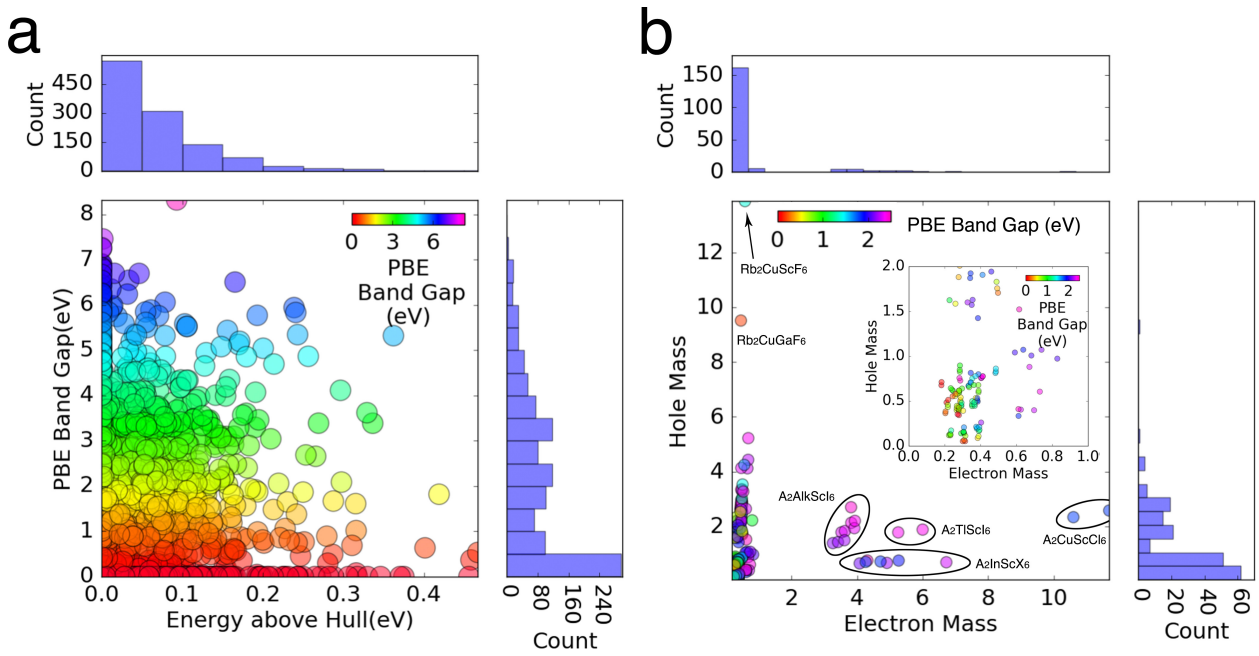

Figure 4.2: (a) Distribution of calculated energy above hull and PBE band gap. The scatter plot illustrates the distribution of calculated energies above hull and band gap values for 1,149 cubic double perovskite halide compounds. The histograms quantify the distribution of the calculated values for the compounds considered. (b) Distribution of calculated effective mass and PBE band gap values. The scatter plot illustrates the distribution of electron mass and hole mass for 189 double perovskite halides with $E_{hull} < 50$ meV/atom and $0.1 < E_g < 2.5$ eV. The histograms quantify the distribution of the calculated values for the compounds considered. Inset: zoom-in view showing only materials with small effective masses.

that the actual thermodynamic (meta)stability could be lower than predicted. It should also be pointed out that these are zero-temperature calculations and the stability could be altered by finite-temperature contributions to the free energy. In other words, some of the compounds that are predicted to be unstable at 0K might turn out to be stable at room temperature due to the entropy terms in free energy. Consideration of finite-temperature stabilities can be undertaken as further efforts in applications of the database studied here, which are limited to zero-temperature properties. Related to finite temperature effects, practical applications of halide perovskites are often limited by their stability in air and moisture and the examination of such effects computationally would again require additional efforts to compute reaction energetics that outside the scope of the database presented here.

Employing the bounds on energy above hull (i.e., considering only flourides, chlorides, bromides and iodides with energy above hull lower than 100, 50, 30, 25 meV/atom, respectively) narrows down the search space for synthesizable double perovksite halides to 238 flourides, 161 chlorides, 107 bromides and 37 iodides(543 in total). The calculated PBE band gaps of these 543 compounds span from 0 to 8 eV, which indicates a rich variety of electronic properties, covering metals, semiconductors and large-gap insulators. Out of the 543 compounds, 62, 171, and 310 have PBE-calculated band gaps(E_g) of 0, $0 < E_g < 2.5$, $E_g \geq 2.5$, respectively. From the scatter plot in Fig. 4.2(a) we can observe that compounds with the highest values of the energy above hull (i.e., more unstable) are more likely to be those predicted as metals.

To evaluate the transport properties of these compounds, we have calculated effective masses. In Figure 4.2(b) we presented the distribution of effective masses and PBE band gaps of 189 double perovskite halides with the energy above hull(E_{hull}) having values $<$ 50 meV/atom and $0.1 < E_g < 2.5$ eV. Interestingly, most of the compounds have very small electron effective masses(167 compounds with $m_e < 1$), but overall a relatively broad distribution of hole effective masses. The groups of outliers are indicated in the scatter plot, and most of them have Sc as the M′ cation. It is interesting that Sc compounds have such a broad range of effective mass values. For example, Rb_2CuScF_6 has very small electron mass and very large hole mass, while $Rb_2CuScCl_6$ has very large electron mass and an intermediate value of hole mass. The hybridization in Sc-Cl and Cu-Cl states is relatively stronger than for Sc-F and Cu-F, so Cu-d band(valence band) and Sc-d band(conduction band) are narrower in Rb_2CuScF_6 than in $Rb_2CuScCl_6$, thus the effective mass should be larger in Rb_2CuScF_6, which is true for hole mass. However, it happens that in Rb_2CuScF_6 at the conduction band edge there is also some hybridization from Cu-s and F-s, which contributes to a very small electron mass. In $Rb_2CuScCl_6$, the Cu-s and Cl-s also hybridize, but the energy level is higher than the conduction edge, and thus has no contribution to electron effective mass. Other Sc compound outliers in Figure 4.2(b) generally have large eletron mass due to the narrow Sc-d band that dominates the character of the conduction band edge. Notably, $M/M' = In/Sc$ compounds have small hole masses due to strong In-s/X-p hybridization at the valence band, and might be good for hole transport materials. In the current study, we are particularly interested in materials with low electron and hole masses, so in the inset of Figure 4.2(b) we show only the compounds with small effective masses. There is a rough trend that compounds with larger band gap(represented by purple/blue dots) have larger effective masses than compounds with smaller band gap(represented by red/yellow/green

dots).

4.4 Analysis for Solar Absorber Applications

4.4.1 Promising Candidates from the Database

Among double perovskite halide compounds that satisfy the energy above hull criteria defined in the previous section, only 30 compounds satisfy the following conditions: PBE band gaps with $E_g > 0$ (non-metal), $E_{g(direct)} < 1.5$ eV, and effective masses with $0 < m_e, m_h < 1.5$. Such compounds are considered as potentially interesting candidates for photovoltaic applications, and are the focus of further analysis. Specifically, for these 30 compounds, we further relax the structure using the HSE functional and calculate band gaps using the HSE functional with SOC included.

We consider first a comparison of the calculated and measured lattice constant of $Cs_2AgBiBr_6$, $Cs_2AgBiCl_6$ and $Cs_2AgInCl_6$. Note that $Cs_2AgBiBr_6$ and $Cs_2AgBiCl_6$ are experimentally observable but do not belong to the predicted 30 promising candidates. The calculated and measured lattice constants agree reasonably well with the GGA-PBE value(11.49 A, 10.96 A and 10.68 A), which are larger than measurements(11.25 A[83], 10.78 A[86] and 10.47 A[93]) by up to 2.1%. The calculated results from HSE06(10.60 A for $Cs_2AgInCl_6$) show slightly better agreement with measurements, with a deviation of 1.3%. Supplemental Table B.2 lists calculated results for the lattice constants of the 30 $A_2MM'X_6$ compounds that passed the screening criteria described above, and also compares and shows that the present GGA-PBE calculated lattice constants are consistent with previous calculations using the same method.

Band gaps, energies above hull and effective masses of the 30 compounds are listed in supplemental Table B.3 and Table B.4, respectively. For these 30 compounds, except for $Cs_2AgInCl_6$, all other compounds have not been experimentally realized as reported in the Inorganic Crystal Structure Database[53, 54]. Among the 30 compounds, 12 compounds are predicted to be thermodynamically stable ($E_{hull} = 0$), including $Cs_2AgInCl_6$. The HSE06+SOC calculated band gaps span the range of 0.2 to 2.6 eV. We also list in Table B.3 some of the measured band gap and calculated HSE06+SOC band gaps from other work. The present calculated HSE06+SOC band gap for $Cs_2AgInCl_6$(2.57 eV) is very close to a previous HSE06 calculation(2.6 eV)[93] without SOC, indicating that SOC effects are not significant for In/Ag double perovskites. Both calculations give band gap values somewhat smaller than measurements(3.3 eV)[93]. We further compare our HSE+SOC calculations with previous calculations for additional compounds in Table B.3; results are largely consistent with the small differences likely due to the fact that the calculated band gaps are sensitive to the lattice constant and our calculations are based on HSE06 relaxed structures while previous calculations are based on PBE relaxed structures[99].

The 30 compounds are divided into five categories according to their M and M′ site elements. The five categories are listed in Table 4.1. For Category 1 and Category 2 compounds, M and M' cations have the same electron configurations(both $d^{10}s^0$ or both $d^{10}s^2$), which leads to a direct band gap. For all other categories, M and M' cations have mismatched electron configurations, which leads to an indirect band gap. Category 3 and Category 5

Category	M	M'	electron configuration	band gap
1	Cu, Ag, Au	Al, Ga, In ,Tl	$d^{10}s^0/d^{10}s^0$	direct
2	In, Tl	As, Sb, Bi	$d^{10}s^2/d^{10}s^2$	direct
3	Cu, Ag, Au	As, Sb, Bi	$d^{10}s^0/d^{10}s^2$	indirect
4	Cu, Ag, Au	Sc, Y	$d^{10}s^0/p^6$	indirect
5	In, Tl	Al, Ga, In, Tl	$d^{10}s^2/d^{10}s^0$	indirect

Table 4.1: Five categories of promising candidates. Electron configurations and band gap types are listed.

actually have the same mismatched electron configurations($d^{10}s^2/d^{10}s^0$), and it is expected that they have similar electronic structures.

Similar to halide perovskite AMX_3[45] and derivative A_2MX_6[38] compounds, in the chemical series K, Rb and Cs, the band gap slightly increases(for example, $K_2AgInCl_6$(2.49 eV) to $Rb_2AgInCl_6$(2.52 eV) to $Cs_2AgInCl_6$(2.57 eV)); from Cl to Br to I, the band gap decreases more strongly(for example, $Rb_2AgInCl_6$(2.52 eV) to $Rb_2AgInBr_6$(1.44 eV) and $Rb_2TlSbBr_6$(1.03 eV) to Rb_2TlSbI_6(0.57 eV)). The chemical trends for M and M′ site elements are more complex and will be discussed further below.

We consider next the results for effective masses listed in Supplemental Table B.4. Our calculated average effective masses are consistent with previous calculations, even though previous calculations are based on PBE+SOC band structures and our calculations are based on PBE band structures. The chemical trends in effective mass values listed in Table B.4 are correlated with those for the band gaps. Specifically, increasing the size of the A-site cation leads to an increase in both the effective mass and the band gap; increasing the size of the X-site anion leads to a decrease in both the effective mass and the band gap. This correlation between band gap and effective mass is consistent with $k \cdot p$ theory[71]. If we only consider effective mass, among the five categories, the In/Tl-As/Bi/Sb compounds are the best candidates for high mobilities, desirable for photovoltaic applications, since they have small effective mass for both electrons and holes.

4.4.2 Band Structure

In Figure 4.3 we present calculated band structures and densities of states for one representative compound from each of categories listed in Table 4.1. Since Category 3 and 5 have the same electron configurations, only the representative compound from Category 5 is shown.

We consider first the electronic structure of $Cs_2AgInBr_6$(Figure 4.3(a)), representative of the set of compounds with M = Cu, Ag, Au and M′ = Al, Ga, In ,Tl (from Category 1). It is calculated to be a direct band gap semiconductor with valence band derived from antibonding states of Ag-d and Br-p orbitals and conduction band derived from antibonding states of

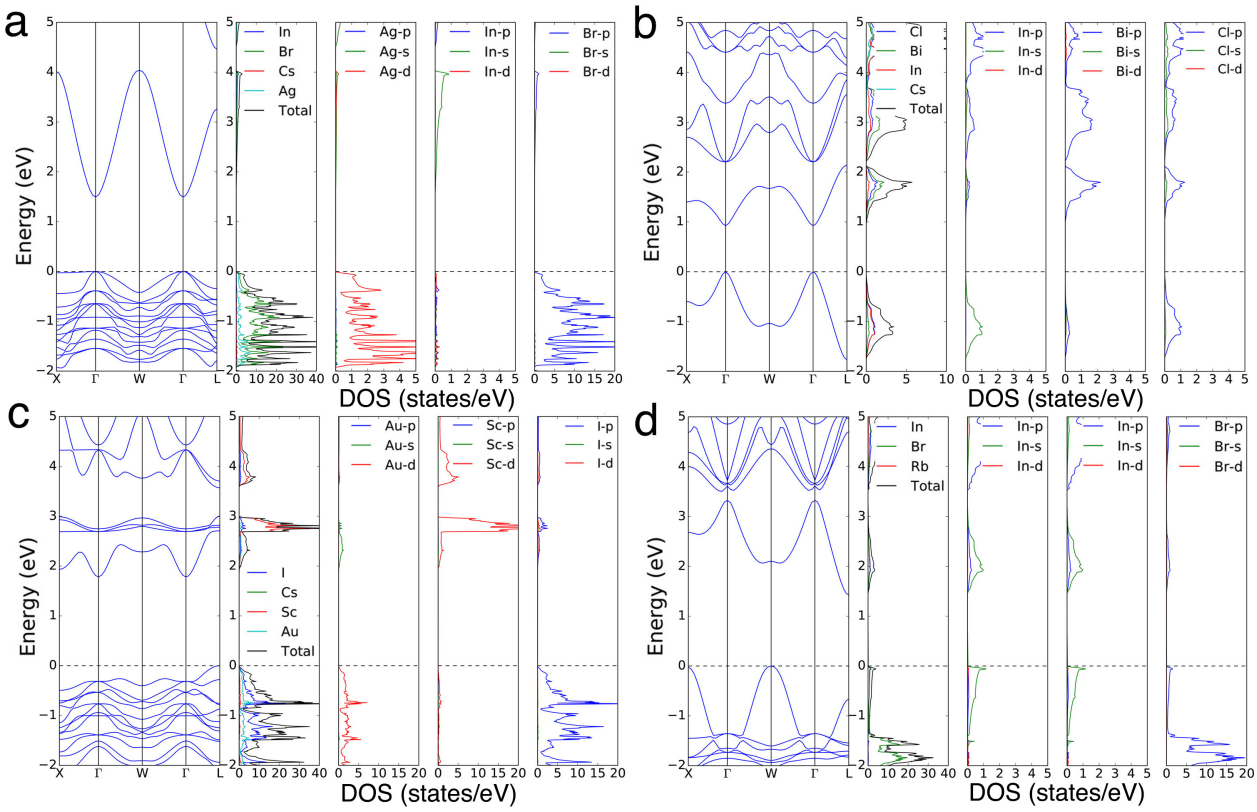

Figure 4.3: Band structures, total and projected densities of states(DOS), calculated by PBE+SOC with conduction bands shifted to match calculated HSE06+SOC band gaps by scissor operator for (a) $Cs_2AgInBr_6$ (Category 1), (b) $Cs_2InBiCl_6$(Category 2), (c) Cs_2AuScI_6(Category 4) and (d) $Rb_2InInBr_6$ (Category 5).

In-s and Br-p orbitals. The direct nature of the band gap of $Cs_2AgInBr_6$ is consistent with previous ab initio calculations[101]. The conduction band is very dispersive(s character), leading to its small electron effective mass($0.18m_e$). The valence band edge consists of a heavy hole band and a light hole band, and the average hole effective mass($0.71m_e$) is thus larger than the electron effective mass.

We consider next the representative compound $Cs_2InBiCl_6$ for the set of compounds with M = In, Tl and M′ = As, Sb, Bi (from Category 2). The calculated band structure in Figure 4.3(b) shows that this compound is a direct band gap semiconductor with valence band derived primarily from antibonding states between In-s and Cl-p orbitals and conduction band primarily from antibonding states between Bi-p and Cl-p orbitals. The direct nature of the band gap of $Cs_2InBiCl_6$ is consistent with previous ab initio calculations[99]. The dispersive nature of both the conduction band and valence band leads to the small electron and hole effective mass($0.39m_e$ and $0.18m_e$). The dispersive valence band derives from the s orbitals of the cations.

Next we consider the compound Cs_2AuScI_6 representative of the set of compounds with M = Cu, Ag, Au and M′ = Sc, Y (from Category 4). The calculated band structure in Figure 4.3(c) shows that it is an indirect gap semiconductor with valence band derived primarily from antibonding states between Au-d and I-p orbitals and conduction band derived from both antibonding states between Au-s and I-p orbitals and antibonding states between Sc-d and I-p orbitals. To the best of our knowledge, no experimental results have been reported for any of the compounds in this category. The conduction band is more dispersive than the valence band, resulting in a smaller electron effective mass($0.23m_e$) than hole effective mass($0.64m_e$).

We consider finally $Rb_2InInBr_6$, representative of the set of compounds with M and M′ from the same group (Al, Ga, In, Tl) in the periodic table (from Category 5). The calculated band structure in Figure 4.3(d) shows that it is an indirect band gap semiconductor with different cation configurations(In-d10s0, In-d10s2). If the two In ions in the primitive unit cell are in the same charge state, with one unpaired s electron, we would expect $RbInBr_3$ to be a metallic conductor. Indeed, forcing a single charge state for In by using a 5-atom unit cell results in a metallic state. Charge ordering between different valence states on the In site leads to the semiconductor state in Figure 4.3(d), with lower energy than the metallic state. Two similar compounds $CsTlCl_3$ and $CsTlF_3$ have been synthesized and found to be insulators[110]. Labeling the In ion with more charge on it(which we identify as corresponding to the formal 1+ oxidation state) to be In1 and the In ion with less charge on it(which we identify as corresponding to the formal 3+ oxidation state) to be In2, then the valence band of $Rb_2InInBr_6$ is derived from antibonding states between In1-s and Br-p orbitals and conduction band derived from antibonding states between In2-s and Cl-p orbitals. This interpretation is better supported by the crystal orbital Hamilton population analysis in Supplemental Figure B.6. Both the valence band and conduction band are very dispersive due to their s character, resulting in very small electron and hole effective masses.

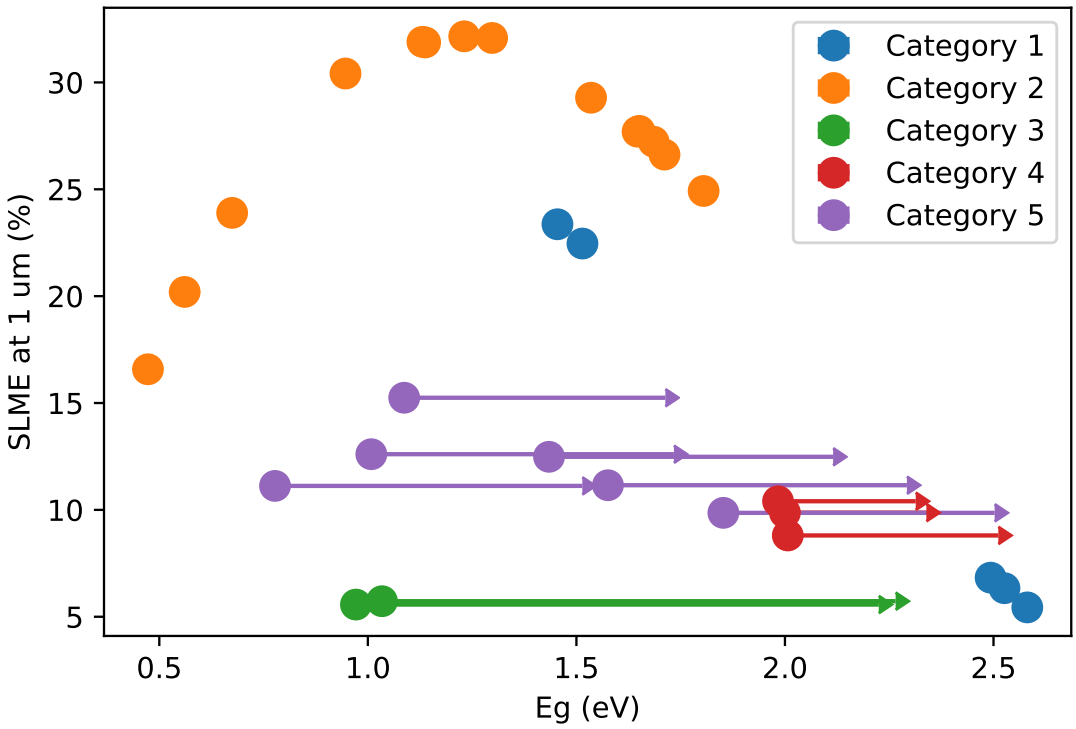

Figure 4.4: SLME at L = 1 μm vs the fundamental gap E_g for compounds from the 5 categories. For categories 3, 4 and 5, the arrow indicates the direct dipole allowed band gap E_g^{da}.

4.4.3 Optical Absorption and Spectroscopic Limited Maximum Efficiency

Absorption properties relevant to photovoltaic applications depend not only on band gap, but also on the nature of the gap, i.e. direct or indirect, dipole allowed or forbidden. The absorption spectra for compounds from the 5 categories are presented in Fig. B.7-B.12. The onsets of all compounds is close to their dipole allowed band gaps E_g^{da}(matrix element squared $|M|^2 > 10^{-6} eV^2/A^2$). For Category 1 and Category 2 compounds, E_g^{da} is the fundamental band gap. For the other three categories with indirect band gaps, E_g^{da} is significantly larger than the fundamental band gap E_g, as shown in Fig. 4.4, where the dots indicate E_g and arrows indicate E_g^{da}. So it is reasonable that we use direct band gap instead of fundamental band gap in the first screening steps.

Based on absorption spectra, we then calculate the spectroscopic limited maximum efficiency(SLME) as defined by Yu and Zunger[112]. SLME takes consideration of band gap, the shape of absorption spectra and nonradiative recombination losses. The fraction of radiative recombination current is an exponential decay function with decay rate determined by E_g^{da}-E_g. Larger E_g^{da}-E_g indicates more severe nonradiative recombination losses. SLMEs for all 30 compounds are plotted versus their band gaps in Fig. 4.4. Category 2 compounds forms a curve very similar to that of the Shockley–Queisser limit. This is not surprising since the assumptions made when calculating the Shockley–Queisser limit are good approximations for Category 2 compounds, where the radiative recombination dominates and the absorption onsets are sharp. For Category 1 compounds, even though they are direct gap semiconductors, their absorption onset is not as sharp as Category 2 compounds, as it takes over 0.5eV for their absorption coefficients to rise up to 10^4 cm^{-1}(Figure. B.7). As discussed by Meng et al, Category 1 compounds exhibit parity-forbidden transitions only between CBM and VBM, but with allowed transitions between band edges at other k points[100]. As a result, the SLMEs for Category 1 compounds are lower than Category 2 compounds at similar band gaps. Category 3 compounds have lowest efficiencies among the 5 categories, due to their large direct band gaps as well as large nonradiative recombination losses caused by large E_g^{da}-E_g. Category 4 compounds have higher efficiencies than Category 3 compounds with similar direct band gaps, probably due to the smaller difference between E_g^{da} and E_g in Category 4 compounds. Category 5 compounds have best efficiency among the indirect gap compounds, because some of Category 5 compounds have band gaps closer to the ideal value. Overall, the direct gap compounds (Category 1 and 2) achieve better SLMEs than the indirect gap compounds, with the best featuring theoretically predicted efficiency higher than 30%.

4.4.4 Dynamical Stability Analysis

As mentioned above, it is possible that at low temperature some of the double perovskite compounds in the high-symmetry $Fm\bar{3}m$ structure may be dynamically unstable with respect to symmetry-lowering phonon modes associated with ferroelectric, octahedral-rotation and related structural distortions. To investigate this issue, for all 30 compounds identified above, dynamical stability is evaluated by calculating phonon spectra at 0K. The least stable phonon frequencies (i.e., the lowest real frequency for dynamically stable compounds, and the imaginary frequency with the largest magnitude for dynamically unstable compounds)

and related q-points are listed in Table B.6. Also listed in Table B.6 is the space group of the distorted structure that results from introduction of the least stable phonon mode; for the correspondence between this space group and the distortion mode the interested is referred to Ref. 109. Two of the compounds($Cs_2AgInCl_6$ and $Cs_2InAsBr_6$) have no imaginary modes and are dynamically stable at 0K. All other compounds have imaginary modes at 0K, mostly at Γ. For 5 of the compounds, the frequencies of the imagniary modes are larger than 10 THz, and we consider them to be dynamically unstable. For all other 23 compounds with smaller imaginary frequencies, it is still possible that the phonon entropy at finite temperatures can stabilize these modes at room temperature. For these compounds, we imposed structural distortions corresponding to the most unstable phonon mode at Γ and performed structural relaxations; the energy differences between the resulting relaxed distorted structures and the ideal cubic structure are listed in Table B.6. If this structural energy difference is smaller than 10 meV/atom, we consider the compounds as candidates for stability in the cubic phase at room temperature. Out of the 25 compounds with small or no imaginary frequencies, 14 meet this criterion: 3 from Category 1, 7 from Category 2, 1 from Category 3 and 3 from Category 5.

Table 4.2: 11 $A_2MM'X_6$ compounds that are both thermodynamically and dynamically stable and have SLMEs larger than 10%. Chemical formula, Category, calculated SLME at $L = 1\mu m$, effective masses, energies above hull (meV/atom) and E_{cubic}-$E_{distorted}$ (meV/atom) are listed below.

Formula	**Category**	**SLME at $1\mu m$ (%)**	$\mathbf{m}_e$	$\mathbf{m}_h$	$\mathbf{E}_{hull}$	$\mathbf{E}_{cubic}$-$\mathbf{E}_{distorted}$
$Cs_2AgInBr_6$	1	22.5	0.18	0.71	0.0	0.0
$Cs_2InAsBr_6$	2	20.2	0.30	0.05	26.2	0.0
$Cs_2InBiCl_6$	2	24.9	0.39	0.18	14.2	8.2
$Cs_2InBiBr_6$	2	31.9	0.32	0.11	0.0	6.8
$Cs_2InSbBr_6$	2	23.9	0.31	0.07	7.0	2.6
$Cs_2TlAsBr_6$	2	27.7	0.31	0.15	0.0	1.6
Cs_2TlAsI_6	2	32.1	0.23	0.13	0.0	3.1
$Cs_2TlSbBr_6$	2	27.7	0.31	0.16	12.4	9.0
Cs_2InGaI_6	5	11.1	0.22	0.51	18.1	1.1
$Cs_2InInBr_6$	5	11.2	0.27	0.58	0.0	2.3
$Cs_2TlTlBr_6$	5	15.2	0.26	0.58	0.7	6.8

Combining with SLMEs calculated above, in Table 4.2 we summarize the 11 compounds

that have SLMEs larger than 10%, are thermodynamically stable and either dynamically stable or possibly dynamically stable at room temperature (based on the energetic criterion above). The d10s2 configuration of the band edges for Category 2 compounds resembles that of hybrid lead halides, so it is not surprising that most of the promising compounds come from Category 2. Of these compounds, those containing In may be more attractive than those containing Tl, due to the toxicity of the latter element.

4.4.5 Chemical Trend Analysis

The efficiencies or stability of a compound can be improved further by substitutional alloying, especially with elements from the same group. A detailed analysis of chemical trends with respect to band structures within the three promising chemical categories defined above may be useful in guiding such band-structure engineering. To analyze the chemical trends of band gaps for the promising categories 1, 2, 5, band gaps are calculated for compounds within each category with the GGA-PBE functional including SOC effect. Specially, band gaps for $Cs_2MM'Cl_6$ compounds with M = Cu, Ag, Au, In, Tl and M′ = Al, Ga, In, Tl, As, Sb, Bi are plotted in Figure 4.5.

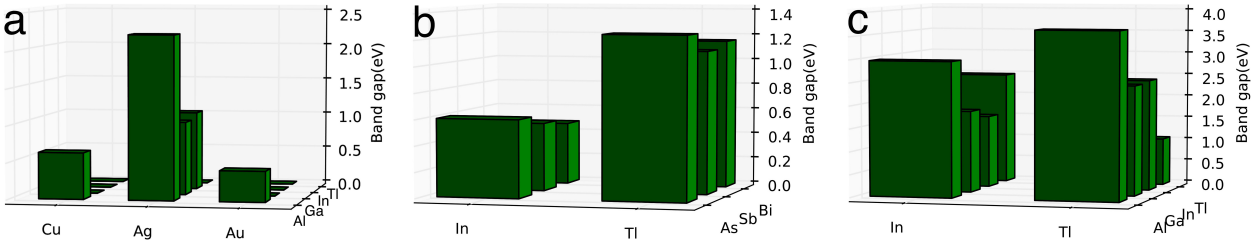

Figure 4.5: Chemical trends of band gaps calculated by PBE+SOC for $Cs_2MM'Cl_6$ with (a) M = Cu, Ag, Au and M′ = Al, Ga, In ,Tl (Category 1) (b) M = In, Tl and M′ = As, Sb, Bi (Category 2) and (c) M = In, Tl and M′ = Al, Ga, In, Tl (Category 5).

For $Cs_2MM'Cl_6$ compounds with M = Cu, Ag, Au and M′ = Al, Ga, In, Tl(Figure 4.5(a), Category 1), Ag-containing compounds have larger band gaps than those with Cu and Au. This can be understood considering that among Cu, Ag and Au, Ag has the lowest energy d states and the valence band maximum(VBM) derives from hybridization between Cu/Ag/Au-d and Cl-p orbitals, such that the lowest VBM for Ag compounds results in the largest band gap. For the M = Ag series, for M' = Ga, In, Tl, the CBM is derived from antibonding M'-s and Cl-p states. The band gap of $Cs_2AgTlCl_6$ is the smallest, due to the relativistic stabilization of Tl-s states and small bonding-antibonding splitting caused by relatively small energetic overlap and spatial overlap of the Tl-Cl bond. For $Cs_2AgAlCl_6$, the Al-s state is shallow and the hybridization of Al-Cl is strong, leading to a high lying Al-Cl antibonding level. In this case, the CBM is no longer Al-Cl states, but Ag-Cl states. The band gap of $Cs_2AgAlCl_6$ is the largest among the M = Ag series.

For $Cs_2MM'Cl_6$ compounds with M = In, Tl and M′ = As, Sb, Bi(Figure 4.5(b), Category 2), Tl compounds have larger band gaps than In compounds. Due to relativistic effects, Tl-s is lower in energy than In-s, resulting in a lower VBM. For M = In series, the band gap difference among As, Sb, Bi is very small, probably because the band edges all have

contributions from In-s and In-p states and the band gaps are affected less by the difference among As, Sb and Bi. For M = Tl series, the band gap difference among As, Sb, Bi is also very small, likely due to the same underlying reason.

For $Cs_2MM'Cl_6$ compounds with M = In, Tl and M′ = Al, Ga, In ,Tl(Figure 4.5(c), Category 5), for the M = Tl series, the CBM is derived from antibonding M'-s and Cl-p character(Tl:1+, M':3+). The band gap of $Cs_2TlAlCl_6$ is the largest, due to the shallow Al-s orbital and large bonding-antibonding splitting caused by the relatively large spatial overlap and energetic overlap of the Al-Cl bond. The band gap of $Cs_2TlTlCl_6$ is the smallest in the series, since the CBM and VBM are derived from the same Tl-s character. For the M = In series, for M' = Tl, In, Ga, the VBM is derived from antibonding M'-s and Cl-p character(M':1+, In:3+). The band gap of $Cs_2TlInCl_6$ is the largest, due to relativistic stabilization of Tl-s orbitals and the small bonding-antibonding splitting caused by relatively small energetic overlap and spatial overlap of the Tl-Cl bond. The band gap of $Cs_2InInCl_6$ is the smallest in the series, since the CBM and VBM are derived from the same In-s character.

4.5 Summary and Discussion

Starting from a consideration of the octahedral and tolerance factors of 1980 candidate double-perovskite compounds, we compute structural, thermodynamic and electronic properties of 1149 compounds using first-principles calculations. The computational results have been assembled in a database that is accessible through the Materials Project online.

We present the application of the database in screening for new double perovskite halide compounds showing promising electronic properties for photovoltaic solar absorber applications. Combining further calculations of optical absorption, conversion efficiency and phonon stability, 11 promising candidates(summarized in Table 4.2) from 3 categories were identified from the database. Seven of these compounds are from a chemical class corresponding to M/M' electronic configurations of $d^{10}s^2/d^{10}s^2$, iso-electronic to the hybrid lead halides. All eleven compounds have not been reported experimentally, and they are listed below with the SLME at $1\mu m$ in the parentheses: $Cs_2AgInBr_6$ (22.5%), $Cs_2InAsBr_6$ (20.2%), $Cs_2InBiCl_6$ (24.9%), $Cs_2InBiBr_6$ (31.9%), $Cs_2InSbBr_6$ (23.9%), $Cs_2TlAsBr_6$ (27.7%), Cs_2TlAsI_6 (32.1%), $Cs_2TlSbBr_6$ (27.7%), Cs_2InGaI_6 (11.1%), $Cs_2InInBr_6$ (11.2%), $Cs_2TlTlBr_6$ (15.2%).

The chemical trends for band gap within each of three different chemical categories are identified as follows: 1) Category 1: for $Cs_2MM'Cl_6$ compounds with M = Cu, Ag, Au and M′ = Al, Ga, In, Tl, silver compounds always have larger band gaps than those with Cu and Au with the same M′ elements; the band gap trend for M′ site is Al > In, Ga > Tl. 2) Category 2: For $Cs_2MM'Cl_6$ compounds with M = In, Tl and M′ = As, Sb, Bi, thallium compounds are found to have larger band gaps than In compounds, confirming results of a previous study[99]. 3) Cateogry 5: For $Cs_2MM'Cl_6$ compounds with M = Tl and M′ = Al, Ga, In, Tl, the band gap trend for M′ site is Al > In, Ga > Tl. For $Cs_2MM'Cl_6$ compounds with M = In and M′ = Ga, In, Tl, the band gap trend for M′ site is Tl > Ga, In. These trends can provide guidelines for the use of substitutional alloying as a means of tuning band structures in halide perovskite solid solutions.

In addition to the potential solar-cell applications discussed specifically above, the halide double-perovskite database developed in this work can be used for other applications such

as scintillators. For scintillator applications, it is usually required that the host materials have large enough band gap to accommodate dopant-ion energy levels involved in relevant electronic transitions. An overview of our database shows that the compounds with alkali metals as M site cations usually have significantly larger band gaps than compounds with other M site elements. Such compounds can be engineered towards scintillator applications, and indeed the compounds Cs_2LiYCl_6 and $Cs_2NaYBr_3I_3$ have already been identified as relevant examples[82, 117]. The calculations for this database yielded a mixed-valence charge-ordered state for $ATlX_3$, consistent with experimental results[110], and also predict a mixed valence state for $AInX_3$ compounds. It is possible that some of these structures or their alloys could be precursors for superconducting compounds, as discussed in Ref. 110. Overall, it is anticipated that the database of halide double-perovskite compounds developed in this work and made available online could find application in materials discovery efforts for a wider variety of applications than those considered here.

4.6 Acknowledgement

This work was funded primarily by the National Research Foundation (NRF), Singapore (CRP NRF2014NRF-CRP002-036 and NRF-CRP14-2014-03) and the Singapore-Berkeley Research Initiative for Sustainable Energy (SinBeRISE) CREATE programme. Use was made of computational resources provided under the Extreme Science and Engineering Discovery Environment (XSEDE), which is supported by the National Science Foundation grant No. OCI-1053575. The efforts of P.H., K.P. and M.A., associated with the integration of the database into Materials Project (P.H. and K.P.) and supervising the computational work and its analysis (M.A.) was funded by the U.S. Department of Energy, Office of Science, Office of Basic Energy Sciences, Materials Sciences and Engineering Division under Contract No. DE-AC02-05-CH11231 (Materials Project program KC23MP).

Chapter 5:

Computational study of $SrNbO_{3+\delta}$

5.1 Introduction

$SrNbO_{3+\delta}$ is a series of related materials with intriguing structures and properties. The compositions can be generalized as the series $Sr_nNb_nO_{3n+2}$. Structurally, the perovskite-derived series $Sr_nNb_nO_{3n+2}$ (n=4, 5, ..., ∞) has extra oxygen planes inserted every n planes along the perovskite [110] direction. $SrNbO_{3.4}$ and $SrNbO_{3.5}$ can be considered members in the perovskite-derived family $Sr_nNb_nO_{3n+2}$ with n = 5 and n = 4, while $SrNbO_3$ can be considered as the end member $n = \infty$. $SrNbO_x$ with $3.4 < x < 3.5$ are usually formed as an intergrowth between $SrNbO_{3.4}$ and $SrNbO_{3.5}$[120].

The tunability of the structure also gives $SrNbO_{3+\delta}$ interesting physical properties. Two of our co-authored papers discussed two relevant but different aspects of the film series $SrNbO_{3+\delta}$. The first paper focuses on photocatalytic properties[118]. $SrNbO_3$, a red metallic oxide, has been shown to act as photocatalyst under visible light to oxidize and reduce water with appropriate sacrificial elements[121]. The room-temperature resistivity of the stoichiometric film was $2.82 \times 10^{-5}\Omega cm$[122]. Questions that naturally arise are 1) Why is $SrNbO_3$ red? 2) as a metal, how can it effectively separate photocarriers? Contrary to previous assumption that the photocatalytic activity comes from interband transition, Wan *et al* points out that it should come from plasmon resonance, arising from the large carrier density in metallic $SrNbO_3$, and the hot electron and hole carriers excited via Landau damping are responsible for the photocatalytic property of $SrNbO_3$ under visible light irradiation[118]. Apart from the conventional plasmon induced by free charge in $SrNbO_3$, the second paper by Asmara *et al* points out that when the density of extra oxygen plane increases(δ increases), correlated plasmons appear, which arise from collective excitations of correlated electrons induced by the strong Coulomb repulsion caused by nanometre-spaced confinement of extra

Part of the results presented in this chapter have been published in two regular articles with title "*Electron Transport and Visible Light Absorption in a Plasmonic Photocatalyst based on Strontium Niobate*" in Nature Communications 8, 15070 (2017) by D. Y. Wan, Y. L. Zhao, Y. Cai, T. C. Asmara, Z. Huang, J. Q. Chen, J. Hong, S. M. Yin, C. T. Nelson, M. R. Motapothula, B. X. Yan, D. Xiang, X. Chi, H. Zheng, W. Chen, R. Xu, Ariando, A. Rusydi, A. M. Minor, M. B. H. Breese, M. Sherburne, M. Asta, Q-H Xu T Venkatesan[118] and title "*Tunable and Low-loss Correlated Plasmons in Mott-like Insulating Oxides*" in Nature Communications 8, 15271 (2017) by Teguh Citra Asmara, Dongyang Wan, Yongliang Zhao, Muhammad Aziz Majidi, Christopher T. Nelson, Mary C. Scott, Yao Cai, Bixing Yan, Daniel Schmidt, Ming Yang, Tao Zhu, Paolo E. Trevisanutto, Mallikarjuna R. Motapothula, Yuan Ping Feng, Mark B. H. Breese, Matthew Sherburne, Mark Asta, Andrew Minor, T. Venkatesan Andrivo Rusydi[119]. Only portions of the above publications that are relevant to the author's contribution are reproduced here. The material is presented here with the permission of co-authors and publishers.

oxygen planes[119].

In what follows we discuss in detail our relevant computational work and contributions to the above two papers and general understanding of the $SrNbO_{3+\delta}$ compound series. Our computational work presents the electronic structure of the film series, and reveals the close relationship between the atomic structures and electronic structures of the films. Before jumping directly into the discussion of the computational work, we first summarize briefly the basic transport properties and micro-structure characterization of the film series.

When growing under low oxygen partial pressure (5×10^{-6} Torr), the film has a carrier density as high as $10^{22} cm^{-3}$ and a moderate electron mobility $2.47 cm^2 V^{-1} s^{-1}$ at room temperature. The structure formed at such low oxygen partial pressure is tetragonal perovskite $SrNbO_3$ in a metallic state. As the oxygen partial pressure increases, the film becomes more and more insulating: both carrier density and carrier mobility decrease. The structure formed at high oxygen pressure(1×10^{-4} Torr) is orthorhombic $SrNbO_{3.5}$ which is insulating. The structure formed at intermediate oxygen pressure is short-range perovskite structure interspersed with extra oxygen defect layers parallel to {101} and {-101} planes. [118, 119] Atomic-resolution high-angle annular dark-field (HAADF) scanning TEM (STEM) images show that the density of the extra oxygen layers increases as the oxygen partial pressure increases. [119]

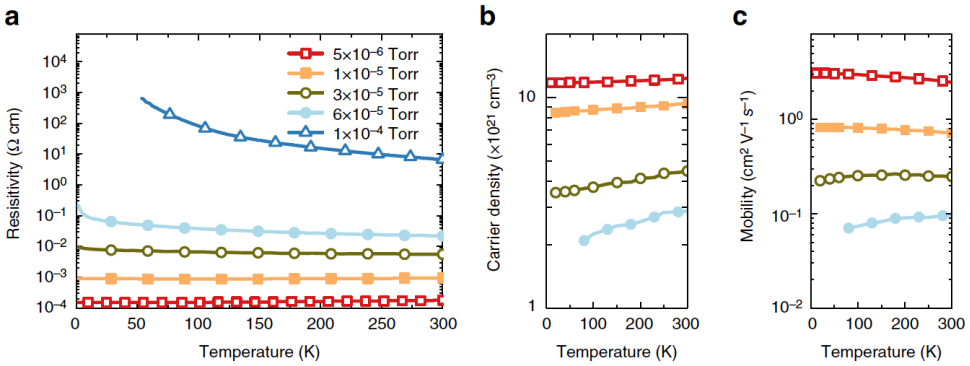

Figure 5.1: Electronic transport properties of $SrNbO_{3+\delta}$ films. Temperature-dependent transport properties of the films prepared at various oxygen pressures: (a) resistivity, (b) carrier density and (c) electron mobility of the films. [118]

5.2 Methods

The atomic and electronic structure of $SrNbO_{3+\delta}$ compounds were performed employing spin-polarized DFT calculations, using the Perdew–Burke–Ernzerhof[28] exchange-correlation potential, and the projector augment wave method[59], as implemented in the Vienna ab-initio simulation program[60–62]. In these calculations, Sr 4s4p5s, Nb 4p5s4d and O 2s2p orbitals were treated as valence states, employing the projector-augment wave potentials labelled Sr_sv, Nb_pv and O in the Vienna ab-initio simulation program Perdew–Burke–Ernzerhof library. The cutoff energy for the plane-wave basis set was set to 450 eV and the DFT+U approach due to Dudarev *et al*[33] was employed to treat the Nb

4d orbitals occupied by the Nb^{4+} ions present for $SrNbO_3$ and $SrNbO_{3.4}$ compositions with the value of U–J set to 4 eV. $SrNbO_3$, $SrNbO_{3.4}$ and $SrNbO_{3.5}$ were modeled by supercells containing, respectively, 20 atoms with space group Pnam, 54 atoms with space group Pnnm and 44 atoms with space group Cmc2. For the cells with oxygen excess (that is, $SrNbO_{3.4}$ and $SrNbO_{3.5}$), the extra oxygen ions were placed in planar defects as illustrated in Fig. 5.4. In the structural relaxations, we employed 8*8*4, 1*4*6 and 1*4*6 k-point meshes, for $SrNbO_3$, $SrNbO_{3.4}$ and $SrNbO_{3.5}$, respectively. The density of states was calculated with 16*16*8, 2*8*12 and 2*8*12 k-point meshes for the same three structures, respectively. In systems with occupied Nb 4d orbitals (that is, $SrNbO_3$ and $SrNbO_{3.4}$), we employed ferromagnetic ordering of the local moments on the Nb^{4+} ions. The Nb valence charge density was calculated using the electron states with energies ranging from the bottom of the Nb conduction band up to the Fermi level.

5.3 Results

5.3.1 Electronic Ground States and Charge Density

In our calculations, the perovskite structure is assumed for the stoichiometric $SrNbO_3$ compound and the extra oxygen atoms for the hyper stoichiometric compositions are assumed to order into planar defects, as illustrated by the structural figures in Fig. 5.2, 5.3 and 5.4. The structural models are consistent with the electron microscopy of the films[119]. For $SrNbO_3$, where Nb is nominally in the 4+ oxidation state, with $4d^1$ electronic configuration, several converged states were obtained in the DFT+U calculations, and the total energies were compared to assess the nature of the electronic ground state. We initially performed calculations for the ferromagnetic spin-polarized and nonmagnetic states, and found that the ferromagnetic state is lower in energy by approximately 0.20 eV per Nb atom. Additionally, we converged the calculations to two different spin-polarized states, and one featuring orbital ordering (Fig. 5.2(a)) was found to have a lower energy than a corresponding non-orbital-ordered state, by approximately 0.17 eV per Nb atom. This result was also confirmed with independent calculations performed using the U-ramping method[37], where the value of U-J was slowly increased from 0 to 4eV, by an increment of 0.1eV. The final state of the system corresponded to a ferromagnetic orbital-ordered state, with the nature of the orbital ordering illustrated in Fig. 5.2(a). In this state the 4d electron on one of the Nb atoms occupies a d_{yz} orbital, and on the other Nb atom the electron occupies a linear combination of d_{xy} and d_{xz} orbitals.

For $SrNbO_{3.4}$, we also investigated the relative energies of different spin, charge and orbital ordered electronic states. The lowest energy configuration found was that for the ferromagnetic state illustrated in Fig. 5.2(b); this state was found to be 0.12 eV per Nb atom lower than a related state with an anti-parallel (ferrimagnetic) spin configuration alternating along the direction normal to the planar oxygen defects. In this low energy state, the 4d electrons spread themselves on the three planes of Nb atoms that are in the middle between two neighboring oxygen defect layers. The Nb planes close to extra oxygen walls are depleted of d valence electrons.

In addition to $SrNbO_3$ and $SrNbO_{3.4}$, we also perform density functional theory (DFT)

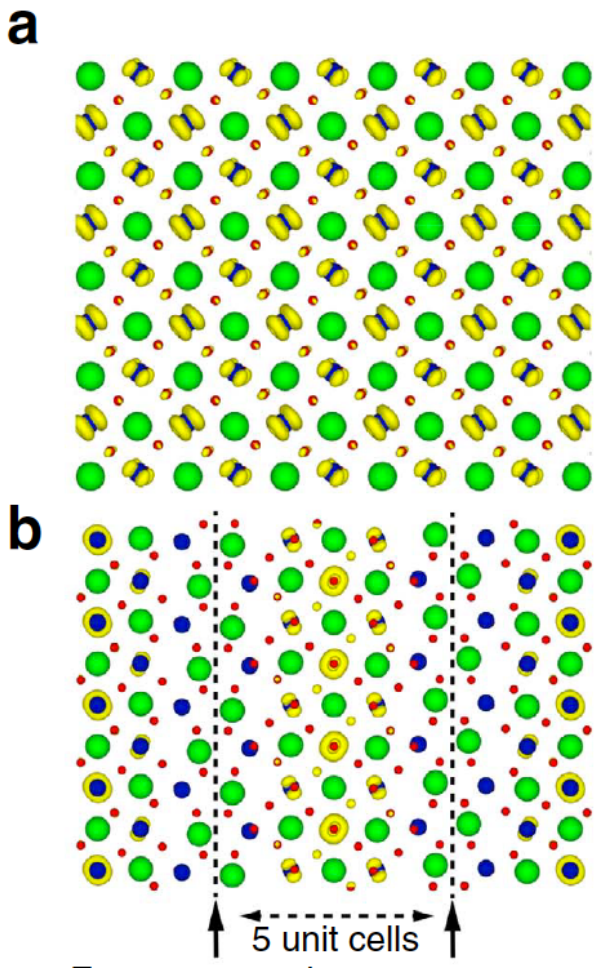

Figure 5.2: (a) Theoretical Nb-4d electron density iso-surface of $SrNbO_3$ superimposed on $SrNbO_3$ crystal structure (Sr:green, Nb:blue, O:red, iso-surface:yellow). (b) Theoretical Nb-4d electron density iso-surface of $SrNbO_{3.4}$ superimposed on $SrNbO_{3.4}$ crystal structure. Black dashed lines denote the oxygen walls. The Nb-4d electrons occupy only the middle three Nb planes, while those close to the oxygen walls are depleted of electrons.

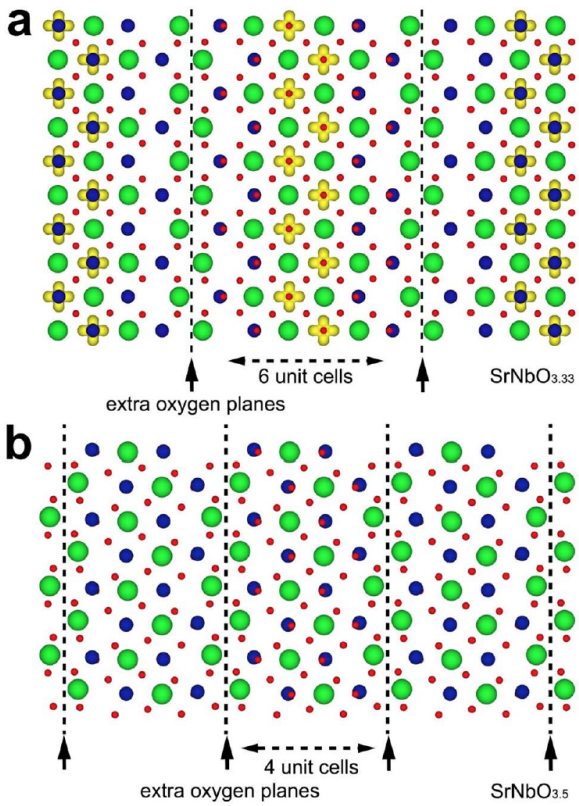

Figure 5.3: Theoretical Nb-4d electron density iso-surface of $SrNbO_{3.33}$ and $SrNbO_{3.5}$. a, Theoretical Nb-4d electron density iso-surface of $SrNbO_{3.33}$ superimposed on $SrNbO_{3.33}$ crystal structure (Sr = green, Nb = blue, O = red, iso-surface = yellow). b, Theoretical Nb-4d electron density iso-surface of $SrNbO_{3.5}$ superimposed on $SrNbO_{3.5}$ crystal structure. Black dashed lines denote the oxygen walls.

calculations on $SrNbO_{3.33}$ and $SrNbO_{3.5}$ (Fig. 5.3(a, b)). From these calculations, the effect of different oxygen concentration in $SrNbO_{3+\delta}$ is to change the spacing (and thus density) of the extra oxygen planes. If the oxygen concentration is decreased to $SrNbO_{3.33}$ (Fig. 5.3(a)), the extra oxygen spacing would increase to 6 unit cells (for $SrNbO_{3.4}$ the spacing is 5 unit cells).

On the other hand, if the oxygen concentration is increased to $SrNbO_{3.5}$ (Fig. 5.3(b)), the extra oxygen spacing would decrease to 4 unit cells. However, this increase of extra oxygens is enough to deplete the free electrons, and as a result $SrNbO_{3.5}$ is found to be an insulator.

5.3.2 Electronic Structures

The energy band structures of $SrNbO_3$, $SrNbO_{3.4}$ and $SrNbO_{3.5}$ are calculated using density functional theory (DFT+U) and shown in Fig. 5.4. As noted above, for $SrNbO_3$ all Nb atoms are nominally in a 4+ ($4d^1$) oxidation state. By contrast for $SrNbO_{3.5}$, all Nb atoms are nominally in the 5+ ($4d^0$) charge state, while for $SrNbO_{3.4}$ the Nb atoms a mixture of oxidation states is expected. Consistent with this picture, the DFT+U (with U-J=4 eV) calculations predicts that the Fermi level of $SrNbO_3$ is in the Nb 4d conduction band, and there is finite density of states at the Fermi level, which implies that this material is metallic even though there is a bandgap as large as 3.0 eV between the CB and the highest fully occupied band (B1 band). The Fermi level of $SrNbO_{3.4}$ is located near the bottom of the conduction band; thus, the conductivity is poorer than that of $SrNbO_3$, as there are fewer states for the free carriers leading to a lower carrier density. These results are consistent with the experimental measurements. $SrNbO_{3.5}$ has a conduction band that has primarily Nb-4d character, and a valence band that is dominantly O-2p in character. Unlike $SrNbO_3$ and $SrNbO_{3.4}$, the Fermi level of $SrNbO_{3.5}$ is located at the top of the valence band; thus, $SrNbO_{3.5}$ is insulating and the film should be transparent, consistent with experiments.

5.3.3 Effect of Sr vacancies

The experimentally synthesized samples are characterized to have 6% Sr vacancies. The main effect of Sr vacancies was assumed to be to shift the Fermi level downward in energy, without changing significantly the shape of the valence and conduction bands. Consequently, we undertook calculations of the Nb valence charge density by integrating the charge density of bands from the bottom of the conduction band to a lower value of the Fermi energy calculated to give the correct number of valence electrons, including the measured level of Sr vacancies. The results are shown in Fig. 5.5. To highlight the charge density difference between the systems with and without Sr vacancies, planar integrated charge densities along the long axis in the $SrNbO_{3.4}$ structure are plotted in Fig. 5.5. The magnitude of the charge density is lowered due to the holes introduced by the Sr vacancies, but the qualitative shape of the spatial variation in the charge density is maintained.

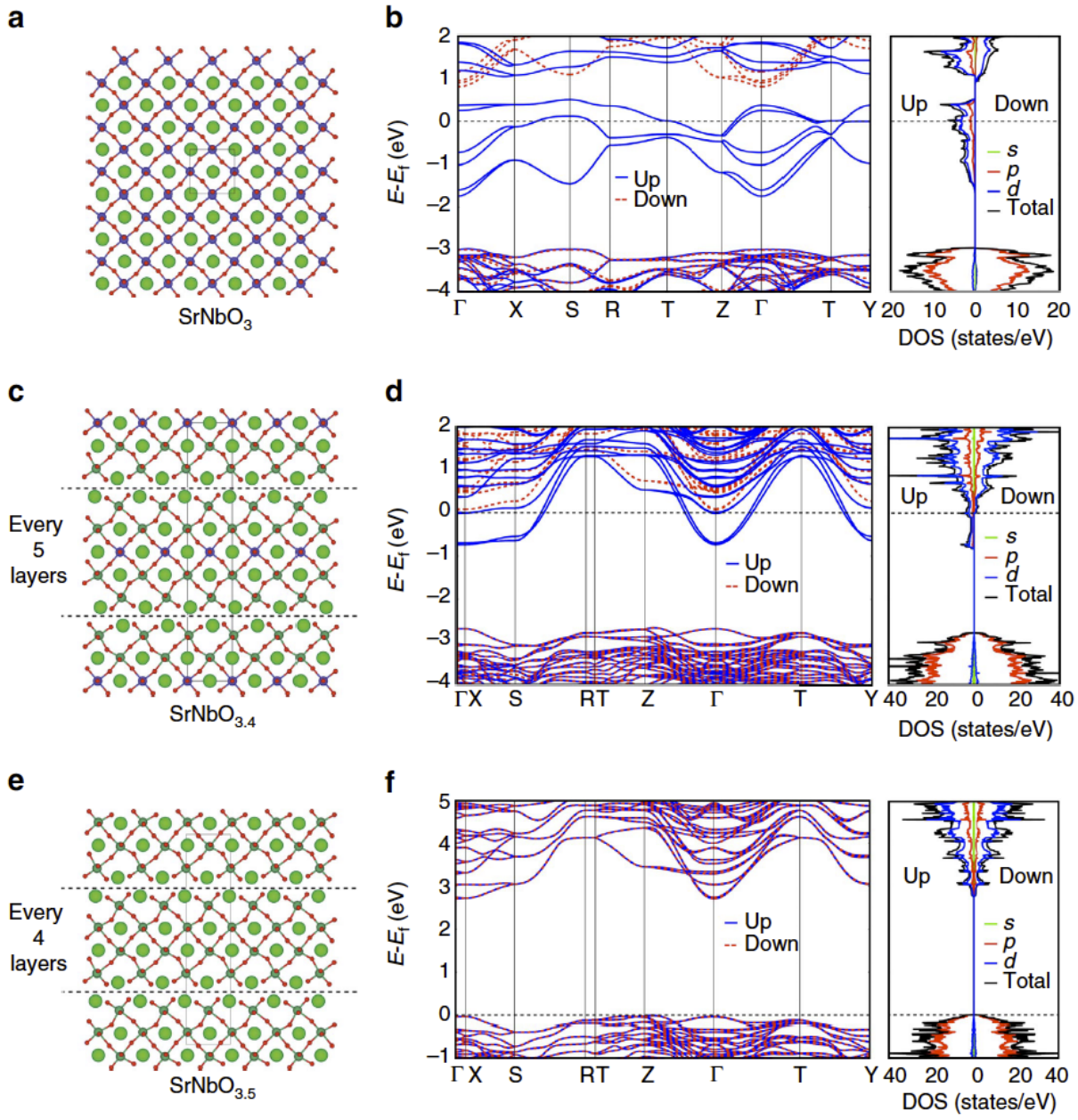

Figure 5.4: Crystal structures and energy band structures with its density of state (DOS) of $SrNbO_{3+\delta}$). (a) Distorted perovskite structure of $SrNbO_3$. O^{2-}: small red sphere, Sr^{2+}: large green sphere, Nb^{4+}: small blue sphere. The unit cell is shown with the black solid line. (b) Band structure and DOS of $SrNbO_3$, showing its metallic behaviour. (c) The layered structure of $SrNbO_{3.4}$ with extra oxygen layers inserted every five octahedral layers. The dash lines indicate where the extra oxygen layers are. Nb^{4+} (small blue sphere) and Nb^{5+} (small green sphere) are given different colors to show charge ordering in this composition. (d) Band structure and DOS of $SrNbO_{3.4}$, with significantly reduced carriers at the Fermi level. (e) The layered structure of $SrNbO_{3.5}$, with an extra oxygen layer inserted every four octahedral layers. (f) Band structure and DOS of $SrNbO_{3.5}$, showing its insulating behaviour. The calculation method is using DFT+U ($U - J = 4eV$).

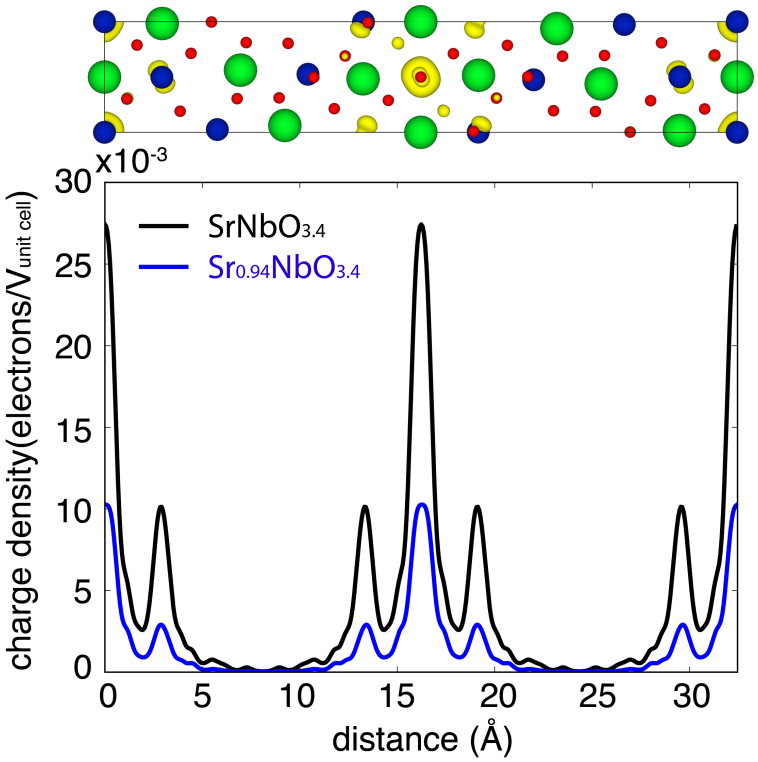

Figure 5.5: Nb valence charge densities of $SrNbO_{3.4}$ and $Sr_{0.94}NbO_{3.4}$. The density curves in the lower panel are the density projections along the long unit cell axis in the upper panel.

5.4 Summary and Discussion

Under low oxygen pressure, films formed have the long-range $SrNbO_3$ perovskite structure. $SrNbO_3$ has a heavily degenerate conduction band and a high carrier density. These characteristics of the electronic structure lead to a strong plasmonic effects. A plasmon peak at 1.8 eV was observed for this film and explaines its red color[118]. These findings contradict earlier report that the visible light absorption is caused by interband transitions[121]. The decaying of these plasmons create hot electrons and holes that are involved in photocatalytic reactions.[118]

When growing under higher oxygen pressure, the carrier density decreases and the films become more insulating. The density of extra oxygen planes increases and in the structure of nominal composition $SrNbO_{3.4}$, they should appear every 5 unit cells. According to our calculation for $SrNbO_{3.4}$, valence electrons are confined in the middle of two neighboring extra oxygen planes. This confinement provided by the extra oxygen planes enhances the Coulomb interactions and induces the correlation between the confined electrons. A new form of correlated plasmons arises from collective excitations of these strongly correlated electrons. [119]

5.5 Acknowledgement

This work was funded by National Research Foundation (NRF), Singapore (CRP NRF2014NRF-CRP002-036) and the Singapore-Berkeley Research Initiative for Sustainable Energy (SinBeRISE) CREATE programme. This work made use of computational resources provided under the Extreme Science and Engineering Discovery Environment (XSEDE), which is supported by the National Science Foundation grant No. OCI-1053575.

Chapter 6:

Summary and Future Work

6.1 Summary of Results

In this dissertation, we investigate the electronic properties of several energy-conversion materials and reveal the relationship between their structure and physical properties through density functional calculations. Below we will summarize the main results of this dissertation.

In Chapter 3, we focus on a perovksite-derived halide A_2BX_6 for photovoltaic applications. The electronic structure and energetic stability of A_2BX_6 halide compounds with the cubic and tetragonal variants of the perovskite-derived K_2PtCl_6 prototype structure are investigated computationally within the frameworks of density-functional-theory and hybrid functionals. The HSE06 calculations are undertaken for seven known A_2BX_6 compounds with A = K, Rb and Cs, and B = Sn, Pd, Pt, Te, and X = I. Trends in band gaps and energetic stability are identified, which are explored further employing DFT calculations over a larger range of chemistries, characterized by A = K, Rb, Cs, B = Si, Ge, Sn, Pb, Ni, Pd, Pt, Se and Te and X = Cl, Br, I. For the systems investigated in this work, the band gap increases from iodide to bromide to chloride. Further, variations in the A site cation influences the band gap as well as the preferred degree of tetragonal distortion. Smaller A site cations such as K and Rb favor tetragonal structural distortions, resulting in a slightly larger band gap. For variations in the B site in the (Ni, Pd, Pt) group and the (Se, Te) group, the band gap increases with increasing cation size. However, no observed chemical trend with respect to cation size for band gap was found for the (Si, Sn, Ge, Pb) group. The findings in this work provide guidelines for the design of halide A_2BX_6 compounds for potential photovoltaic applications.

In Chapter 4, we focus on building a database for the double perovkite halides and employ the database to identify new materials for photovoltaic applications. Starting from a consideration of the octahedral and tolerance factors of $\sim$2000 candidate double-perovskite compounds, we compute structural, electronic and transport properties of $\sim$1000 using first-principles calculations based on density-functional-theory methods. The computational results have been assembled in a database that is accessible through the Materials Project online. As one potential application, double perovskites are candidates in the search for lead-free halide photovoltaic absorbers. We present the application of our database to aid the discovery of new double perovskite halide photovoltaic materials, by combining the results with optical absorption and phonon stability calculations. Eleven compounds from three distinct classes of chemistries were identified as promising solar absorbers and the complex chemical trends for band gap within each of these are analyzed, to provide guidelines for the use of substitutional alloying as a means of further tuning the electronic structure.

In Chapter 5, we focus on the $SrNbO_{3+\delta}$ structures with different oxygen compositions

and discuss their electronic properties based on density functional theory calculations of their electronic structures and charge density distributions. Under low oxygen pressure, films formed have the long-range $SrNbO_3$ perovskite structure. $SrNbO_3$ has a heavily degenerate conduction band and a high carrier density. When growing under higher oxygen pressure, the carrier density decreases and the films become more insulating. The density of extra oxygen planes increases and in the structure of nominal composition $SrNbO_{3.4}$, they should appear every 5 unit cells. According to our calculation for $SrNbO_{3.4}$, valence electrons are confined in the middle of two neighboring extra oxygen planes. These characteristics of the electronic structures lead to a strong conventional plasmonic effects and a strongly correlated plasmonic effects for $SrNbO_3$ and $SrNbO_{3.4}$, respectively.

6.2 Unpublished and Future Work

This section discusses some of the unpublished and future work that can be developed based on the work summarized in this dissertation.

6.2.1 Discover Novel Materials with Double Perovskite Halide Database

The double perovskite halide database can be used not only for screening photovoltaic materials, but for discovering materials with interesting physical properties or screening materials for other applications. Materials that are not suitable for solar cell absorber materials might be good candidates for other applications. For example, the double perovskite halides can also be screened for scintillator applications. Thermodynamic stability, band gaps and effective masses developed in this database are important for a lot of applicatios. For example, for activated scintillators, their band gaps should be small enough for high light yield, but large enough to accommodate the activator ion levels; their effective mass should be small enough for efficient transport and fast scintillation response.

6.2.2 Perovskite Halide Solid Solution

To further optimize perovskite halides for solar cell applications, substitutional alloying is a useful strategy. In current work, we only investigated pure perovskite-derived A_2BX_6 and double perovksite $A_2BB'X_6$. We provide a detailed analysis about the chemical trends in the chemical series, which can be a start point for designing solid solutions with even better properties. For example, substitutional alloying at the X site can be used to tune the band gap; substitutional alloying at the A site can be used to tune the stability of the structure; substitutional alloying at B site is more subtle and can be used to change the characteristic of the band edges. This requires more computations for solid solutions and can be based upon the methodologies developed for this dissertation.

6.2.3 Double Perovskite Defect Calculations

An important aspect that is not discussed in the current dissertation is the defect properties of double perovskite halide. As discussed in Chapter 1, the Shockley Read Hall recombination depends on the density and characteristics of defects. Defects can be modelled

using density functional theory. Defect levels and their positions relative to band edges can be calculated. Point defect formation energies under different growth conditions can also be calculated to get the most dominant point defect species under different growth conditions. Based on the findings in current dissertation, defect properties for outstanding candidates can be further investigated.

Bibliography

[1] "Seia solar industry research data," https://www.seia.org/solar-industry-research-data, accessed: 2019-07-30.

[2] J. Nelson, *The Physics of Solar Cells*, ser. Physics textbook. Imperial College Press, 2003. https://books.google.com/books?id=p_V9ngEACAAJ

[3] S. Rühle, "Tabulated values of the Shockley–Queisser limit for single junction solar cells," *Solar Energy*, vol. 130, pp. 139–147, Jun. 2016. http://www.sciencedirect.com/science/article/pii/S0038092X16001110

[4] W. Shockley and W. T. Read, "Statistics of the Recombinations of Holes and Electrons," *Phys. Rev.*, vol. 87, pp. 835–842, Sep. 1952. https://link.aps.org/doi/10.1103/PhysRev.87.835

[5] D. B. Mitzi, C. A. Feild, W. T. A. Harrison, and A. M. Guloy, "Conducting tin halides with a layered organic-based perovskite structure," *Nature*, vol. 369, p. 467, Jun. 1994. https://www.nature.com/articles/369467a0

[6] A. Kojima, K. Teshima, Y. Shirai, and T. Miyasaka, "Organometal Halide Perovskites as Visible-Light Sensitizers for Photovoltaic Cells," *J. Am. Chem. Soc.*, vol. 131, pp. 6050–6051, May 2009. http://dx.doi.org/10.1021/ja809598r

[7] M. M. Lee, J. Teuscher, T. Miyasaka, T. N. Murakami, and H. J. Snaith, "Efficient Hybrid Solar Cells Based on Meso-Superstructured Organometal Halide Perovskites," *Science*, vol. 338, pp. 643–647, Nov. 2012. http://science.sciencemag.org/content/338/6107/643

[8] J. Burschka, N. Pellet, S.-J. Moon, R. Humphry-Baker, P. Gao, M. K. Nazeeruddin, and M. Grätzel, "Sequential deposition as a route to high-performance perovskite-sensitized solar cells," *Nature*, vol. 499, pp. 316–319, Jul. 2013. https://www.nature.com/articles/nature12340

[9] M. Liu, M. B. Johnston, and H. J. Snaith, "Efficient planar heterojunction perovskite solar cells by vapour deposition," *Nature*, vol. 501, pp. 395–398, Sep. 2013. https://www.nature.com/articles/nature12509

[10] N. J. Jeon, H. Na, E. H. Jung, T.-Y. Yang, Y. G. Lee, G. Kim, H.-W. Shin, S. I. Seok, J. Lee, and J. Seo, "A fluorene-terminated hole-transporting material for highly efficient and stable perovskite solar cells," *Nature Energy*, vol. 3, p. 682, Aug. 2018. https://www.nature.com/articles/s41560-018-0200-6

[11] J. P. C. Baena, L. Steier, W. Tress, M. Saliba, S. Neutzner, T. Matsui, F. Giordano, T. J. Jacobsson, A. R. S. Kandada, S. M. Zakeeruddin, A. Petrozza, A. Abate, M. K. Nazeeruddin, M. Grätzel, and A. Hagfeldt, "Highly efficient planar perovskite solar cells through band alignment engineering," *Energy Environ. Sci.*, vol. 8, pp. 2928–2934, Oct. 2015. https://pubs.rsc.org/en/content/articlelanding/2015/ee/c5ee02608c

[12] A. K. Jena, A. Kulkarni, and T. Miyasaka, "Halide Perovskite Photovoltaics: Background, Status, and Future Prospects," *Chem. Rev.*, vol. 119, pp. 3036–3103, Mar. 2019. https://doi.org/10.1021/acs.chemrev.8b00539

[13] J. Jean, P. R. Brown, R. L. Jaffe, T. Buonassisi, and V. Bulović, "Pathways for solar photovoltaics," *Energy Environ. Sci.*, vol. 8, pp. 1200–1219, Apr. 2015. https://pubs.rsc.org/en/content/articlelanding/2015/ee/c4ee04073b

[14] W.-J. Yin, T. Shi, and Y. Yan, "Superior Photovoltaic Properties of Lead Halide Perovskites: Insights from First-Principles Theory," *J. Phys. Chem. C*, vol. 119, pp. 5253–5264, Mar. 2015. https://doi.org/10.1021/jp512077m

[15] Q. Dong, Y. Fang, Y. Shao, P. Mulligan, J. Qiu, L. Cao, and J. Huang, "Electron-hole diffusion lengths > 175 m in solution-grown CH3nh3pbi3 single crystals," *Science*, vol. 347, pp. 967–970, Feb. 2015. https://science.sciencemag.org/content/347/6225/967

[16] C. Katan, A. D. Mohite, and J. Even, "Entropy in halide perovskites," *Nature Materials*, vol. 17, p. 377, May 2018. https://www.nature.com/articles/s41563-018-0070-0

[17] K. Miyata and X.-Y. Zhu, "Ferroelectric large polarons," *Nature Materials*, vol. 17, p. 379, May 2018. https://www.nature.com/articles/s41563-018-0068-7

[18] S. D. Stranks and P. Plochocka, "The influence of the Rashba effect," *Nature Materials*, vol. 17, p. 381, May 2018. https://www.nature.com/articles/s41563-018-0067-8

[19] K. Frohna, T. Deshpande, J. Harter, W. Peng, B. A. Barker, J. B. Neaton, S. G. Louie, O. M. Bakr, D. Hsieh, and M. Bernardi, "Inversion symmetry and bulk Rashba effect in methylammonium lead iodide perovskite single crystals," *Nat Commun*, vol. 9, pp. 1–9, May 2018. https://www.nature.com/articles/s41467-018-04212-w

[20] A. M. A. Leguy, Y. Hu, M. Campoy-Quiles, M. I. Alonso, O. J. Weber, P. Azarhoosh, M. van Schilfgaarde, M. T. Weller, T. Bein, J. Nelson, P. Docampo, and P. R. F. Barnes, "Reversible Hydration of CH3nh3pbi3 in Films, Single Crystals, and Solar Cells," *Chem. Mater.*, vol. 27, pp. 3397–3407, May 2015. https://doi.org/10.1021/acs.chemmater.5b00660

[21] A. Kudo and Y. Miseki, "Heterogeneous photocatalyst materials for water splitting," *Chemical Society Reviews*, vol. 38, pp. 253–278, 2009. https://pubs.rsc.org/en/content/articlelanding/2009/cs/b800489g

[22] K. Maeda and K. Domen, "Photocatalytic Water Splitting: Recent Progress and Future Challenges," *J. Phys. Chem. Lett.*, vol. 1, pp. 2655–2661, Sep. 2010. https://doi.org/10.1021/jz1007966

[23] P. Hohenberg and W. Kohn, "Inhomogeneous Electron Gas," *Phys. Rev.*, vol. 136, pp. B864–B871, Nov. 1964. https://link.aps.org/doi/10.1103/PhysRev.136.B864

[24] M. Born and K. Huang, *Dynamical Theory of Crystal Lattices*. Oxford University Press, 1954.

[25] W. Kohn and L. J. Sham, "Self-Consistent Equations Including Exchange and Correlation Effects," *Phys. Rev.*, vol. 140, pp. A1133–A1138, Nov. 1965. https://link.aps.org/doi/10.1103/PhysRev.140.A1133

[26] R. M. Martin, *Electronic structure: basic theory and practical methods*. Cambridge university press, 2004.

[27] J. P. Perdew, P. Ziesche, and H. Eschrig, "Electronic structure of solids' 91," 1991.

[28] J. P. Perdew, K. Burke, and M. Ernzerhof, "Generalized gradient approximation made simple," *Phys. Rev. Lett.*, vol. 77, pp. 3865–3868, Oct 1996. http://link.aps.org/doi/10.1103/PhysRevLett.77.3865

[29] G. Pacchioni, "Modeling doped and defective oxides in catalysis with density functional theory methods: Room for improvements," *J. Chem. Phys.*, vol. 128, p. 182505, May 2008. https://aip.scitation.org/doi/10.1063/1.2819245

[30] J. Heyd, G. E. Scuseria, and M. Ernzerhof, "Hybrid Functionals Based on a Screened Coulomb Potential," *The J. Chem. Phys.*, vol. 118, pp. 8207–8215, Apr. 2003. http://aip.scitation.org/doi/10.1063/1.1564060

[31] J. Heyd, J. E. Peralta, G. E. Scuseria, and R. L. Martin, "Energy Band Gaps and Lattice Parameters Evaluated with the Heyd-Scuseria-Ernzerhof Screened Hybrid Functional," *The J. Chem. Phys.*, vol. 123, pp. 174 101–174 108, Oct. 2005. http://aip.scitation.org/doi/10.1063/1.2085170

[32] J. Heyd, G. E. Scuseria, and M. Ernzerhof, "Erratum: "Hybrid Functionals Based on a Screened Coulomb Potential" [J. Chem. Phys. 118, 8207 (2003)]," *The J. Chem. Phys.*, vol. 124, pp. 219 906–219 907, Jun. 2006. http://aip.scitation.org/doi/full/10.1063/1.2204597

[33] S. L. Dudarev, G. A. Botton, S. Y. Savrasov, C. J. Humphreys, and A. P. Sutton, "Electron-energy-loss spectra and the structural stability of nickel oxide: An LSDA+U study," *Phys. Rev. B*, vol. 57, pp. 1505–1509, Jan. 1998. https://link.aps.org/doi/10.1103/PhysRevB.57.1505

[34] V. I. Anisimov and O. Gunnarsson, "Density-functional calculation of effective Coulomb interactions in metals," *Phys. Rev. B*, vol. 43, pp. 7570–7574, Apr. 1991. https://link.aps.org/doi/10.1103/PhysRevB.43.7570

[35] M. Cococcioni and S. de Gironcoli, "Linear response approach to the calculation of the effective interaction parameters in the $\mathrm{LDA}+\mathrm{U}$ method," *Phys. Rev. B*, vol. 71, p. 035105, Jan. 2005. https://link.aps.org/doi/10.1103/PhysRevB.71.035105

[36] L. Wang, T. Maxisch, and G. Ceder, "Oxidation energies of transition metal oxides within the $\mathrm{GGA}+\mathrm{U}$ framework," *Phys. Rev. B*, vol. 73, p. 195107, May 2006. https://link.aps.org/doi/10.1103/PhysRevB.73.195107

[37] B. Meredig, A. Thompson, H. A. Hansen, C. Wolverton, and A. van de Walle, "Method for locating low-energy solutions within $\text{DFT}+U$," *Phys. Rev. B*, vol. 82, p. 195128, Nov. 2010. https://link.aps.org/doi/10.1103/PhysRevB.82.195128

[38] Y. Cai, W. Xie, H. Ding, Y. Chen, K. Thirumal, L. H. Wong, N. Mathews, S. G. Mhaisalkar, M. Sherburne, and M. Asta, "Computational Study of Halide Perovskite-Derived A_2BX_6 Inorganic Compounds: Chemical Trends in Electronic Structure and Structural Stability," *Chem. Mater.*, vol. 29, pp. 7740–7749, Sep. 2017. http://dx.doi.org/10.1021/acs.chemmater.7b02013

[39] H.-S. Kim, C.-R. Lee, J.-H. Im, K.-B. Lee, T. Moehl, A. Marchioro, S.-J. Moon, R. Humphry-Baker, J.-H. Yum, J. E. Moser, M. Grätzel, and N.-G. Park, "Lead Iodide Perovskite Sensitized All-Solid-State Submicron Thin Film Mesoscopic Solar Cell with Efficiency Exceeding 9%," *Scientific Reports*, vol. 2, p. 591, Aug. 2012. https://www.nature.com/articles/srep00591

[40] "Nrel research cell record efficiency chart. https://www.nrel.gov/pv/assets/images/efficiency-chart.png (accessed apr 14, 2017)."

[41] X. Zhao and N.-G. Park, "Stability Issues on Perovskite Solar Cells," *Photonics*, vol. 2, pp. 1139–1151, Dec. 2015.

[42] N. K. Noel, S. D. Stranks, A. Abate, C. Wehrenfennig, S. Guarnera, A.-A. Haghighirad, A. Sadhanala, G. E. Eperon, S. K. Pathak, M. B. Johnston, A. Petrozza, L. M. Herz, and H. J. Snaith, "Lead-free organic-inorganic tin halide perovskites for photovoltaic applications," *Energy Environ. Sci.*, vol. 7, pp. 3061–3068, 2014. http://dx.doi.org/10.1039/C4EE01076K

[43] F. Hao, C. C. Stoumpos, D. H. Cao, R. P. H. Chang, and M. G. Kanatzidis, "Lead-free Solid-state Organic-inorganic Halide Perovskite Solar Cells," *Nat. Photonics*, vol. 8, pp. 489–494, May 2014.

[44] S. Chakraborty, W. Xie, N. Mathews, M. Sherburne, R. Ahuja, M. Asta, and S. G. Mhaisalkar, "Rational Design: A High-Throughput Computational Screening and Experimental Validation Methodology for Lead-Free and Emergent Hybrid Perovskites," *ACS Energy Letters*, vol. 2, pp. 837–845, Apr. 2017. http://dx.doi.org/10.1021/acsenergylett.7b00035

[45] T. Krishnamoorthy, H. Ding, C. Yan, W. L. Leong, T. Baikie, Z. Zhang, M. Sherburne, S. Li, M. Asta, N. Mathews, and S. G. Mhaisalkar, "Lead-free Germanium Iodide Perovskite Materials for Photovoltaic Applications," *J. Mater. Chem.A*, vol. 3, pp. 23 829–23 832, Nov. 2015. http://pubs.rsc.org/en/content/articlelanding/2015/ta/c5ta05741h

[46] B. Lee, C. C. Stoumpos, N. Zhou, F. Hao, C. Malliakas, C.-Y. Yeh, T. J. Marks, M. G. Kanatzidis, and R. P. H. Chang, "Air-Stable Molecular Semiconducting Iodosalts for Solar Cell Applications: Cs_2SnI_6 as a Hole Conductor," *J. Am. Chem. Soc.*, vol. 136, pp. 15 379–15 385, Oct. 2014.

[47] B. Saparov, J.-P. Sun, W. Meng, Z. Xiao, H.-S. Duan, O. Gunawan, D. Shin, I. G. Hill, Y. Yan, and D. B. Mitzi, "Thin-Film Deposition and Characterization of a Sn-Deficient Perovskite Derivative Cs_2SnI_6," *Chem. Mater.*, vol. 28, pp. 2315–2322, Apr. 2016. http://dx.doi.org/10.1021/acs.chemmater.6b00433

[48] A. Kaltzoglou, M. Antoniadou, A. G. Kontos, C. C. Stoumpos, D. Perganti, E. Siranidi, V. Raptis, K. Trohidou, V. Psycharis, M. G. Kanatzidis, and P. Falaras, "Optical-Vibrational Properties of the Cs_2SnX_6 (X = Cl, Br, I) Defect Perovskites and Hole-Transport Efficiency in Dye-Sensitized Solar Cells," *The J. Phys. Chem. C*, vol. 120, pp. 11 777–11 785, Jun. 2016. http://dx.doi.org/10.1021/acs.jpcc.6b02175

[49] Z. Xiao, H. Lei, X. Zhang, Y. Zhou, H. Hosono, and T. Kamiya, "Ligand-Hole in [SnI6] Unit and Origin of Band Gap in Photovoltaic Perovskite Variant cs_2sni_6," *Bull. Chem. Soc. Jpn.*, vol. 88, pp. 1250–1255, 2015. http://www.readcube.com/articles/10.1246/bcsj.20150110

[50] X. Qiu, B. Cao, S. Yuan, X. Chen, Z. Qiu, Y. Jiang, Q. Ye, H. Wang, H. Zeng, J. Liu, and M. G. Kanatzidis, "From Unstable $CsSnI_3$ to Air-stable Cs_2SnI_6: A Lead-free Perovskite Solar Cell Light Absorber with Bandgap of 1.48 eV and High Absorption Coefficient," *Sol. Energy Mater. Sol. Cells*, vol. 159, pp. 227–234, Jan. 2017. https://www.sciencedirect.com/science/article/pii/S0927024816303622

[51] M. G. Brik and I. V. Kityk, "Modeling of Lattice Constant and their Relations with Ionic Radii and Electronegativity of Constituting Ions of A_2XY_6 Cubic Crystals (A=K, Cs, Rb, Tl; X=Tetravalent Cation, Y=F, Cl, Br, I)," *J. Phys. Chem. Solids*, vol. 72, pp. 1256–1260, Nov. 2011. https://www.sciencedirect.com/science/article/pii/S0022369711002137

[52] A. E. Maughan, A. M. Ganose, M. M. Bordelon, E. M. Miller, D. O. Scanlon, and J. R. Neilson, "Defect Tolerance to Intolerance in the Vacancy-Ordered Double Perovskite Semiconductors Cs_2SnI_6 and Cs_2TeI_6," *J. Am. Chem. Soc.*, vol. 138, pp. 8453–8464, Jul. 2016. http://dx.doi.org/10.1021/jacs.6b03207

[53] A. Belsky, M. Hellenbrandt, V. L. Karen, and P. Luksch, "New Developments in the Inorganic Crystal Structure Database (ICSD): Accessibility in Support of Materials

Research and Design," *Acta Crystallogr., Sect. B: Struct. Sci*, vol. 58, pp. 364–369, Jun. 2002. http://scripts.iucr.org/cgi-bin/paper?an0615

[54] G. Bergerhoff, R. Hundt, R. Sievers, and I. D. Brown, "The Inorganic Crystal Structure Data Base," *J. Chem. Inf. Comput. Sci.*, vol. 23, pp. 66–69, May 1983. http://dx.doi.org/10.1021/ci00038a003

[55] A. Jain, S. P. Ong, G. Hautier, W. Chen, W. D. Richards, S. Dacek, S. Cholia, D. Gunter, D. Skinner, G. Ceder, and K. Persson, "The Materials Project: A Materials Genome Approach to Accelerating Materials Innovation," *APL Mater.*, vol. 1, pp. 011 002–011 012, 2013. http://link.aip.org/link/AMPADS/v1/i1/p011002/s1&Agg=doi

[56] R. D. Shannon, "Revised Effective Ionic Radii and Systematic Studies of Interatomic Distances in Halides and Chalcogenides," *Acta Crystallogr. Section A: Crystal Physics, Diffraction, Theoretical and General Crystallography*, vol. 32, pp. 751–767, Sep. 1976. http://scripts.iucr.org/cgi-bin/paper?a12967

[57] W. Li, E. Ionescu, R. Riedel, and A. Gurlo, "Can We Predict the Formability of Perovskite Oxynitrides from Tolerance and Octahedral Factors?" *J. Mater. Chem.A*, vol. 1, pp. 12 239–12 245, 2013. http://pubs.rsc.org/en/Content/ArticleLanding/2013/TA/C3TA10216E

[58] I. D. Brown, "The Crystal Structure of K_2TeBr_6," *Can. J. Chem.*, vol. 42, pp. 2758–2767, Dec. 1964. http://www.nrcresearchpress.com/doi/abs/10.1139/v64-409

[59] P. E. Blöchl, "Projector augmented-wave method," *Phys. Rev. B*, vol. 50, pp. 17 953–17 979, Dec 1994. http://link.aps.org/doi/10.1103/PhysRevB.50.17953

[60] G. Kresse and J. Furthmüller, "Efficient iterative schemes for *ab initio* total-energy calculations using a plane-wave basis set," *Phys. Rev. B*, vol. 54, pp. 11 169–11 186, Oct 1996. http://link.aps.org/doi/10.1103/PhysRevB.54.11169

[61] G. Kresse and J. Furthmüller, "Efficiency of Ab-initio Total Energy Calculations for Metals and Semiconductors Using a Plane-wave Basis Set," *Computational Mater. Sci.*, vol. 6, pp. 15–50, Jul. 1996. http://www.sciencedirect.com/science/article/pii/0927025696000080

[62] G. Kresse and J. Hafner, "*Ab initio* molecular dynamics for liquid metals," *Phys. Rev. B*, vol. 47, pp. 558–561, Jan 1993. http://link.aps.org/doi/10.1103/PhysRevB.47.558

[63] G. Hautier, A. Miglio, G. Ceder, G.-M. Rignanese, and X. Gonze, "Identification and Design Principles of Low Hole Effective Mass p-type Transparent Conducting Oxides," *Nat. Commun.*, vol. 4, pp. 2292–2298, 2013.

[64] G. K. H. Madsen and D. J. Singh, "BoltzTraP. A Code for Calculating Band-structure Dependent Quantities," *Comput. Phys. Commun.*, vol. 175, pp. 67–71, Jul. 2006.

[65] S. P. Ong, W. D. Richards, A. Jain, G. Hautier, M. Kocher, S. Cholia, D. Gunter, V. L. Chevrier, K. A. Persson, and G. Ceder, "Python Materials Genomics (pymatgen): A Robust, Open-source Python Library for Materials Analysis," *Computational Mater. Sci.*, vol. 68, pp. 314–319, Feb. 2013. https://www.sciencedirect.com/science/article/pii/S0927025612006295

[66] W. Werker, "Die Kristallstruktur des Rb_2SnI_6 und Cs_2SnI_6," *Recl. Trav. Chim. Pays-Bas et de la Belgique*, vol. 58, pp. 257–258, 1939.

[67] B. Schüpp, P. Heines, A. Savin, and H.-L. Keller, "Crystal Structures and Pressure-Induced Redox Reaction of $Cs_2PdI_4{\cdot}I_2$ to Cs_2PdI_6," *Inorg. Chem.*, vol. 39, pp. 732–735, Feb. 2000. http://dx.doi.org/10.1021/ic990670+

[68] G. Thiele, "On Hexaiodoplatinates(IV) M_2PtI_6(M = K, Rb, Cs, NH_4, TI) - Preparation, Properties and Structural Data ," *Z. Naturforsch*, vol. 38, pp. 905–910, 1983.

[69] E. Y. Peresh, O. V. Zubaka, V. I. Sidei, I. E. Barchii, S. V. Kun, and A. V. Kun, "Preparation, Stability Regions, and Properties of M_2TeI_6 (M = Rb, Cs, Tl) Crystals," *Inorg. Mater.*, vol. 38, pp. 859–863, Aug. 2002. http://link.springer.com/article/10.1023/A:1019747432003

[70] L.-Y. Huang and W. R. L. Lambrecht, "Electronic Band Structure, Phonons, and Exciton Binding Energies of Halide Perovskites $CsSnCl_3$, $CsSnBr_3$, and $CsSnI_3$," *Phys. Rev. B*, vol. 88, pp. 165 203–165 216, Oct. 2013. http://link.aps.org/doi/10.1103/PhysRevB.88.165203

[71] P. Y. Yu and M. Cardona, *Fundamentals of Semiconductors*, 4th ed. Springer-Verlag Berlin Heidelberg, 2010.

[72] A. W. Laubengayer, O. B. Billings, and A. E. Newkirk, "Chlorogermanic Acid and the Chlorogermanates. Properties and Crystal Structure of Cesium Hexachlorogermanate," *J. Am. Chem. Soc.*, vol. 62, pp. 546–548, Mar. 1940. http://dx.doi.org/10.1021/ja01860a027

[73] G. Engel, "Die Kristallstrukturen einiger Hexachlorokomplexsalze," *Zeitschrift für Kristallographie - Crystalline Materials*, vol. 90, pp. 341–373, 2015. https://www.degruyter.com/view/j/zkri.1935.90.issue-1-6/zkri.1935.90.1.341/zkri.1935.90.1.341.xml

[74] W. Abriel and M. A. White, "The Phase Transitions of Ferroelastic K_2SeBr_6: A Calorimetric and X-ray Diffraction Study," *The J. Chem. Phys.*, vol. 93, pp. 8321–8327, Dec. 1990. http://aip.scitation.org/doi/abs/10.1063/1.459315

[75] W. Abriel, "Crystal Structure and Phase Transition of Rb_2TeI_6," *Mater. Res. Bull.*, vol. 17, pp. 1341–1346, Oct. 1982. http://www.sciencedirect.com/science/article/pii/0025540882901714

[76] S. Syoyama, K. Osaki, and S. Kusanagi, "X-ray Study of the Crystal Structure of K_2TeI_6 and the Symmetry of the Compounds of this Series," *Inorganic and Nuclear Chem. Lett.*, vol. 8, pp. 181–184, Feb. 1972. http://www.sciencedirect.com/science/article/pii/0020165072801077

[77] D. P. McMeekin, G. Sadoughi, W. Rehman, G. E. Eperon, M. Saliba, M. T. Hörantner, A. Haghighirad, N. Sakai, L. Korte, B. Rech, M. B. Johnston, L. M. Herz, and H. J. Snaith, "A mixed-cation lead mixed-halide perovskite absorber for tandem solar cells," *Science*, vol. 351, pp. 151–155, 2016. http://science.sciencemag.org/content/351/6269/151

[78] Y. Cai, W. Xie, Y. T. Teng, P. C. Harikesh, B. Ghosh, P. Huck, K. A. Persson, N. Mathews, S. G. Mhaisalkar, M. Sherburne, and M. Asta, "High-throughput Computational Study of Halide Double Perovskite Inorganic Compounds," *Chem. Mater.*, vol. 31, pp. 5392–5401, Aug. 2019. https://doi.org/10.1021/acs.chemmater.9b00116

[79] E. Greul, M. L. Petrus, A. Binek, P. Docampo, and T. Bein, "Highly stable, phase pure $Cs_2agbibr_6$ double perovskite thin films for optoelectronic applications," *J. Mater. Chem. A*, vol. 5, pp. 19 972–19 981, Sep. 2017. http://pubs.rsc.org/en/content/articlelanding/2017/ta/c7ta06816f

[80] J. Luo, S. Li, H. Wu, Y. Zhou, Y. Li, J. Liu, J. Li, K. Li, F. Yi, G. Niu, and J. Tang, "$Cs_2agincl_6$ Double Perovskite Single Crystals: Parity Forbidden Transitions and Their Application For Sensitive and Fast UV Photodetectors," *ACS Photonics*, vol. 5, p. 398–405, Oct. 2018. https://doi.org/10.1021/acsphotonics.7b00837

[81] W. Pan, H. Wu, J. Luo, Z. Deng, C. Ge, C. Chen, X. Jiang, W.-J. Yin, G. Niu, L. Zhu, L. Yin, Y. Zhou, Q. Xie, X. Ke, M. Sui, and J. Tang, "$Cs_2AgBiBr_6$ single-crystal X-ray detectors with a low detection limit," *Nat. Photonics*, vol. 11, pp. 726–732, Nov. 2017. https://www.nature.com/articles/s41566-017-0012-4

[82] J. Glodo, R. Hawrami, and K. S. Shah, "Development of Cs_2liycl_6 scintillator," *J. Cryst. Growth*, vol. 379, pp. 73–78, Sep. 2013. http://www.sciencedirect.com/science/article/pii/S0022024813002108

[83] A. H. Slavney, T. Hu, A. M. Lindenberg, and H. I. Karunadasa, "A Bismuth-Halide Double Perovskite with Long Carrier Recombination Lifetime for Photovoltaic Applications," *J. Am. Chem. Soc.*, vol. 138, pp. 2138–2141, Feb. 2016. http://dx.doi.org/10.1021/jacs.5b13294

[84] W. Ning, F. Wang, B. Wu, J. Lu, Z. Yan, X. Liu, Y. Tao, J.-M. Liu, W. Huang, M. Fahlman, L. Hultman, T. C. Sum, and F. Gao, "Long Electron–Hole Diffusion Length in High-Quality Lead-Free Double Perovskite Films," *Adv. Mater.*, vol. 30, pp. 1 706 246(1)–1 706 246(6), 2018. https://onlinelibrary.wiley.com/doi/abs/10.1002/adma.201706246

[85] F. Wei, Z. Deng, S. Sun, F. Zhang, D. M. Evans, G. Kieslich, S. Tominaka, M. A. Carpenter, J. Zhang, P. D. Bristowe, and A. K. Cheetham, "Synthesis and Properties of a Lead-Free Hybrid Double Perovskite: $(CH_3NH_3)_2AgBiBr_6$," *Chem. Mat.*, vol. 29, pp. 1089–1094, Jan. 2017. http://pubs.acs.org/doi/abs/10.1021/acs.chemmater.6b03944

[86] G. Volonakis, M. R. Filip, A. A. Haghighirad, N. Sakai, B. Wenger, H. J. Snaith, and F. Giustino, "Lead-Free Halide Double Perovskites via Heterovalent Substitution of Noble Metals," *arXiv:1603.01585 [cond-mat]*, Mar. 2016, arXiv: 1603.01585. http://arxiv.org/abs/1603.01585

[87] E. T. McClure, M. R. Ball, W. Windl, and P. M. Woodward, "Cs 2AgBiX 6(X = Br, Cl): New Visible Light Absorbing, Lead-Free Halide Perovskite Semiconductors," *Chem. Mater.*, vol. 28, pp. 1348–1354, Mar. 2016.

[88] S. E. Creutz, E. N. Crites, M. C. De Siena, and D. R. Gamelin, "Colloidal Nanocrystals of Lead-Free Double-Perovskite (Elpasolite) Semiconductors: Synthesis and Anion Exchange To Access New Materials," *Nano Lett.*, vol. 18, p. 1118–1123, Jan. 2018. https://doi.org/10.1021/acs.nanolett.7b04659

[89] T. ThaoTran, J. R.Panella, J. R.Chamorro, J. R.Morey, and T. M.McQueen, "Designing indirect–direct bandgap transitions in double perovskites," *Mater. Horizons*, vol. 4, pp. 688–693, 2017. http://pubs.rsc.org/en/Content/ArticleLanding/2017/MH/C7MH00239D

[90] F. Wei, Z. Deng, S. Sun, F. Xie, G. Kieslich, D. M. Evans, M. A. Carpenter, P. D. Bristowe, and A. K. Cheetham, "The synthesis, structure and electronic properties of a lead-free hybrid inorganic–organic double perovskite $(MA)_2KBiCl_6$ (MA = methylammonium)," *Mater. Horiz.*, vol. 3, pp. 328–332, Jun. 2016. http://pubs.rsc.org/en/content/articlelanding/2016/mh/c6mh00053c

[91] C. N. Savory, A. Walsh, and D. O. Scanlon, "Can Pb-Free Halide Double Perovskites Support High-Efficiency Solar Cells?" *ACS Energy Letters*, vol. 1, pp. 949–955, Nov. 2016. http://www.ncbi.nlm.nih.gov/pmc/articles/PMC5210270/

[92] Z. Deng, F. Wei, S. Sun, G. Kieslich, A. K.Cheetham, and P. D.Bristowe, "Exploring the properties of lead-free hybrid double perovskites using a combined computational-experimental approach," *J. Mater. Chem. A*, vol. 4, pp. 12 025–12 029, 2016. http://pubs.rsc.org/en/Content/ArticleLanding/2016/TA/C6TA05817E

[93] G. Volonakis, A. A. Haghighirad, R. L. Milot, W. H. Sio, M. R. Filip, B. Wenger, M. B. Johnston, L. M. Herz, H. J. Snaith, and F. Giustino, "Cs2inagcl6: A New Lead-Free Halide Double Perovskite with Direct Band Gap," *The J. Phys. Chem. Lett.*, vol. 8, pp. 772–778, Feb. 2017. http://dx.doi.org/10.1021/acs.jpclett.6b02682

[94] J. Zhou, Z. Xia, M. S.Molokeev, X. Zhang, D. Peng, and Q. Liu, "Composition design, optical gap and stability investigations of lead-free halide double perovskite $Cs_2AgInCl_6$," *J. Mater. Chem. A*, vol. 5, pp. 15 031–15 037, 2017. http://pubs.rsc.org/en/Content/ArticleLanding/2017/TA/C7TA04690A

[95] A. H. Slavney, L. Leppert, D. Bartesaghi, A. Gold-Parker, M. F. Toney, T. J. Savenije, J. B. Neaton, and H. I. Karunadasa, "Defect-Induced Band-Edge Reconstruction of a Bismuth-Halide Double Perovskite for Visible-Light Absorption," *J. Am. Chem. Soc.*, vol. 139, pp. 5015–5018, Apr. 2017. http://dx.doi.org/10.1021/jacs.7b01629

[96] K.-z. Du, W. Meng, X. Wang, Y. Yan, and D. B. Mitzi, "Bandgap Engineering of Lead-Free Double Perovskite $Cs_2AgBiBr_6$ through Trivalent Metal Alloying," *Angew. Chem. Int. Ed.*, vol. 56, pp. 8158–8162, Jul. 2017. http://onlinelibrary.wiley.com/doi/10.1002/anie.201703970/abstract

[97] M. R. Filip, X. Liu, A. Miglio, G. Hautier, and F. Giustino, "Phase Diagrams and Stability of Lead-Free Halide Double Perovskites $Cs_2BB'X_6$: B = Sb and Bi, b′ = Cu, Ag, and Au, and X = Cl, Br, and I," *J. Phys. Chem. C*, vol. 122, pp. 158–170, Jan. 2018. https://doi.org/10.1021/acs.jpcc.7b10370

[98] G. Volonakis, A. A. Haghighirad, H. J. Snaith, and F. Giustino, "Route to Stable Lead-Free Double Perovskites with the Electronic Structure of $CH_3NH_3PbI_3$: A Case for Mixed-Cation $[Cs|CH_3NH_3|CH(NH_2)_2]_2InBiBr_6$," *J. Phys. Chem. Lett.*, vol. 8, pp. 3917–3924, Aug. 2017. https://doi.org/10.1021/acs.jpclett.7b01584

[99] X.-G. Zhao, J.-H. Yang, Y. Fu, D. Yang, Q. Xu, L. Yu, S.-H. Wei, and L. Zhang, "Design of Lead-Free Inorganic Halide Perovskites for Solar Cells via Cation-Transmutation," *J. Am. Chem. Soc.*, vol. 139, pp. 2630–2638, Feb. 2017. http://dx.doi.org/10.1021/jacs.6b09645

[100] W. Meng, X. Wang, Z. Xiao, J. Wang, D. B. Mitzi, and Y. Yan, "Parity-Forbidden Transitions and Their Impact on the Optical Absorption Properties of Lead-Free Metal Halide Perovskites and Double Perovskites," *J. Phys. Chem. Lett.*, vol. 8, pp. 2999–3007, Jul. 2017. https://doi.org/10.1021/acs.jpclett.7b01042

[101] X.-G. Zhao, D. Yang, Y. Sun, T. Li, L. Zhang, L. Yu, and A. Zunger, "Cu–In Halide Perovskite Solar Absorbers," *J. Am. Chem. Soc.*, vol. 139, pp. 6718–6725, May 2017. http://dx.doi.org/10.1021/jacs.7b02120

[102] J. Dai, L. Ma, M. Ju, J. Huang, and X. ChengZeng, "In- and Ga-based inorganic double perovskites with direct bandgaps for photovoltaic applications," *Phys. Chem. Chem. Phys.*, vol. 19, pp. 21 691–21 695, 2017. http://pubs.rsc.org/en/Content/ArticleLanding/2017/CP/C7CP03448B

[103] A. Jain, O. Voznyy, and E. H. Sargent, "High-Throughput Screening of Lead-Free Perovskite-like Materials for Optoelectronic Applications," *J. Phys. Chem. C*, vol. 121, pp. 7183–7187, Apr. 2017. https://doi.org/10.1021/acs.jpcc.7b02221

[104] N. Kojima, M. Hasegawa, H. Kitagawa, T. Kikegawa, and O. Shimomura, "P-T Phase Diagram and Gold Valence State of the Perovskite-Type Mixed-Valence Compounds $Cs_2Au_2X_6$ (X = Cl, Br, and I) under High Pressures," *J. Am. Chem. Soc.*, vol. 116, pp. 11 368–11 374, Dec. 1994. https://doi.org/10.1021/ja00104a016

[105] N. Matsushita, H. Kitagawa, and N. Kojima, "A Three-Dimensional Iodo-Bridged Mixed-Valence Gold(I, III) Compound, $Cs_2Au^{I}Au^{III}I_6$," *Acta Cryst C*, vol. 53, pp. 663–666, Jun. 1997. //scripts.iucr.org/cgi-bin/paper?oa1010

[106] X. J. Liu, K. Matsuda, Y. Moritomo, A. Nakamura, and N. Kojima, "Electronic structure of the gold complexes $Cs_2Au_2X_6$ (X =I, Br, and Cl)," *Phys. Rev. B*, vol. 59, pp. 7925–7930, Mar. 1999. https://link.aps.org/doi/10.1103/PhysRevB.59.7925

[107] S. Wang, A. F. Kemper, M. Baldini, M. C. Shapiro, S. C. Riggs, Z. Zhao, Z. Liu, T. P. Devereaux, T. H. Geballe, I. R. Fisher, and W. L. Mao, "Bandgap closure and reopening in $CsAuI_3$ at high pressure," *Phys. Rev. B*, vol. 89, p. 245109, Jun. 2014. https://link.aps.org/doi/10.1103/PhysRevB.89.245109

[108] L. Debbichi, S. Lee, H. Cho, A. M. Rappe, K.-H. Hong, M. S. Jang, and H. Kim, "Mixed Valence Perovskite $Cs_2Au_2I_6$: A Potential Material for Thin-Film Pb-Free Photovoltaic Cells with Ultrahigh Efficiency," *Adv. Mater.*, vol. 30, pp. 1 707 001(1)–1 707 001(6), 2018. https://onlinelibrary.wiley.com/doi/abs/10.1002/adma.201707001

[109] C. J. Howard, B. J. Kennedy, and P. M. Woodward, "Ordered double perovskites – a group-theoretical analysis," *Acta Cryst B*, vol. 59, pp. 463–471, Aug. 2003. //scripts.iucr.org/cgi-bin/paper?ta5000

[110] M. Retuerto, T. Emge, J. Hadermann, P. W. Stephens, M. R. Li, Z. P. Yin, M. Croft, A. Ignatov, S. J. Zhang, Z. Yuan, C. Jin, J. W. Simonson, M. C. Aronson, A. Pan, D. N. Basov, G. Kotliar, and M. Greenblatt, "Synthesis and Properties of Charge-Ordered Thallium Halide Perovskites, $CsTl^{+}_{0.5}tl^{3+}_{0.5}x_3$ (X = F or Cl): Theoretical Precursors for Superconductivity?" *Chem. Mater.*, vol. 25, pp. 4071–4079, Oct. 2013. https://doi.org/10.1021/cm402423x

[111] P. E. Blöchl, O. Jepsen, and O. K. Andersen, "Improved tetrahedron method for brillouin-zone integrations," *Phys. Rev. B*, vol. 49, pp. 16 223–16 233, Jun 1994. https://link.aps.org/doi/10.1103/PhysRevB.49.16223

[112] L. Yu and A. Zunger, "Identification of Potential Photovoltaic Absorbers Based on First-Principles Spectroscopic Screening of Materials," *Phys. Rev. Lett.*, vol. 108, p. 068701, Feb. 2012. https://link.aps.org/doi/10.1103/PhysRevLett.108.068701

[113] A. Togo and I. Tanaka, "First principles phonon calculations in materials science," *Scr. Mater.*, vol. 108, pp. 1–5, Nov 2015.

[114] V. M. Goldschmidt, "Die Gesetze der Krystallochemie," *Naturwissenschaften*, vol. 14, pp. 477–485, May 1926. https://doi.org/10.1007/BF01507527

[115] W. Travis, E. N. K. Glover, H. Bronstein, D. O. Scanlon, and R. G. Palgrave, "On the application of the tolerance factor to inorganic and hybrid halide perovskites: a revised system," *Chem. Sci.*, vol. 7, pp. 4548–4556, Jun. 2016. https://pubs.rsc.org/en/content/articlelanding/2016/sc/c5sc04845a

[116] W. Sun, S. T. Dacek, S. P. Ong, G. Hautier, A. Jain, W. D. Richards, A. C. Gamst, K. A. Persson, and G. Ceder, "The thermodynamic scale of inorganic crystalline metastability," *Sci. Adv.*, vol. 2, pp. e1 600 225(1)–e1 600 225(8), Nov. 2016. http://advances.sciencemag.org/content/2/11/e1600225

[117] H. Wei, M.-H. Du, L. Stand, Z. Zhao, H. Shi, M. Zhuravleva, and C. L. Melcher, "Scintillation properties and electronic structures of the intrinsic and extrinsic mixed elpasolites $cs_2Nar br_3 i_3$ (r = La, y)," *Phys. Rev. Applied*, vol. 5, pp. 024 008(1)–024 008(12), Feb 2016. https://link.aps.org/doi/10.1103/PhysRevApplied.5.024008

[118] D. Y. Wan, Y. L. Zhao, Y. Cai, T. C. Asmara, Z. Huang, J. Q. Chen, J. Hong, S. M. Yin, C. T. Nelson, M. R. Motapothula, B. X. Yan, D. Xiang, X. Chi, H. Zheng, W. Chen, R. Xu, Ariando, A. Rusydi, A. M. Minor, M. B. H. Breese, M. Sherburne, M. Asta, Q.-H. Xu, and T. Venkatesan, "Electron transport and visible light absorption in a plasmonic photocatalyst based on strontium niobate," *Nature Communications*, vol. 8, p. 15070, Apr. 2017. http://www.nature.com/doifinder/10.1038/ncomms15070

[119] T. C. Asmara, D. Wan, Y. Zhao, M. A. Majidi, C. T. Nelson, M. C. Scott, Y. Cai, B. Yan, D. Schmidt, M. Yang, T. Zhu, P. E. Trevisanutto, M. R. Motapothula, Y. P. Feng, M. B. H. Breese, M. Sherburne, M. Asta, A. Minor, T. Venkatesan, and A. Rusydi, "Tunable and low-loss correlated plasmons in Mott-like insulating oxides," *Nature Communications*, vol. 8, p. 15271, May 2017. http://www.nature.com/doifinder/10.1038/ncomms15271

[120] D. Liu, X. Yao, and D. M. Smyth, "Structure intergrowth in ceramic SrNbO3.5x," *Materials Research Bulletin*, vol. 27, pp. 387–392, Mar. 1992. http://www.sciencedirect.com/science/article/pii/002554089290068B

[121] X. Xu, C. Randorn, P. Efstathiou, and J. T. S. Irvine, "A red metallic oxide photocatalyst," *Nature Materials*, vol. 11, pp. 595–598, Jul. 2012. https://www.nature.com/articles/nmat3312

[122] D. Oka, Y. Hirose, S. Nakao, T. Fukumura, and T. Hasegawa, "Intrinsic high electrical conductivity of stoichiometric SrNb O 3 epitaxial thin films," *Physical Review B*, vol. 92, Nov. 2015. https://link.aps.org/doi/10.1103/PhysRevB.92.205102

[123] R. Dronskowski and P. E. Bloechl, "Crystal orbital Hamilton populations (COHP): Energy-resolved visualization of chemical bonding in solids based on density-functional calculations," *J. Phys. Chem.*, vol. 97, pp. 8617–8624, Aug. 1993. https://doi.org/10.1021/j100135a014

[124] V. L. Deringer, A. L. Tchougréeff, and R. Dronskowski, "Crystal Orbital Hamilton Population (COHP) Analysis As Projected from Plane-Wave Basis Sets," *J. Phys. Chem. A*, vol. 115, pp. 5461–5466, Jun. 2011. https://doi.org/10.1021/jp202489s

[125] S. Maintz, V. L. Deringer, A. L. Tchougréeff, and R. Dronskowski, "Analytic projection from plane-wave and PAW wavefunctions and application to chemical-bonding analysis in solids," *J. Comput. Chem.*, vol. 34, pp. 2557–2567, 2013. https://onlinelibrary.wiley.com/doi/abs/10.1002/jcc.23424

[126] S. Maintz, V. L. Deringer, A. L. Tchougréeff, and R. Dronskowski, "LOBSTER: A tool to extract chemical bonding from plane-wave based DFT," *J. Comput. Chem.*, vol. 37, pp. 1030–1035, 2016. https://onlinelibrary.wiley.com/doi/abs/10.1002/jcc.24300

[127] Z. Xiao, K.-Z. Du, W. Meng, J. Wang, D. B. Mitzi, and Y. Yan, "Intrinsic Instability of $Cs_2In(I)M(III)X_6$ (M = Bi, Sb; X = Halogen) Double Perovskites: A Combined Density Functional Theory and Experimental Study," *J. Am. Chem. Soc.*, vol. 139, pp. 6054–6057, May 2017. http://dx.doi.org/10.1021/jacs.7b02227

Appendix A:

Supplemental Materials for Computational Study of Halide Perovskite-Derived A_2BX_6 Inorganic Compounds: Chemical Trends in Electronic Structure and Structural Stability

---

The results presented in this appendix and Chapter 3 have been published as a regular article with title "*Computational Study of Halide Perovskite-Derived A_2BX_6 Inorganic Compounds: Chemical Trends in Electronic Structure and Structural Stability*" in Chem. Mater. 2017, 29, 77407749 by Yao Cai, Wei Xie, Hong Ding, Yan Chen, Krishnamoorthy Thirumal, Lydia H. Wong, Nripan Mathews, Subodh G. Mhaisalkar, Matthew Sherburne and Mark Asta[38]. The material is presented here with the permission of co-authors and publishers.

Table A.1: 41 A_2BX_6 compounds experimentally reported in the ICSD with A = K, Rb, Cs, B = Si, Ge, Sn, Pb, Ni, Pd, Pt, Se, Te, X = Cl. Br, I. Chemical formula, ICSD collection codes, space groups, crystal systems, and number of atoms per unit cell are listed.

Formula	ICSD ID	Space group	Crystal system	Nsites
K_2SnCl_6	6058	$Fm\bar{3}m$	Cubic	9
K_2SnBr_6	30212	P4/mnc	Tetragonal	18
K_2SnBr_6	35557	$P2_1/c$	Monoclinic	18
K_2SnBr_6	158955	$Fm\bar{3}m$	Cubic	9
K_2PdCl_6	33709	$Fm\bar{3}m$	Cubic	9
K_2PtCl_6	31114	$Fm\bar{3}m$	Cubic	9
K_2PtBr_6	23771	$Fm\bar{3}m$	Cubic	9
K_2PtI_6	37190	P4/mnc	Tetragonal	18
K_2SeBr_6	36228	$Fm\bar{3}m$	Cubic	9
K_2TeBr_6	37270	P4/mnc	Tetragonal	18
K_2TeBr_6	65115	$P2_1/c$	Monoclinic	18
K_2TeBr_6	38346	$Fm\bar{3}m$	Cubic	9
K_2TeI_6	23649	$P2_1/c$	Monoclinic	18
Rb_2SnCl_6	29026	$Fm\bar{3}m$	Cubic	9
Rb_2SnBr_6	158956	$Fm\bar{3}m$	Cubic	9
Rb_2SnI_6	22104	$Fm\bar{3}m$	Cubic	9
Rb_2PbCl_6	29029	$Fm\bar{3}m$	Cubic	9
Rb_2PdCl_6	33710	$Fm\bar{3}m$	Cubic	9
Rb_2PdBr_6	36305	$Fm\bar{3}m$	Cubic	9
Rb_2PdI_6	92478	$Fm\bar{3}m$	Cubic	9
Rb_2PdI_6	92477	Pnma	Orthorhombic	36
Rb_2PtCl_6	29028	$Fm\bar{3}m$	Cubic	9
Rb_2PtI_6	37191	$Fm\bar{3}m$	Cubic	9
Rb_2SeCl_6	26692	$Fm\bar{3}m$	Cubic	9
Rb_2TeCl_6	29027	$Fm\bar{3}m$	Cubic	9

Table A.1 – continued from previous page

Formula	ICSD ID	Space group	Crystal system	Nsites
Rb_2TeBr_6	49521	$Fm\bar{3}m$	Cubic	9
Rb_2TeBr_6	49520	I4/m	Tetragonal	9
Rb_2TeI_6	36009	P4/mnc	Tetragonal	18
Cs_2GeCl_6	28892	$Fm\bar{3}m$	Cubic	9
Cs_2SnCl_6	9023	$Fm\bar{3}m$	Cubic	9
Cs_2SnBr_6	158957	$Fm\bar{3}m$	Cubic	9
Cs_2PbCl_6	26713	$Fm\bar{3}m$	Cubic	9
Cs_2PdI_6	280189	I4/mmm	Tetragonal	9
Cs_2PdI_6	280190	$Fm\bar{3}m$	Cubic	9
Cs_2PtCl_6	29032	$Fm\bar{3}m$	Cubic	9
Cs_2PtBr_6	77381	$Fm\bar{3}m$	Cubic	9
Cs_2PtI_6	37193	$Fm\bar{3}m$	Cubic	9
Cs_2SeCl_6	26693	$Fm\bar{3}m$	Cubic	9
Cs_2TeCl_6	26704	$Fm\bar{3}m$	Cubic	9
Cs_2TeBr_6	27695	$Fm\bar{3}m$	Cubic	9
Cs_2TeI_6	38105	$Fm\bar{3}m$	Cubic	9

Table A.2: The energy above convex hull(E_{hull}) and decomposition products(if $E_{hull} > 0$) for 81 cubic A_2BX_6 compounds with A = K, Rb, Cs, B = Si, Ge, Sn, Pb, Ni, Pd, Pt, Se, Te, X = Cl. Br, I.

Compound	Energy above hull(meV)	Decomposition path
K_2SiCl_6	69	$SiCl_4$ + KCl
K_2SiBr_6	100	$SiBr_4$ + KBr
K_2SiI_6	150	SiI_4 + KI
K_2GeCl_6	33	KCl + $GeCl_4$
K_2GeBr_6	72	KBr + $GeBr_4$
K_2GeI_6	117	KI + GeI_4
K_2SnCl_6	7	K_2SnCl_6 ($P2_1/c$)

Table A.2 – continued from previous page

Compound	Energy above hull(meV)	Decomposition path
K_2SnBr_6	13	K_2SnBr_6 ($P2_1/c$)
K_2SnI_6	48	$KI + SnI_4$
K_2PbCl_6	0	
K_2PbBr_6	53	$Br + KBr + KPb_2Br_5$
K_2PbI_6	152	$PbI_2 + KI + I$
K_2NiCl_6	0	
K_2NiBr_6	0	
K_2NiI_6	40	$NiI_2 + KI + I$
K_2PdCl_6	0	
K_2PdBr_6	0	
K_2PdI_6	27	$PdI_2 + I + KI$
K_2PtCl_6	0	
K_2PtBr_6	0	
K_2PtI_6	12	K_2PtI_6 (P4/mnc)
K_2SeCl_6	0	
K_2SeBr_6	0	
K_2SeI_6	26	$I + Se + KI$
K_2TeCl_6	0	
K_2TeBr_6	23	K_2TeBr_6 ($P2_1/c$)
K_2TeI_6	31	K_2TeI_6 ($P2_1/c$)
Rb_2SiCl_6	42	$SiCl_4 + RbCl$
Rb_2SiBr_6	72	$RbBr + SiBr_4$
Rb_2SiI_6	109	$SiI_4 + RbI$
Rb_2GeCl_6	3	$GeCl_4 + RbCl$
Rb_2GeBr_6	40	$GeBr_4 + RbBr$
Rb_2GeI_6	86	$GeI_4 + RbI$
Rb_2SnCl_6	0	

Table A.2 – continued from previous page

Compound	Energy above hull(meV)	Decomposition path
Rb_2SnBr_6	0	
Rb_2SnI_6	12	$RbI + SnI_4$
Rb_2PbCl_6	0	
Rb_2PbBr_6	30	$RbPbBr_3 + Br + Rb_4PbBr_6$
Rb_2PbI_6	134	$RbPbI_3 + RbI_3$
Rb_2NiCl_6	0	
Rb_2NiBr_6	0	
Rb_2NiI_6	74	$RbI + NiI_2 + RbI_3$
Rb_2PdCl_6	0	
Rb_2PdBr_6	0	
Rb_2PdI_6	16	$PdI_2 + RbI_3 + RbI$
Rb_2PtCl_6	0	
Rb_2PtBr_6	0	
Rb_2PtI_6	0	
Rb_2SeCl_6	0	
Rb_2SeBr_6	0	
Rb_2SeI_6	27	$Se + RbI_3$
Rb_2TeCl_6	0	
Rb_2TeBr_6	1	Rb_2TeBr_6 (I4/m)
Rb_2TeI_6	6	Rb_2TeI_6 (P4/mnc)
Cs_2SiCl_6	22	$CsCl + SiCl_4$
Cs_2SiBr_6	50	$CsBr + SiBr_4$
Cs_2SiI_6	83	$SiI_4 + CsI$
Cs_2GeCl_6	0	
Cs_2GeBr_6	16	$CsBr + GeBr_4$
Cs_2GeI_6	59	$CsI + GeI_4$
Cs_2SnCl_6	0	

Table A.2 – continued from previous page

Compound	Energy above hull(meV)	Decomposition path
Cs_2SnBr_6	0	
Cs_2SnI_6	0	
Cs_2PbCl_6	0	
Cs_2PbBr_6	44	$CsPbBr_3 + CsBr_3$
Cs_2PbI_6	137	$CsI_3 + CsPbI_3$
Cs_2NiCl_6	0	
Cs_2NiBr_6	18	$CsBr + NiBr_2 + CsBr_3$
Cs_2NiI_6	29	$NiI_2 + CsI_3 + CsI$
Cs_2PdCl_6	0	
Cs_2PdBr_6	0	
Cs_2PdI_6	5	$CsI_3 + PdI_2 + CsI$
Cs_2PtCl_6	0	
Cs_2PtBr_6	0	
Cs_2PtI_6	0	
Cs_2SeCl_6	0	
Cs_2SeBr_6	0	
Cs_2SeI_6	20	$Se + CsI_3$
Cs_2TeCl_6	0	
Cs_2TeBr_6	0	
Cs_2TeI_6	0	

Appendix B:

Supplemental Materials for High-throughput Computational Study of Halide Double Perovskites Inorganic Compounds

B.0.1 Discussion on Tolerance Factor and Octahedral Factor

The approach used by Travis, et al.[115] is more accurate in terms of screening perovskites using geometric criteria. It argues that Shannon radii were calculated from more ionic compounds like fluorides and oxides, so are less suitable in more covalent compounds like bromides and iodides. Travis, et al then calculated 4 sets of ionic radii of several divalent metals for each of fluorides, chlorides, bromides and iodides, by surveying related compounds containing MX_6 octahedra in the ICSD. Using an approach similar to the above would require us to undertake a complete survey of related compounds containing MX_6 octahedra in ICSD, where M is a univalent or trivalent metal. Even though this is feasible, it requires additional work that lies beyond the scope of the current study.

As we use multiple screening steps (geometric criteria, energy above hull, band gap, effective mass), our goal is to reduce false negatives in each step. Here we argue that our current geometric screening uses a very relaxed criteria of tolerance factor and octahedral factor, in order to reduce false negatives. We allow some false positives in each of the screening steps.

Using the revised ionic radii for M-site cations, Travis et al set a criteria of octahedral factor $u > 0.41$ and tolerance factor $t > 0.875$[115]. In general, the revised ionic radii for M-site cations would be smaller than the respective Shannon radii. Translating the above criteria to the situation using Shannon radii, we would end up with

$$u > (\text{a number larger than } 0.41) \tag{B.1}$$

$$t > (\text{a number smaller than } 0.875) \tag{B.2}$$

The results presented in this appendix and Chapter 4 have been published as a regular article with title "*High-throughput Computational Study of Halide Double Perovskite Inorganic Compounds*" in Chem. Mater. 2019, 31, 15, 5392-5401 by Yao Cai, Wei Xie, Yin Ting Teng, P.C. Harikesh, Biplab Ghosh, Patrick Huck, Kristin A. Persson, Nripan Mathews, Subodh G. Mhaisalkar, Matthew Sherburne, and Mark Asta[78]. The material is presented here with the permission of co-authors and publishers.

The current criteria we use for octahedral factor is $0.4 < u < 1.0$, so on the lower side, and it is thus more relaxed than criteria based on (1) and is better at reducing false negatives.

The current criteria we use for tolerance factor is $0.82 < t < 1.08$ where the lower bound is significant smaller than 0.875 and would probably satisfy the tolerance criteria even if we used a more realistic set of ionic radii.

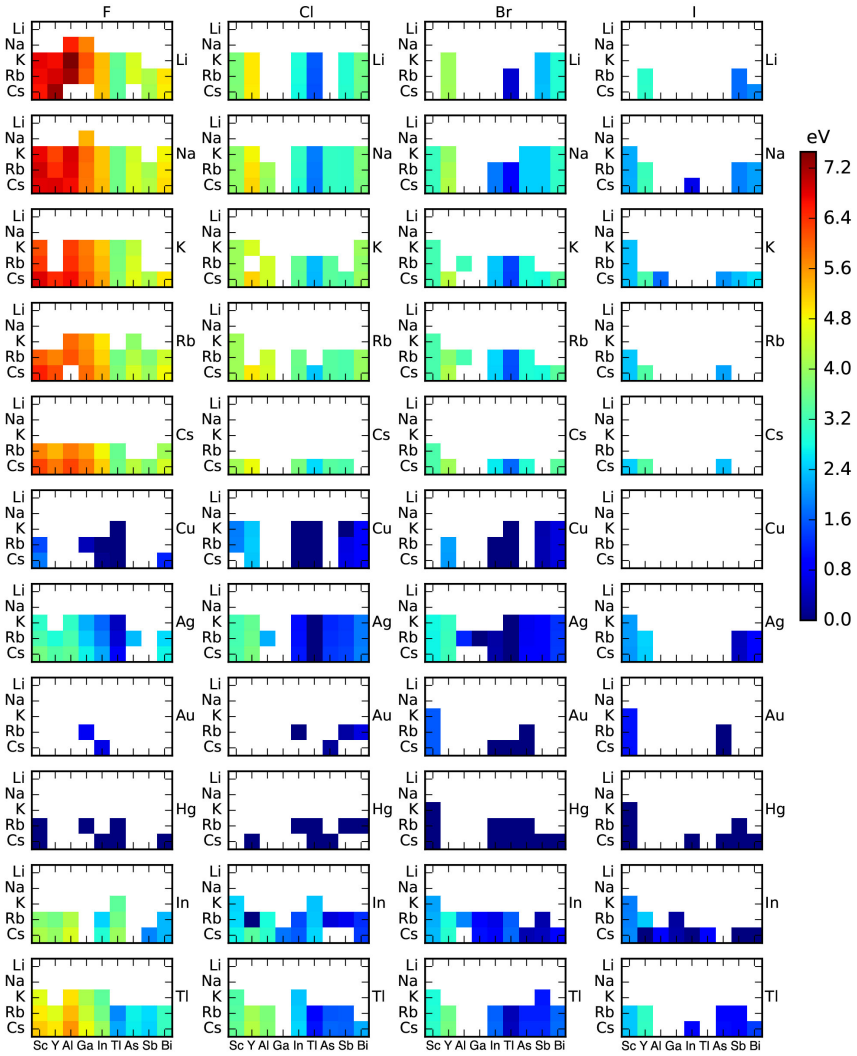

Figure B.1: PBE band gaps for all halide $A_2MM'X_6$ compounds with energy above hull less than 50 meV/atom with A = Li, Na, K, Rb, Cs, M = Li, Na, K, Rb, Cs, Cu, Ag, Au, Hg, In, Tl, M′ = Sc, Y, Al, Ga, In, Tl, As, Sb, Bi, and X = F, Cl, Br, I.

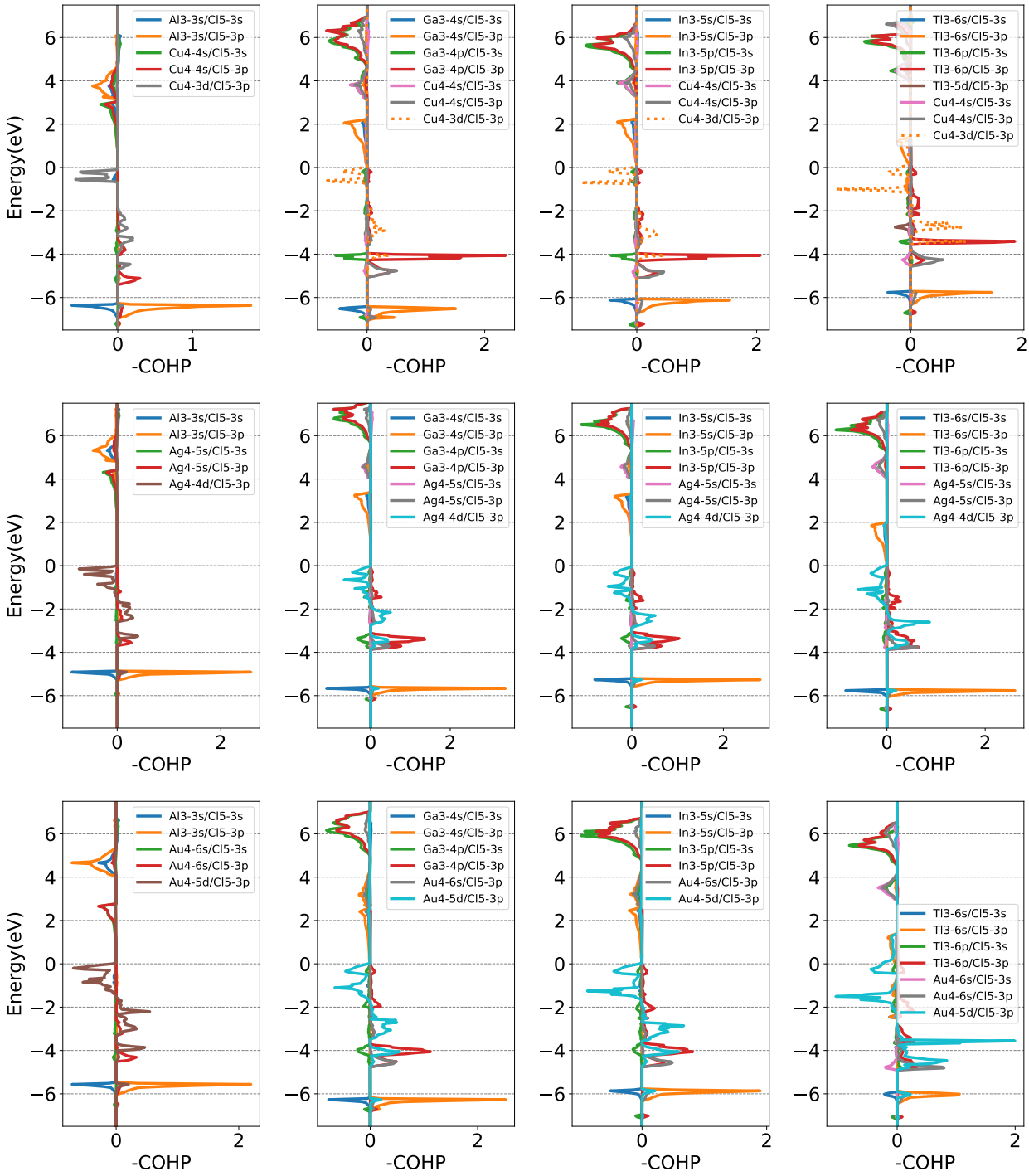

Figure B.2: Negative crystal orbital Hamilton population(-COHP)[123–126], calculated by PBE for $Cs_2MM'Cl_6$ with M = Cu, Ag, Au and M′ = Al, Ga, In ,Tl.

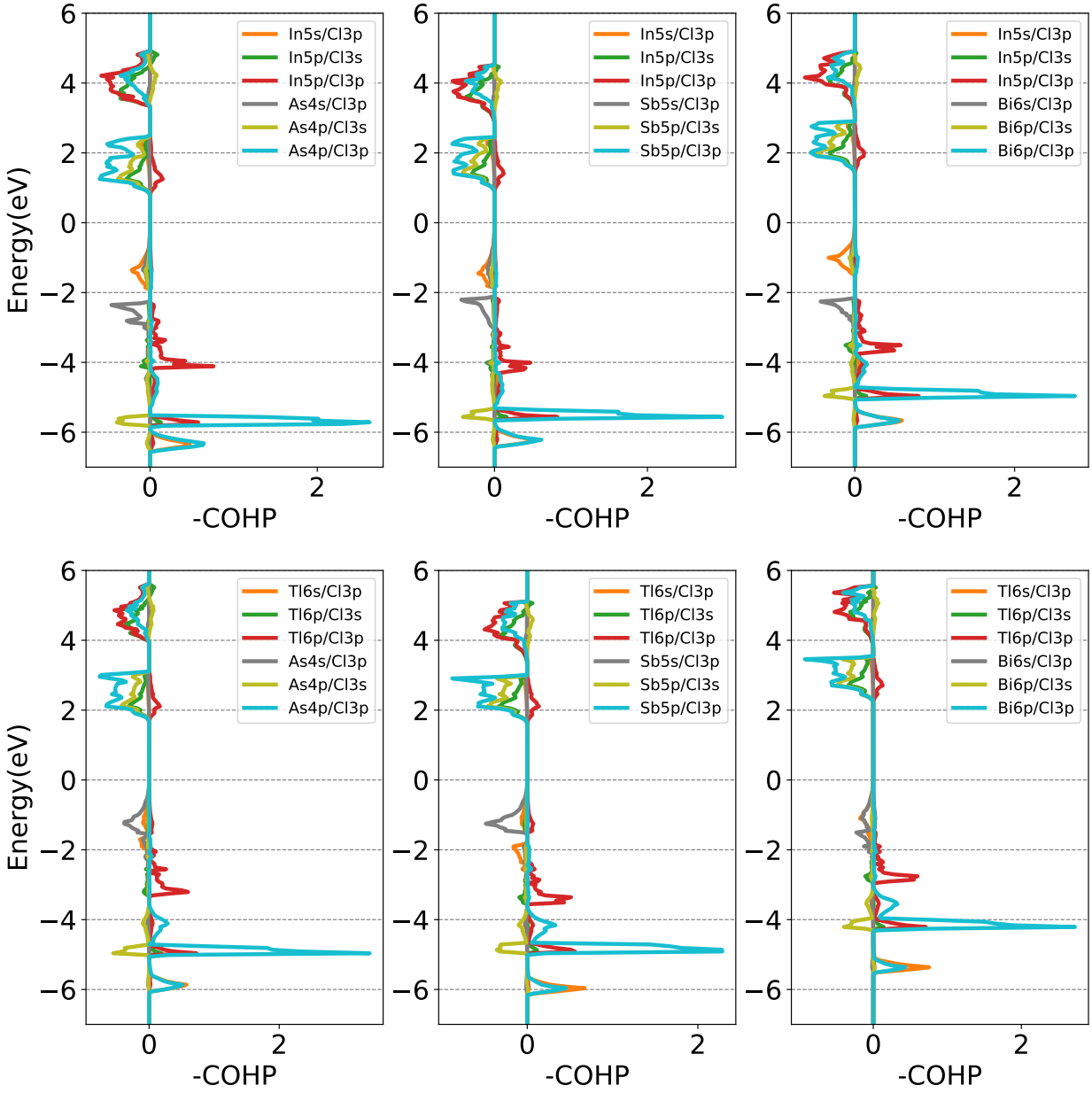

Figure B.3: Negative crystal orbital Hamilton population(-COHP)[123–126], calculated by PBE for $Cs_2MM'Cl_6$ with M = In, Tl and M′ = As, Sb, Bi.

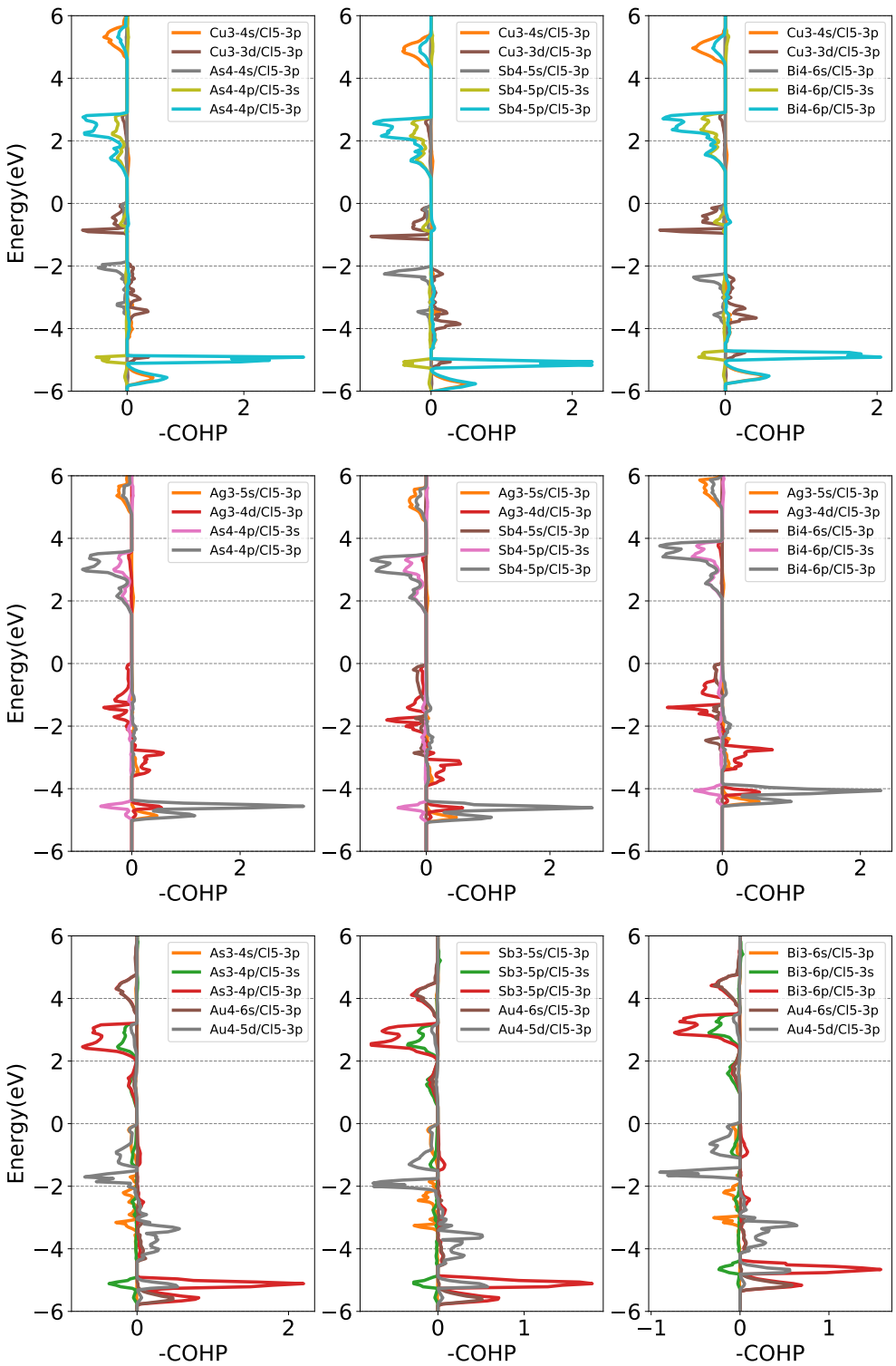

Figure B.4: Negative crystal orbital Hamilton population(-COHP)[123–126], calculated by PBE for $Cs_2MM'Cl_6$ with M = Cu, Ag, Au and M′ = As, Sb, Bi.

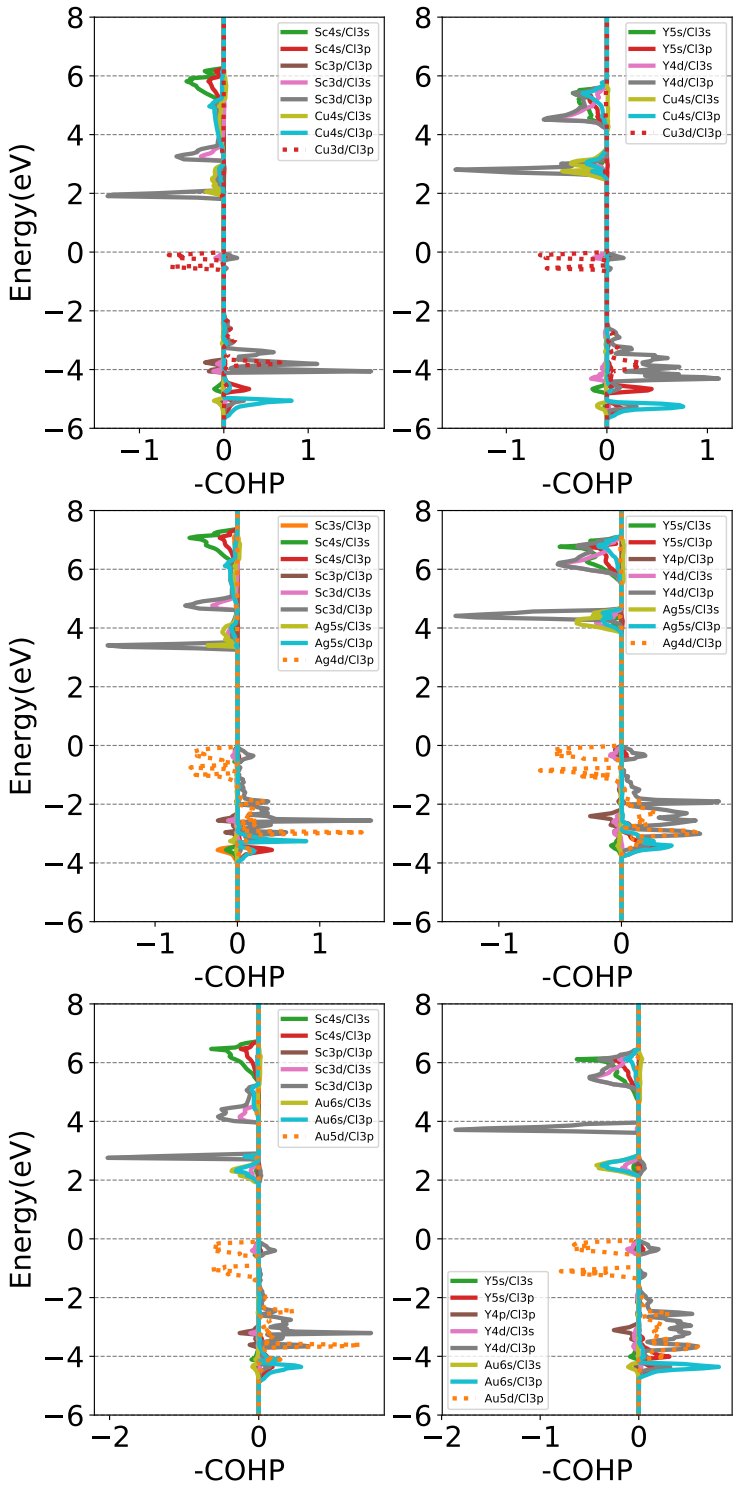

Figure B.5: Negative crystal orbital Hamilton population(-COHP)[123–126], calculated by PBE for $Cs_2MM'Cl_6$ with M = Cu, Ag, Au and M′ = Sc, Y.

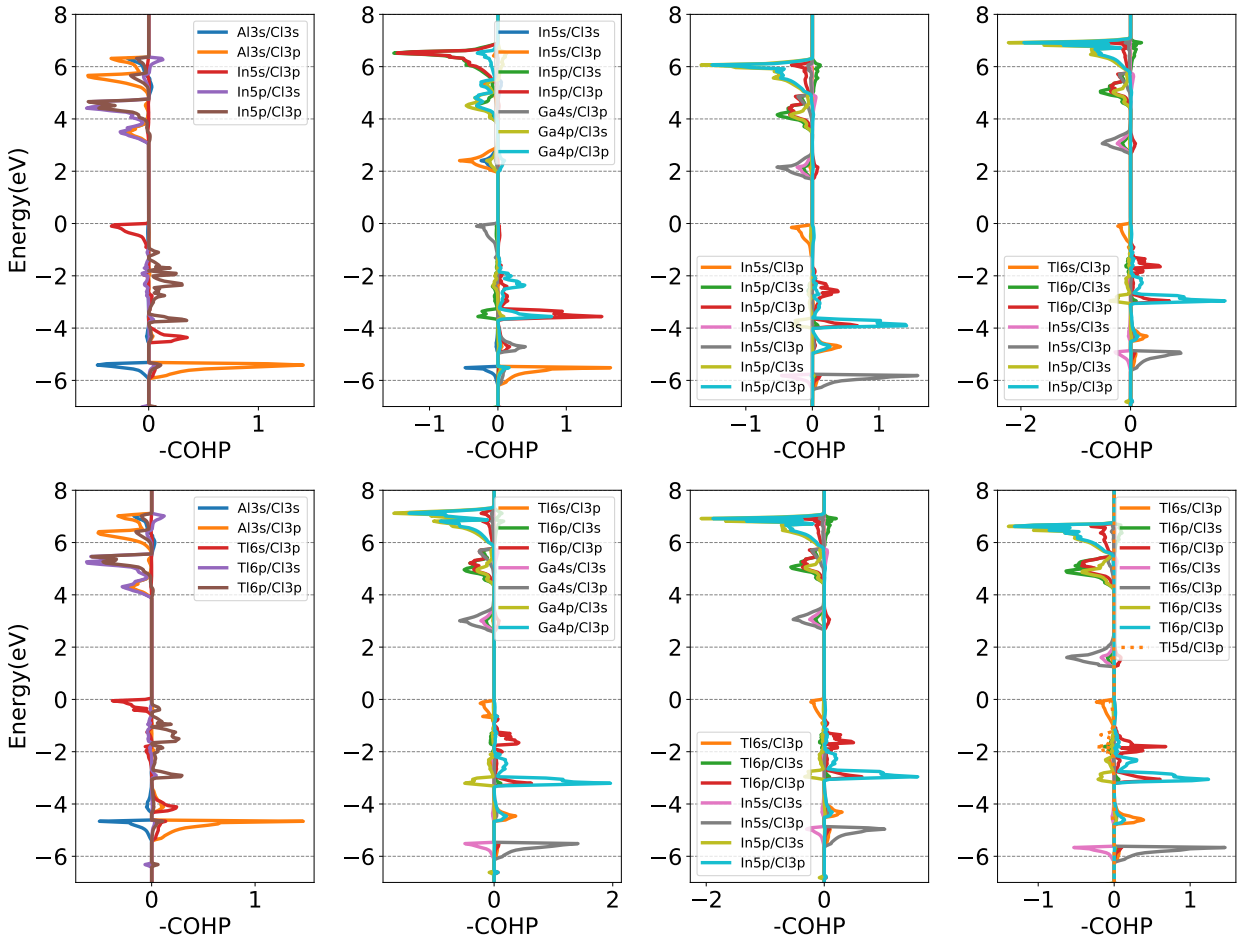

Figure B.6: Negative crystal orbital Hamilton population(-COHP)[123–126], calculated by PBE for $Cs_2MM'Cl_6$ with M = In, Tl and M′ = Al, Ga, In, Tl.

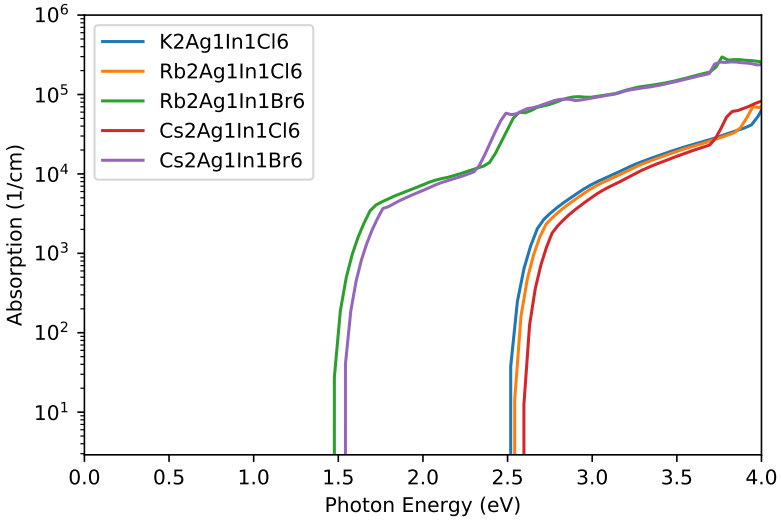

Figure B.7: Calculated absorption spectra for halide $A_2MM'X_6$ compounds from Category 1.

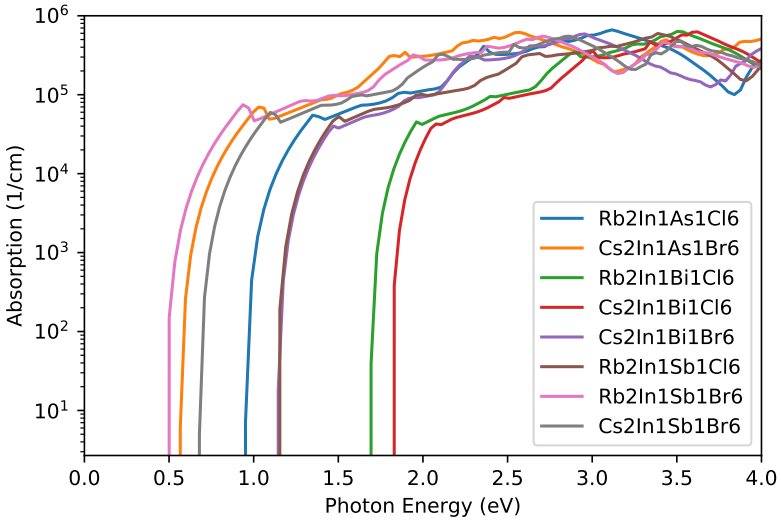

Figure B.8: Calculated absorption spectra for halide $A_2MM'X_6$ compounds from Category 2.

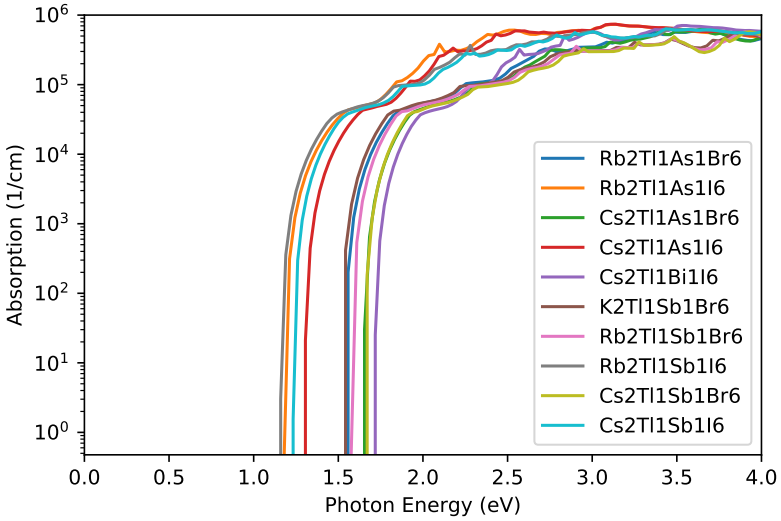

Figure B.9: Calculated absorption spectra for halide $A_2MM'X_6$ compounds from Category 2.

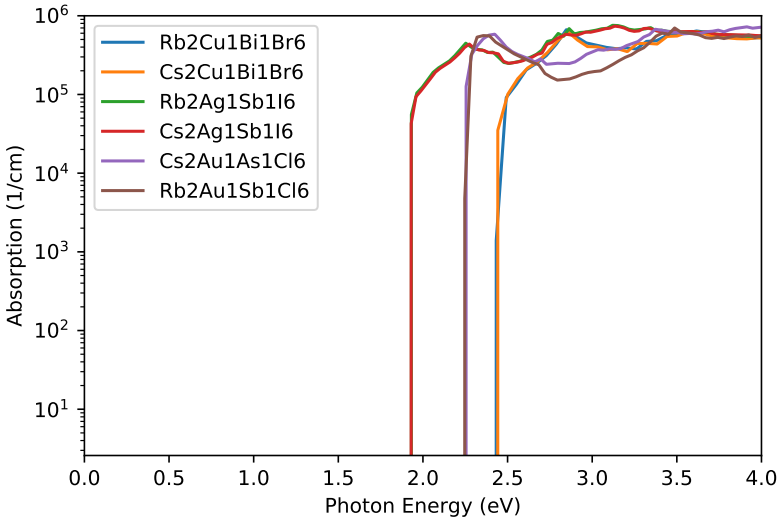

Figure B.10: Calculated absorption spectra for halide $A_2MM'X_6$ compounds from Category 3.

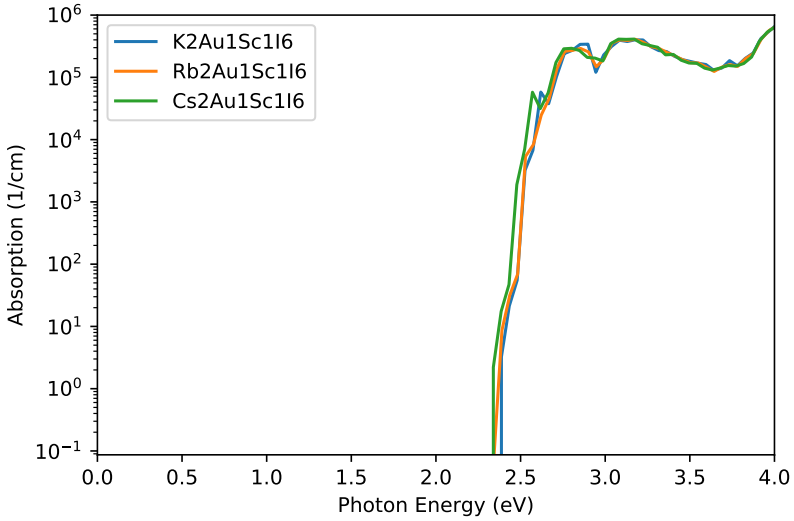

Figure B.11: Calculated absorption spectra for halide $A_2MM'X_6$ compounds from Category 4.

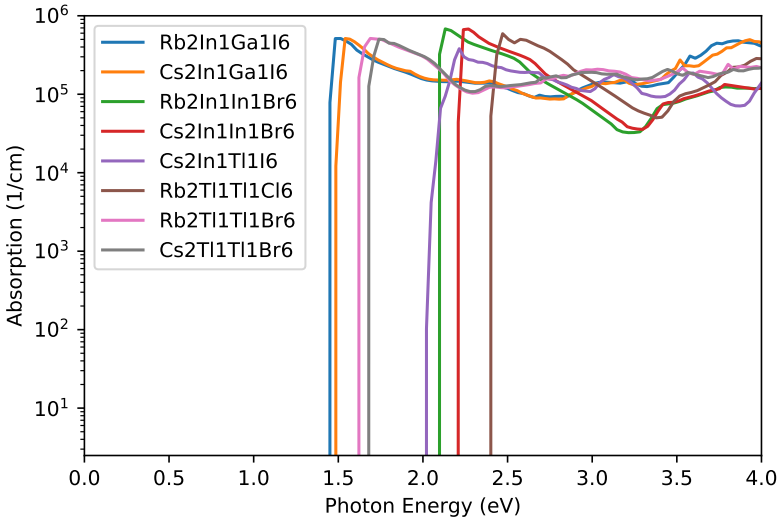

Figure B.12: Calculated absorption spectra for halide $A_2MM'X_6$ compounds from Category 5.

Table B.1: 79 $A_2MM'X_6$ compounds experimentally reported in the ICSD with A^{1+}, M^{1+}, M'^{3+} and X^{1-} ions. Chemical formula, ICSD collection codes, space groups, crystal systems, and number of atoms per unit cell are listed.

Formula	ICSD ID	Space Group	Crystal System	Nsites
$Cs_2AgAuCl_6$	[26162]	I4/mmm	Tetragonal	10
$Cs_2AgAuCl_6$	[24516]	$Fm\bar{3}m$	Cubic	10
$Cs_2AgBiBr_6$	[252164, 291597, 239875]	$Fm\bar{3}m$	Cubic	10
$Cs_2AgBiCl_6$	[291598, 239874, 252451]	$Fm\bar{3}m$	Cubic	10
Cs_2KBiF_6	[9383]	$Fm\bar{3}m$	Cubic	10
Cs_2KCoF_6	[6037]	$Fm\bar{3}m$	Cubic	10
Cs_2KCrF_6	[9705]	$Fm\bar{3}m$	Cubic	10
Cs_2KEuCl_6	[84845]	$Fm\bar{3}m$	Cubic	10
Cs_2KFeF_6	[42144]	$Fm\bar{3}m$	Cubic	10
Cs_2KMoF_6	[4053]	$Fm\bar{3}m$	Cubic	10
Cs_2KRhF_6	[4056]	$Fm\bar{3}m$	Cubic	10
Cs_2KScCl_6	[59196]	$Fm\bar{3}m$	Cubic	10
Cs_2KSmCl_6	[166519]	$Fm\bar{3}m$	Cubic	10
Cs_2KTbCl_6	[84844]	$Fm\bar{3}m$	Cubic	10
Cs_2KYF_6	[25367, 155977]	$Fm\bar{3}m$	Cubic	10
Cs_2LiGaF_6	[9004]	$P\bar{3}m1$	Trigonal	10
$Cs_2LiInCl_6$	[65735]	$R\bar{3}m$	Trigonal	20
$Cs_2LiLuCl_6$	[59194]	$Fm\bar{3}m$	Cubic	10
$Cs_2LiScCl_6$	[65734]	$R\bar{3}m$	Trigonal	20
Cs_2LiYCl_6	[65731]	$Fm\bar{3}m$	Cubic	10
Cs_2NaAlF_6	[93459, 200305, 41801, 93458]	$R\bar{3}m$	Trigonal	20

Table B.1 – continued from previous page

Formula	ICSD ID	Space Group	Crystal System	Nsites
$Cs_2NaBiCl_6$	[59195, 2738]	$Fm\bar{3}m$	Cubic	10
Cs_2NaBiF_6	[9382]	$Fm\bar{3}m$	Cubic	10
$Cs_2NaCeCl_6$	[85021]	$Fm\bar{3}m$	Cubic	10
Cs_2NaCoF_6	[42157]	$R\bar{3}m$	Trigonal	20
Cs_2NaCrF_6	[200, 9002]	$R\bar{3}m$	Trigonal	20
$Cs_2NaErCl_6$	[50361]	$Fm\bar{3}m$	Cubic	10
Cs_2NaErF_6	[23143]	$Fm\bar{3}m$	Cubic	10
Cs_2NaFeF_6	[16255, 9003, 201]	$R\bar{3}m$	Trigonal	20
Cs_2NaFeF_6	[65503]	$Fm\bar{3}m$	Cubic	10
Cs_2NaGaF_6	[55003, 55698]	$R\bar{3}m$	Trigonal	20
$Cs_2NaHoCl_6$	[245367, 245366]	$Fm\bar{3}m$	Cubic	10
Cs_2NaInF_6	[24921]	$Fm\bar{3}m$	Cubic	10
$Cs_2NaLaBr_6$	[426112]	$Fm\bar{3}m$	Cubic	10
$Cs_2NaLaCl_6$	[425945]	$Fm\bar{3}m$	Cubic	10
Cs_2NaScF_6	[22116, 55694]	$Fm\bar{3}m$	Cubic	10
$Cs_2NaSmCl_6$	[50363]	$Fm\bar{3}m$	Cubic	10
$Cs_2NaTbCl_6$	[96062]	$Fm\bar{3}m$	Cubic	10
Cs_2NaTlF_6	[22118]	$Fm\bar{3}m$	Cubic	10
Cs_2NaYBr_6	[65733]	$Fm\bar{3}m$	Cubic	10
Cs_2NaYCl_6	[245353, 65732, 245354]	$Fm\bar{3}m$	Cubic	10
Cs_2NaYF_6	[25368]	$Fm\bar{3}m$	Cubic	10
$Cs_2NaYbCl_6$	[50362]	$Fm\bar{3}m$	Cubic	10
Cs_2RbBiF_6	[9384]	$Fm\bar{3}m$	Cubic	10
Cs_2RbYF_6	[25366]	$Fm\bar{3}m$	Cubic	10

Table B.1 – continued from previous page

Formula	ICSD ID	Space Group	Crystal System	Nsites
Cs_2TlBiF_6	[9385]	$Fm\bar{3}m$	Cubic	10
Cs_2TlFeF_6	[6036]	$Fm\bar{3}m$	Cubic	10
Cs_2TlMoF_6	[15772]	$Fm\bar{3}m$	Cubic	10
$K_2CsBiCl_6$	[201983]	C2/c	Monoclinic	40
K_2LiAlF_6	[408552, 48149]	$R\bar{3}m$	Trigonal	20
K_2LiAlF_6	[37250, 408553]	$Fm\bar{3}m$	Cubic	10
K_2LiAlF_6	[27672]	$P\bar{3}m1$	Trigonal	30
K_2NaAlF_6	[34201, 164216, 40886, 22109, 6027]	$Fm\bar{3}m$	Cubic	10
K_2NaCrF_6	[40965, 22199]	$Fm\bar{3}m$	Cubic	10
K_2NaFeF_6	[61277, 22200]	$Fm\bar{3}m$	Cubic	10
K_2NaInF_6	[23430, 22113]	$Fm\bar{3}m$	Cubic	10
K_2NaMoF_6	[15777]	$Fm\bar{3}m$	Cubic	10
K_2NaRhF_6	[27342]	$Fm\bar{3}m$	Cubic	10
K_2NaScF_6	[22112, 65730]	$Fm\bar{3}m$	Cubic	10
K_2NaTlF_6	[22114]	$Fm\bar{3}m$	Cubic	10
K_2NaYF_6	[22115]	$Fm\bar{3}m$	Cubic	10
Na_2LiAlF_6	[280906, 96477]	$P2_1/c$	Monoclinic	20
Rb_2KBiF_6	[9387]	$Fm\bar{3}m$	Cubic	10
$Rb_2LiDyBr_6$	[402536]	$Fm\bar{3}m$	Cubic	10
Rb_2LiFeF_6	[16400]	$R\bar{3}m$	Trigonal	20
Rb_2LiGaF_6	[50468]	$R\bar{3}m$	Trigonal	20
Rb_2NaAlF_6	[290318]	$Fm\bar{3}m$	Cubic	10
Rb_2NaBiF_6	[9386]	$Fm\bar{3}m$	Cubic	10

Table B.1 – continued from previous page

Formula	ICSD ID	Space Group	Crystal System	Nsites
Rb_2NaCoF_6	[42148]	$Fm\bar{3}m$	Cubic	10
Rb_2NaCrF_6	[9706]	$Fm\bar{3}m$	Cubic	10
Rb_2NaErF_6	[23142]	$Fm\bar{3}m$	Cubic	10
Rb_2NaFeF_6	[42146, 4030, 40966]	$Fm\bar{3}m$	Cubic	10
Rb_2NaHoF_6	[86274]	I4/m	Tetragonal	10
Rb_2NaHoF_6	[86273]	$Fm\bar{3}m$	Cubic	10
Rb_2NaMoF_6	[15774]	$Fm\bar{3}m$	Cubic	10
Rb_2NaRhF_6	[27341]	$Fm\bar{3}m$	Cubic	10
$Rb_2NaTmCl_6$	[200549, 200550]	$Fm\bar{3}m$	Cubic	10
Rb_2NaYF_6	[25369]	$Fm\bar{3}m$	Cubic	10
Tl_2NaRhF_6	[27340]	$Fm\bar{3}m$	Cubic	10

Table B.2: Calculated lattice parameters of the 30 $A_2MM'X_6$ compounds identified in the initial screening for candidate solar absorber materials. The second and third columns list calculated results obtained by semi-local GGA-PBE and hybrid HSE06 functionals, respectively, and the last column lists calculated results from the literature. All compounds are cubic with space group $Fm\bar{3}m$.

	a (A)		
Compound	**GGA-PBE**	**HSE06**	**GGA-PBE from literature**
$K_2AgInCl_6$	10.50	10.43	
$Rb_2AgInCl_6$	10.57	10.49	
$Rb_2AgInBr_6$	11.14	11.05	
$Cs_2AgInCl_6$	10.68	10.60	
$Cs_2AgInBr_6$	11.22	11.16	
$Rb_2InAsCl_6$	10.92	10.83	
$Cs_2InAsBr_6$	11.51	11.43	
$Rb_2InBiCl_6$	11.41	11.35	
$Cs_2InBiCl_6$	11.48	11.42	11.44[99]
$Cs_2InBiBr_6$	11.95	11.89	11.93[99]
$Rb_2InSbCl_6$	11.26	11.20	
$Rb_2InSbBr_6$	11.77	11.69	
$Cs_2InSbBr_6$	11.83	11.76	11.80[99]
$Rb_2TlAsBr_6$	11.58	11.50	
$Cs_2TlAsBr_6$	11.66	11.58	
Cs_2TlAsI_6	12.42	12.34	
Cs_2TlBiI_6	12.85	12.79	12.84[99]
$Cs_2TlSbBr_6$	11.97	11.90	11.94[99]
Cs_2TlSbI_6	12.72	12.66	12.72[99]
$Cs_2AuAsCl_6$	10.54	10.48	
$Rb_2AuSbCl_6$	10.75	10.68	
K_2AuScI_6	11.81	11.77	
Rb_2AuScI_6	11.86	11.81	

Table B.2 – continued from previous page

	a (A)		
Compound	**GGA-PBE**	**HSE06**	**GGA-PBE from literature**
Cs_2AuScI_6	11.92	11.87	
Cs_2InGaI_6	12.23	12.14	
$Rb_2InInBr_6$	11.61	11.56	
$Cs_2InInBr_6$	11.67	11.63	
$Rb_2TlTlCl_6$	11.26	11.16	
$Rb_2TlTlBr_6$	11.80	11.68	
$Cs_2TlTlBr_6$	11.87	11.74	

Table B.3: 30 $A_2MM'X_6$ compounds identified in the screening for candidate solar absorber materials. Chemical formula, HSE+SOC calculated band gaps (E_g) and direct band gaps (direct E_g), band gap type(direct or indirect), measured band gaps and HSE+SOC calculations from the literature are listed. Asterisk(*) indicates HSE calculation without SOC.

	This work			Experiment	Previous calculations
Compound	**E_g(eV)**	**direct E_g(eV)**	**gap type**	**E_g(eV)**	**E_g(eV)**
$K_2AgInCl_6$	2.49	2.49	direct		
$Rb_2AgInCl_6$	2.52	2.52	direct		
$Rb_2AgInBr_6$	1.44	1.44	direct		
$Cs_2AgInCl_6$	2.57	2.57	direct	3.30[93]	2.6*[93]
$Cs_2AgInBr_6$	1.49	1.49	direct		
$Rb_2InAsCl_6$	0.74	0.74	direct		
$Cs_2InAsBr_6$	0.36	0.36	direct		
$Rb_2InBiCl_6$	0.79	0.79	direct		
$Cs_2InBiCl_6$	0.92	0.92	direct		0.91[99], 0.88[127]
$Cs_2InBiBr_6$	0.29	0.29	direct		0.0[99], 0.33[127]
$Rb_2InSbCl_6$	0.77	0.77	direct		
$Rb_2InSbBr_6$	0.20	0.20	direct		
$Cs_2InSbBr_6$	0.33	0.33	direct		0.41[99], 0.41[127]
$Rb_2TlAsBr_6$	1.11	1.11	direct		
$Cs_2TlAsBr_6$	1.23	1.23	direct		
Cs_2TlAsI_6	0.79	0.79	direct		
Cs_2TlBiI_6	0.66	0.66	direct		0.78[99]
$Cs_2TlSbBr_6$	1.11	1.11	direct		1.25[99]
Cs_2TlSbI_6	0.64	0.64	direct		0.81[99]
$Cs_2AuAsCl_6$	0.90	2.36	indirect		
$Rb_2AuSbCl_6$	0.95	2.36	indirect		

Table B.3 – continued from previous page

Compound	This work			Experiment	Previous calculations
	E_g(eV)	direct E_g(eV)	gap type	E_g(eV)	E_g(eV)
K_2AuScI_6	1.82	2.13	indirect		
Rb_2AuScI_6	1.81	2.11	indirect		
Cs_2AuScI_6	1.78	2.09	indirect		
Cs_2InGaI_6	0.76	1.60	indirect		
$Rb_2InInBr_6$	1.43	2.17	indirect		
$Cs_2InInBr_6$	1.57	2.30	indirect		
$Rb_2TlTlCl_6$	1.83	2.51	indirect		
$Rb_2TlTlBr_6$	0.99	1.73	indirect		
$Cs_2TlTlBr_6$	1.07	1.79	indirect		

Table B.4: 30 $A_2MM'X_6$ compounds identified from screening for candidate solar absorber materials. Chemical formula, energy above hull(E_{hull}), calculated effective masses for electrons (m_e) and holes (m_h) from this work and from the literature are listed.

	This work			Previous calculations	
Compound	$\mathbf{E_{hull}}$**(eV/atom)**	$\mathbf{m}_e$	$\mathbf{m}_h$	$\mathbf{m}_e$	$\mathbf{m}_h$
$K_2AgInCl_6$	0.006	0.29	0.83		
$Rb_2AgInCl_6$	0.000	0.28	0.85		
$Rb_2AgInBr_6$	0.005	0.18	0.68		
$Cs_2AgInCl_6$	0.000	0.29	0.90		
$Cs_2AgInBr_6$	0.000	0.18	0.71		
$Rb_2InAsCl_6$	0.031	0.39	0.09		
$Cs_2InAsBr_6$	0.026	0.30	0.05		
$Rb_2InBiCl_6$	0.000	0.39	0.17		
$Cs_2InBiCl_6$	0.014	0.39	0.18	0.39[99]	0.17[99]
$Cs_2InBiBr_6$	0.000	0.32	0.11	0.3[99]	0.11[99]
$Rb_2InSbCl_6$	0.000	0.39	0.11		
$Rb_2InSbBr_6$	0.028	0.31	0.05		
$Cs_2InSbBr_6$	0.007	0.31	0.07	0.3[99]	0.11[99]
$Rb_2TlAsBr_6$	0.008	0.29	0.14		
$Cs_2TlAsBr_6$	0.000	0.31	0.15		
Cs_2TlAsI_6	0.000	0.23	0.13		
Cs_2TlBiI_6	0.023	0.24	0.17	0.23[99]	0.18[99]
$Cs_2TlSbBr_6$	0.012	0.31	0.16	0.3[99]	0.2[99]
Cs_2TlSbI_6	0.022	0.23	0.13	0.23[99]	0.18[99]
$Cs_2AuAsCl_6$	0.046	0.27	0.35		
$Rb_2AuSbCl_6$	0.048	0.28	0.34		

Table B.4 – continued from previous page

	This work			Previous calculations	
Compound	$\mathbf{E}_{hull}$**(eV/atom)**	$\mathbf{m}_e$	$\mathbf{m}_h$	$\mathbf{m}_e$	$\mathbf{m}_h$
K_2AuScI_6	0.000	0.25	0.62		
Rb_2AuScI_6	0.000	0.24	0.63		
Cs_2AuScI_6	0.000	0.23	0.64		
Cs_2InGaI_6	0.018	0.22	0.51		
$Rb_2InInBr_6$	0.003	0.26	0.56		
$Cs_2InInBr_6$	0.000	0.27	0.58		
$Rb_2TlTlCl_6$	0.031	0.34	0.65		
$Rb_2TlTlBr_6$	0.026	0.25	0.55		
$Cs_2TlTlBr_6$	0.001	0.26	0.58		

Table B.5: 30 $A_2MM'X_6$ compounds identified from screening for candidate solar absorber materials. Chemical formula, category, calculated SLME at L = $1\mu m$, PBE band gap(E_g), PBE direct dipole allowed band gap(E_g^{da}) for each compound are listed below.

Formula	**Category**	**SLME at $1\mu m$ (%)**	**E_g (eV)**	**E_g^{da} (eV)**
$Cs_2AgInCl_6$	1	5.44	2.58	2.58
$Rb_2AgInCl_6$	1	6.34	2.53	2.53
$K_2AgInCl_6$	1	6.83	2.49	2.49
$Cs_2AgInBr_6$	1	22.46	1.51	1.51
$Rb_2AgInBr_6$	1	23.36	1.45	1.45
$Rb_2InSbBr_6$	2	16.58	0.47	0.47
$Cs_2InAsBr_6$	2	20.20	0.56	0.56
$Cs_2InSbBr_6$	2	23.90	0.67	0.67
$Cs_2InBiCl_6$	2	24.92	1.81	1.81
Cs_2TlBiI_6	2	26.62	1.71	1.71
$Rb_2InBiCl_6$	2	27.23	1.69	1.69
$Cs_2TlAsBr_6$	2	27.70	1.65	1.65
$Cs_2TlSbBr_6$	2	27.73	1.65	1.65
$Rb_2TlAsBr_6$	2	29.28	1.54	1.54
$Rb_2InAsCl_6$	2	30.42	0.95	0.95
$Cs_2InBiBr_6$	2	31.87	1.14	1.14
$Rb_2InSbCl_6$	2	31.90	1.13	1.13
Cs_2TlAsI_6	2	32.08	1.30	1.30
Cs_2TlSbI_6	2	32.16	1.23	1.23
$Cs_2AuAsCl_6$	3	5.57	0.97	2.22
$Rb_2AuSbCl_6$	3	5.73	1.03	2.27
K_2AuScI_6	4	8.80	2.01	2.51

Table B.5 – continued from previous page

Formula	Category	SLME at $1\mu m$ (%)	E_g (eV)	E_g^{da} (eV)
Rb_2AuScI_6	4	9.87	2.00	2.34
Cs_2AuScI_6	4	10.40	1.98	2.31
$Rb_2TlTlCl_6$	5	9.86	1.85	2.50
Cs_2InGaI_6	5	11.12	0.78	1.51
$Cs_2InInBr_6$	5	11.15	1.58	2.29
$Rb_2InInBr_6$	5	12.48	1.43	2.12
$Rb_2TlTlBr_6$	5	12.60	1.01	1.73
$Cs_2TlTlBr_6$	5	15.25	1.09	1.71

Table B.6: 30 $A_2MM'X_6$ compounds identified from screening for candidate solar absorber materials. Chemical formula, category (see main text for definition), least stable phonon frequencies (f_{min}, THz), q-point of least stable phonon, least stable phonon frequencies at Γ ($f_{min,\Gamma}$, THz), energy difference between the cubic structure and the distorted structure induced by the imaginary phonon mode at Γ ($\Delta E = E_{cubic}$-$E_{distorted}$, meV/atom) and the space group of the distorted structure for each compound are listed. Note that negative frequencies represent the magnitude of imaginary frequencies for unstable phonons. For those compounds with missing entries in the sixth column, the magnitude of f_{min} and $f_{min,\Gamma}$ are large and they are considered unstable, so the energies of the distorted structures are not calculated.

Formula	**Category**	$\mathbf{f}_{min}$	**q-point**	$\mathbf{f}_{min,\Gamma}$	**ΔE**	**Space group**
$Cs_2AgInCl_6$	1	-0.00	Γ	-0.00	-0.02	
$Rb_2AgInCl_6$	1	-1.30	Γ	-1.30	5.25	$P\bar{1}$
$K_2AgInCl_6$	1	-1.84	Γ	-1.84	23.07	$P\bar{1}$
$Cs_2AgInBr_6$	1	-0.20	Γ	-0.20	-0.00	$P\bar{1}$
$Rb_2AgInBr_6$	1	-198.11	W	-170.47	NaN	P1
$Rb_2InSbBr_6$	2	-43.91	L	-31.74	NaN	$P\bar{1}$
$Cs_2InAsBr_6$	2	-0.00	Γ	0.00	-0.00	
$Cs_2InSbBr_6$	2	-0.52	Γ	-0.52	2.60	$P\bar{1}$
$Cs_2InBiCl_6$	2	-1.14	Γ	-1.14	8.23	$P\bar{1}$
Cs_2TlBiI_6	2	-0.64	Γ	-0.64	15.70	$P\bar{1}$
$Rb_2InBiCl_6$	2	-1.55	Γ	-1.55	31.75	$P\bar{1}$
$Cs_2TlAsBr_6$	2	-0.52	Γ	-0.52	1.61	$P\bar{1}$
$Cs_2TlSbBr_6$	2	-0.76	Γ	-0.76	8.98	$P\bar{1}$
$Rb_2TlAsBr_6$	2	-0.92	Γ	-0.92	17.06	$P\bar{1}$
$Rb_2InAsCl_6$	2	-137.94	Γ	-137.94	NaN	$Fm\bar{3}m$
$Cs_2InBiBr_6$	2	-0.70	Γ	-0.70	6.76	$P\bar{1}$
$Rb_2InSbCl_6$	2	-1.44	Γ	-1.44	23.01	$P\bar{1}$
Cs_2TlAsI_6	2	-0.44	Γ	-0.44	3.08	$P\bar{1}$
Cs_2TlSbI_6	2	-0.60	Γ	-0.60	10.52	$P\bar{1}$

Table B.6 – continued from previous page

Formula	Category	f_{min}	q-point	$f_{min,\Gamma}$	ΔE	Space group
$Cs_2AuAsCl_6$	3	-4.99	L	-0.00	0.02	
$Rb_2AuSbCl_6$	3	-3.51	L	-1.16	24.80	$P\bar{1}$
K_2AuScI_6	4	-243.35	L	-109.07	NaN	P1
Rb_2AuScI_6	4	-15.76	Γ	-15.76	NaN	P1
Cs_2AuScI_6	4	-0.54	L	-0.41	46.19	$P\bar{1}$
$Rb_2TlTlCl_6$	5	-1.61	Γ	-1.61	29.06	$P\bar{1}$
Cs_2InGaI_6	5	-0.38	Γ	-0.38	1.11	$P\bar{1}$
$Cs_2InInBr_6$	5	-0.56	Γ	-0.56	2.32	$P\bar{1}$
$Rb_2InInBr_6$	5	-0.94	Γ	-0.94	18.81	$P\bar{1}$
$Rb_2TlTlBr_6$	5	-0.97	Γ	-0.97	28.50	$P\bar{1}$
$Cs_2TlTlBr_6$	5	-0.70	Γ	-0.70	6.81	$P\bar{1}$